Electrochemical tip-enhanced Raman spectroscopy

development and applications

Natalia Martín Sabanés

geb. in Madrid

Max Planck Institute for Polymer Research

Dissertation zur Erlangung des Grades
"Doctor rerum naturalium (Dr. rer. nat.)" am Fachbereiche:
09 - Chemie, Pharmazie un Geowissenschaften
der Johannes Gutenberg-Universität

Mainz, 2018

The work described in this thesis was performed at the Max-Planck Institut für Polymerforschung (MPIP, Ackermannweg 10, 55128, Mainz, Deutschland). This work was financially supported by the Deutsche Forschungsgemeinschaft (DFG).

Publications covered in this thesis

N. Martín Sabanés, L. Driessen and K.F. Domke; Versatile side-illumination geometry for tip-enhanced Raman spectroscopy at solid/liquid interfaces. *Anal. Chemistry 88(14)*, 7108-7114 (2016).

N. Martín Sabanés and K.F. Domke; Raman under water - nonlinear and nearfield approaches for electrochemical surface science. *ChemElectroChem 4*, 1-11 (2017).

N. Martín Sabanés, A, Elizabeth, J. Pfisterer and K.F. Domke; The effect of STM parameters on tip-enhanced Raman spectra. *Faraday Discussions 205*, 233-243 (2017).

N. Martín Sabanés, T. Ohto, D. Andrienko, Y. Nagata and K.F. Domke; Electrochemical TERS elucidates potential-induced molecular reorientation of adenine/Au(111). *Angew. Chemie Int. Ed. 56(33)*, 9796-9801 (2017). *Angew. Chemie 129(33)*, 9928-9933 (2017).

Other publications

K. Stadelmann, A. Elizabeth, N. Martín Sabanés and K.F. Domke; The SERS signature of PbS quantum dot oxidation. *Vibrational spectroscopy 91*, 157-162 (2017).

Abstract

Understanding the complex interplay of electrical and chemical reactions at the electrochemical interface is essential to optimize electrochemical devices in a large variety of applications ranging from energy-conversion to catalysis and synthesis. However, there is a lack of analytical techniques providing a full picture of the electrochemical interface. Tip-enhanced Raman spectroscopy (TERS) is a surface-specific vibrational spectroscopy providing chemical information with (sub)monolayer sensitivity and nanometric spatial resolution. TERS has been applied mostly to interrogate interfaces in air and ultra-high vacuum studies, but the characteristics of the technique make it an ideal candidate to study electrochemical interfaces. The objective of this work is to develop a TERS system able to work in electrochemical environment.

As a first step, a TERS setup operating in a simplified liquid/solid interface is developed. Despite a focus distortion at the air/liquid interface, which leads to a reduction of the scattering intensity by a factor of 3, we are able to efficiently collect TER spectra from few hundreds of small resonant and non-resonant molecules adsorbed at flat gold electrodes. Low TERS intensity in liquid can be compensated by phase modulation of the beam, however, enhancement factors of 10^5 can be reached with the setup without distortion correction. In air, TERS intensity has been found be proportional to d^{-10}, being d the tip-sample distance. In STM-based TERS, the gap distance is determined by the STM bias voltage and tunneling current, however, no systematic analysis on the dependence of the spectral features into these parameters was available up to now. By a series of experiments in argon and water, we find that the distance-dependent model is valid also in liquid experiments. Working at tunneling currents higher than 1 nA and bias voltages lower than 0.1 V results in an efficient rise of the TERS intensity in both air and liquid experiments. In this work we demonstrate systematic and reproducible TERS characterization of solid/liquid interfaces.

Finally, we demonstrate the extension of the system to electrochemical environment. As a test experiment, we measure a monolayer of adenine on a Au(111) electrode in acidic media. EC-TERS data combined with theoretical simulations offer a full picture of this electrochemical interface. We find that protonated adenine is physisorbed into the gold substrate in a tilted configuration at potentials lower than the potential of zero charge, and it adopts a vertical orientation at higher potentials. After deprotonation at 0.6 V (versus Ag/AgCl), neutral adenine is chemically adsorbed at the surface with a planar orientation.

The results obtained in this thesis demonstrate the promising capabilities of the instrument to characterize liquid and electrochemical interfaces, providing a general overview of chemical conversion, electron transfer reactions and orientation at the interface. The extension of TERS to electrochemical and liquid environments paves the way for powerful in situ chemical nano-characterization of a wide range of electrified interfaces.

Contents

Chapter 1

Introduction

The scientific method requires the direct observation of natural processes to either validate existing theories or discard them and formulate new hypotheses. It is therefore essential to develop techniques and instrumentation that allow us to observe the physico-chemical process that we are interested in. While great technical progress has yielded techniques that can access atoms and molecules in their characteristic length scales, or at extremely high temporal resolution, the access to fundamental processes in the nanoscale is, in many cases, limited to ultrahigh vacuum (UHV) and low-temperature studies. Gaining understanding about real-life applications and devices requires the extension of experimental techniques to realistic working conditions. The main motivation of the present thesis is the technical development of a spectroscopic method able to access the electrochemical (EC) interface in situ with nanoscale spatial resolution and sub-monolayer sensitivity, where traditional surface science methods operating in UHV conditions provide just a crude approximation of the real interplay between electrode and electrolyte at the interface during redox reactions.

Electrochemistry is the working principle of many important applications nowadays, ranging from energy conversion devices to green catalysis or synthesis. In order to optimize the macroscopic efficiency of electrochemical devices and reactions, we need to observe and understand the complex electrochemical interface where the electron transfer and chemical reactions take place. Despite its importance, there is a lack of analytical techniques able to provide a complete picture of such interfaces in the nanoscale. The ideal tool would provide control of the EC environment to trigger redox reactions at will, combined with in situ observation of the nanoscale processes resulting from such reactions. Motivated by the need for developing methodologies to access the electrochemical interface with nanoscale sensitivity and resolution, we have developed a unique instrument extending a conventional tip-enhanced Raman spectrometer

to electrochemical conditions.

Part of the content of this thesis is reproduced/adapted from published work. [1–4]

1.1 Motivation: towards full understanding of the electrochemical interface.

Electrochemical systems appear in many different disciplines and applications such as, for example, electrocatalysis, [5] biological membrane behaviour [6] or energy conversion [7]. Independently of the system considered, the most important common element is the electrochemical interface. It is at the interface between the electronic conductor electrode and the ionic conductor electrolyte where the interplay between electronic and chemical processes during an electrochemical reaction takes place. Therefore it became very clear in the last decades that fundamental understanding of the processes at the electrochemical interface could lead to a huge revolution in industry and science by tailoring (electro)active interfaces meeting specific application needs. Despite its importance and the extensive research triggered lately aiming to elucidate the specific interactions taking place at the EC-interface, a complete molecular understanding is far from being achieved. The reason behind this is that, due to its complexity, the understanding of the interfacial dynamics requires several capabilities to be achieved in one single instrument.

More specifically an ideal tool that would provide all the molecular information needed about the interfacial processes should count with the following capabilities:

- *High sensitivity* to detect and characterize species at very low concentrations at the interface and distinguish them from the bulk contribution of the solution.
- *Chemical specificity* to identify chemical species and characterize their interactions with the environment.
- *Nanoscale chemical resolution* to identify reactive species and sites.
- *In situ working conditions* to trigger and control the electrochemical reactions, i. e. electron transfer and chemical conversion.

Until this day, many different techniques have been employed in order to disentangle the complex interfacial processes, that combine one or more of the

previously mentioned capabilities. Cyclic voltammetry (CV) is traditionally used in electrochemistry to get thermodynamic and kinetic information about the interface and the reactivity of the electrode with spatial resolution in the mm to nm range.[8] In the last decades, CV has been combined with surface-science instrumentation to improve our knowledge about the electrochemical interface. EC-Scanning probe microscopy (EC-SPM) provides topological images in situ that can be used to distinguish reactive sites with atomic spatial resolution,[9] even providing video of electrochemical reactions at molecular scale;[10] however without specific chemical information. Scanning electrochemical microscopy (SECM)[9,11] and electrochemical scanning flow cell (ECSFC)[12] provide high spatial and temporal resolution to obtain additional insight into electrochemical conversion reactions; however individual reactive sites are not accessible with a detection sensitivity limited to the ppm range. Recently, in situ X-ray scattering tools reaching molecular spatial resolution have been used to reveal the surface structure and chemical composition of electrochemical interfaces.[13–15] While promising, X-ray studies in electrochemistry are scarce because they are synchrotron-based.

Vibrational spectroscopies provide the chemical information required to characterize molecular species and their interactions at the interface. Electrochemical infrared (IR)[16,17] and nonlinear sum frequency generation (SFG) spectroscopy[18–20] provide the required chemical information of the surface. Generally, they access a limited spectral range in the low energy region, and due to the strong IR absorption of water, working in aqueous electrolytes is challenging because water bands can mask the signature of adsorbates at the interface.

Raman spectroscopy can be also used to characterize electrochemical systems, despite its inherent low scattering cross-sections.[21–23] Being conventional Raman a technique only suitable for bulk measurements, near-field Raman techniques are being developed to access the molecular fingerprint of interfacial processes. Tip-enhanced Raman spectroscopy (TERS) offers the required chemical information with (sub) monolayer sensitivity and nanometric spatial resolution, and therefore fulfills three out of the four capabilities of our “ideal” tool.

Based on the combination of an SPM with a Raman instrument, TERS uses the near-field created at the apex of a nanometric tip to act as a nanoantenna that amplifies the Raman scattering of the molecules at the tip-sample gap by several orders of magnitude.[24–26] While ultra-hight vacuum (UHV) and air studies are increasingly used in surface science,[27–30] accessing solid-liquid interfaces and electrochemical systems remains difficult and only a few studies have been reported, due to the complexity of the experiments and the technical challenges that the solid-liquid interface entails.[1,31] The motivation of this work is, precisely, to address this problem and develop a TERS instrument

able to work under electrochemical conditions, providing a full nanoscale in-situ characterization of the electrochemical interface. To achieve it, great care had to be put into the different technical challenges, how to overcome them and couple efficiently the main players of an EC-TERS instrument: SPM, Raman platform and electrochemical environment.

1.2 Thesis outline

In the present work, all the steps in the instrument development are detailed and the performance of the setup tested in different reference experiments.

In Chapter 2 the most relevant theoretical aspects of TERS, SPM and electrochemistry are treated. They are intended to introduce the basic knowledge required to understand the following chapters. Additionally, a review of the most common experimental configurations of a TERS setup is provided, followed by a discussion of how ultra-high vacuum (UHV) and air-system can be adapted to work in liquid environments.

Chapter 3 has been devoted to the development of the setup, since it is a major part of the work done during this Ph.D. project. All details of our setup are given, with a special focus on technical challenges and the way to overcome them. One of the main issues when performing TERS in liquids is the distortion of the focus point in the air/glass/water interface. Spherical aberrations of the focus lead to a decrease of the detected Raman intensity. We are developing a procedure to correct the aberrations by phase-modulation of the laser beam. In Section 3.2, the origin of the focus distortion and the details of the modulation strategy are treated. Practicals details regarding sample and tip preparation are also included, as well as information about the experimental procedure and measurement.

The remaining chapters deal with the experiments done with the instrument to evaluate its performance and potential. While the final motivation is to access electrochemical interfaces, liquid TERS already provides a great technical progress and at the same time is an intermediate step in the building process. In Chapter 4, the initial trials of the machine on a simplified solid/liquid interface are provided. The chapter is focused on the comparison of in-air and in-liquid experiments to quantify the effect of the focus aberrations and other experimental parameters. Results from liquid TERS of resonant and non-resonant species are presented.[1] The discussion is focused on the comparison between air and liquid results and resonant versus non-resonant detection.

In Chapter 5 we evaluate the relation of the TERS setup and the scanning tunneling microscope (STM), the SPM technique used in our home-build liquid

(EC)-TERS setup.[3] In particular, we analyze how the STM parameters (tunneling current and bias) can affect the intensity and position of the Raman peaks in the TER spectra. The effect of each parameter is evaluated independently and a comparison between air and liquid results is provided.

Finally, in Chapter 6 we present a proof-of-principle of the EC-TERS setup used to successfully measure the electrochemical response of a monolayer of adenine in acidic media.[4] The experiments performed allow the understanding of the adsorption process of the DNA base in terms of chemical interaction and orientation with respect to the electrode. Supported by theoretical simulations, the results obtained provide a detailed overview of the physico-chemical processes at the interface as a function of sample potential.

Chapter 2

Fundamentals

This chapter contains an introduction to the theory behind TERS, STM and electrochemical methods, as well as the fundamental aspects of experimental configurations of TERS instruments. Some of the figures and content of this chapter have been previously published in *ChemElectroChem, 4 (8)*, 1814-1823, 2017, `http://onlinelibrary.wiley.com/doi/10.1002/celc.201700293/full` and reproduced here with permission from Wiley. [2]

2.1 Introduction

Electrochemistry is the area of physical-chemistry dealing with the interplay of chemical and electrical reactions. As defined by Schmickler and Santos, *electrochemistry is the study of structures and processes at the interface between an electronic conductor (the electrode) and an ionic conductor (the electrolyte).*[32] In order to understand an electrochemical system, one should then concentrate on studying the electrochemical interface. In an electrochemical cell, charge transfer across the interface between the electrode and the electroactive species in the electrolyte occurs accompanied by different chemical changes at the surface. These interfacial events are usually complicated, composed of different reaction steps including mass transport of electroactive species to the interface, adsorption, electron transfer, reorientation, desorption and diffusion of the products back into the bulk electrolyte.

Traditional electrochemical methods such as cyclic voltammetry, consist of triggering electrochemical reactions by tuning the Fermi energy of the electrode. The corresponding current flow resulting from charge transfer across the interface is evaluated. CV provide information about the charge transfer (or electrical current) as a function of electrode potential, however, it does not provide specific chemical information about the species being formed or the geometry/structure of adsorbates at the electrode. To gain a deeper insight into the electrochemical reactions, a combination of EC methods with other surface-specific techniques is common in electrochemical research.[33,34] In order to fully characterize the interface, we need a technique providing chemical information, with (sub)monolayer sensitivity (as to access the few species at the interface and distinguish them from bulk contributions) and, ideally, nanometric spatial resolution (to analyze the behavior of different adsorption sites), with potential control to induce and control the EC reactions.

As discussed in Chapter 1, different SPM and vibrational spectroscopic methods are commonly used in electrochemistry.[33,34] Raman spectroscopy, an inelastic scattering process (Fig. 2.1 a), is a good candidate because it provides a chemical fingerprint of the system studied, covering a broad spectral range including solid-state vibrations (phonons in the low-energy range), organic and inorganic molecules and ions up to the range where vibrations of water can be detected.

The main challenge to apply Raman spectroscopy to surface studies is to overcome the low scattering cross-sections, that generally require high concentration of analytes to produce a detectable signal. In order to access interfacial information, where few molecules are present, the sensitivity of the technique should be boosted. Enhanced Raman techniques such as surface and tip-enhanced Raman spectroscopy (SERS and TERS, Fig. 2.1 b and c, respectively) provide the

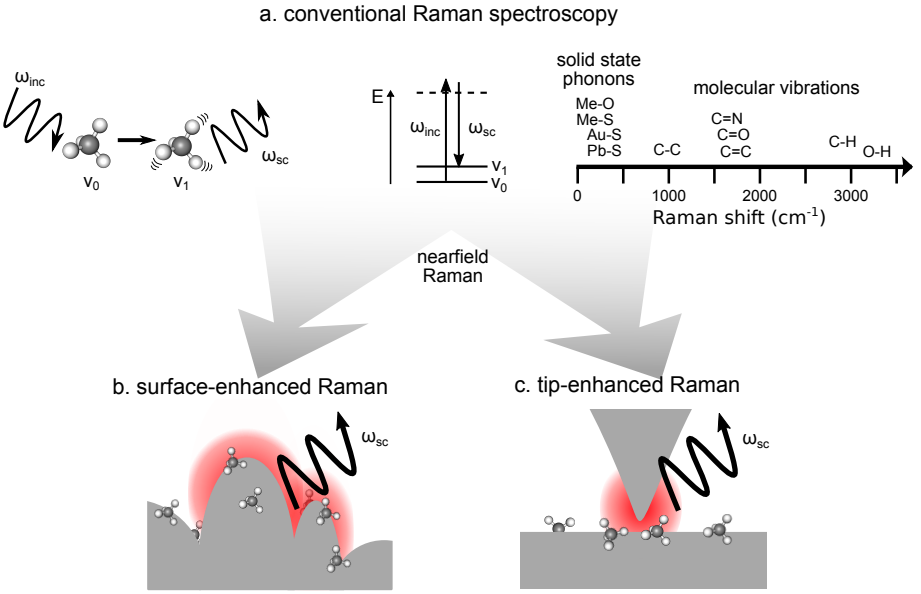

FIGURE 2.1. a: Raman spectroscopy is based on the inelastic scattering of light from a sample. Molecules are excited from the vibrational ground-state (ν_0) to a vibrational excited state (ν_1) whose energy difference matches the one between incident and scattered photons ($\omega_{inc} - \omega_{sc}$, Raman shift). Raman spectra cover a broad energy range, including solid-state phonons or metallic substrate-adsorbate interactions, the molecular fingerprint region, and high-frequency modes of CH/OH. To investigate a small amount of scatterers at interfaces or in confinement, the weak Raman scattering can be enhanced by near-field (surface- or tip-enhanced Raman, SERS/TERS) approaches. In b: SERS and c: TERS, field enhancement is achieved through the excitation of surface plasmons at rough surfaces or in a tip-sample gap, respectively. Reprinted with premission from *ChemElectroChem, 4 (8)*, 1814-1823, 2017, `http://onlinelibrary.wiley.com/doi/10.1002/celc.201700293/full`.[2]

sensitivity required to analyze the electrochemical interface.

Tip-enhanced Raman spectroscopy is a near-field vibrational spectroscopy technique.[35–37] It overcomes the low sensitivity of conventional Raman spectroscopy by using the nanometric tip of an SPM to generate a near-field around the tip apex that acts as a nanoantenna, also called hot-spot. Raman signals from species within the near-field are enhanced by factors of 10^7-10^{10} with respect to conventional Raman (a comparison of a conventional Raman spectrum and a TERS spectrum is given in Fig. 2.2). TERS is a surface specific technique where monolayer and even single molecule detection is possible.[38]

TERS evolved from the discovery of SERS in the 1970's.[21,22,39,40] In SERS multiple hot-spots are created by roughening metallic electrodes. SERS was

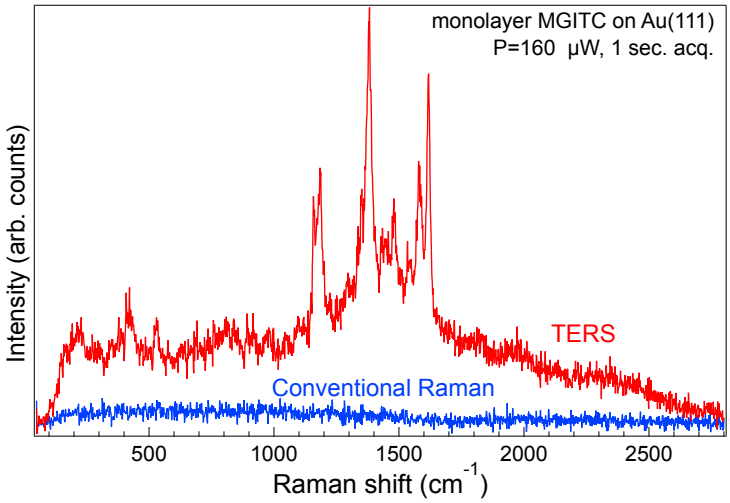

FIGURE 2.2. Example of TER spectrum of a monolayer of malaquite green isothiocyanate (MGITC) on Au(111) electrode (red) in comparison with a conventional Raman spectrum of the same sample (blue).

the first Raman technique reaching sub-monolayer sensitivity. The working principle of SERS is the excitation of localized surface plasmons (LSP) in metallic nanostructures, and therefore SERS is limited to studies on metallic rough electrodes.[41,42] TERS was developed 15 years ago to overcome this limitation.[43–47] By using a single, movable hot spot, i. e. the tip apex of an SPM, the high sensitivity is ensured without limitations to any specific substrate or sample. Additionally, the localized nature of the near-field gives the instrument nanometric spatial resolution. TERS has, in principle, all the ideal requirements of an instrument to study electrochemical interfaces if operated under electrochemical conditions.

Generally, there is a growing interest to move to surface-specific Raman studies in solution, as air and UHV conditions are crude approximations only for systems where water or supporting electrolyte are essential components of the complex interface. A systematic implementation of solid/liquid TERS setups would allow gaining essential information of many biological, electrochemical or catalytic interfaces where insight in the surface (physico)chemical processes is highly desired. However, despite great technological progress, TERS applications in liquid environments still remain scarce. The complexity of the TERS experiment itself combined with the additional requirements that the liquid environment entails can explain the long struggle of the community to achieve solid/liquid TERS.

The challenges to extend the setup to EC and liquid environment will be treated extensively in Chapter 3. In the remaining of this chapter, the basic theory about TERS and its components is presented. It starts with a brief introduction to the principles of interfacial electrochemistry, STM and Raman spectroscopy, followed by an extensive review about the principles of near-field Raman and TERS and its practical implementation.

2.2 Interfacial electrochemistry and cyclic voltammetry

In this section, the basic concepts in electrochemistry needed to understand the experimental work presented in the following chapters of this thesis are introduced. The field of electrochemistry is broad and many important concepts are missing in this description, for more detailed information the reader is referred to specialized literature. [32,48,49]

In electrochemical studies, we aim to elucidate the processes at one electrode/electrolyte interface of interest. In practice, every electrochemical cell consists of two electrodes separated by an electrolyte (with the corresponding electrode/electrolyte/electrode interfaces) which are externally connected by a conductive wire. Generally, a potential difference between the electrodes (cell potential) can be measured and represents the energy available to move charge between them. There are two types of electrochemical cells: galvanic and electrolytic cells. In galvanic cells, spontaneous reactions occur at the surface of the electrodes resulting in a net current flowing through the connecting wire. Batteries and fuel cells are the typical examples of galvanic cells, where chemical energy is converted into electrical energy. In electrolytic cells, applying an external potential between electrodes larger than the open circuit potential (potential difference measured between electrodes when no current is flowing between them), drives the electrochemical reactions. [48]

To study the reactions taking place at one electrode-electrolyte interface, the potential between the working electrode (the one under study) and a reference electrode is controlled and tuned. The potential applied to the working electrode results in a change of its Fermi energy, E_F, which induces electron transfer between the electrode and electroactive species in the electrolyte. Consider the specific example of an electrode at a specific potential U_0. The E_F of the electrode at this potential lies between the highest occupied molecular orbital (HOMO) and the lowest unoccupied molecular orbital (LUMO) of the electroactive species at the interface in the solution side, as depicted in the left part of Fig. 2.3. By changing the potential of the electrode to more posi-

tive values than U_0, its E_F decreases. If the potential applied is large enough an oxidation (or anodic) current is obtained as a result of electron transfer from the electrolyte to the electrode. Similarly, a potential more negative than U_0 rises the E_F. A reduction of the species in the solution can occur and a cathodic current is obtained flowing from the electrode to the electrolyte, as shown in Fig. 2.3, right. The potential ramp can be accompanied by different chemical changes at the interface such as adsorption/desorption of molecules or ions, change of oxidation state, synthesis of new species or reorientation of such species at the interface. The goal of electrochemical surface studies is to induce and monitor such reactions to characterize the electron transfer and chemical reactions occurring as a function of electrode potential. [32,49]

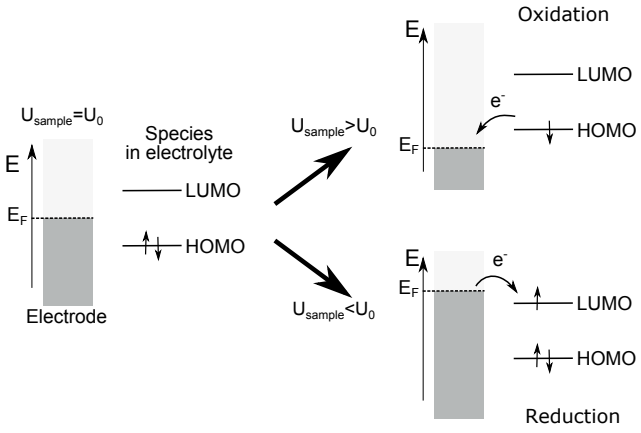

FIGURE 2.3. In electrochemistry, applying a potential to the electrode (U_{sample}) results in a ramp of Fermi energy (E_F) with respect to the equilibrium position, U_0. Depending on the sign of the potential, oxidation or reduction of the species in the solution occurs. Left: At a given potential U_0, the interface is at equilibrium with E_F of the electrode lying in between highest occupied molecular orbital (HOMO) and the lowest unoccupied molecular orbital (LUMO) of the electroactive species at the interface. Right: When U_{sample} is more positive than U_0, E_F decreases to a level where the electrons in the HOMO flow to the electrode resulting in a oxidation process (reduction of the electroactive species happens when U_{sample} is more negative than U_0, rising E_F of the electrode to a level where electrons can flow from the electrode into the LUMO of the species in solution).

The most common method to characterize the reactions taking place at the interface is cyclic voltammetry. In this technique, a three-electrode configuration is adopted, connected as shown in Fig. 2.4a to a potentiostat. The basic concept is to trigger and monitor electrochemical reactions occurring at the interface between the electrolyte and the working electrode (WE). The potentiostat controls the energy of the WE by applying a voltage between WE and a reference electrode (RE). The RE, with a fixed constant composition, has a

constant potential that allows tuning precisely the potential of the WE. No current flows through the RE, which is kept at a constant potential by connecting it to a high impedance point. [50,51] The current then flows between WE and the counter or auxiliary electrode (CE). The electrochemical properties of the CE should not affect the WE, and therefore the only requirement is that the products originated at its interface do not interact with the WE. The electrodes are mounted in an electrochemical cell filled with the electrolyte. The electrolyte consists of a solvent containing ions able to transport charge between electrodes. To choose an appropriate electrolyte, properties as the solubility of the analyte and its redox activity or electrical conductivity have to be considered. [32,49] The potentiostat controls the potential of the WE that is scanned linearly at a constant rate back and forth between two vertex values, Fig. 2.4b. The current of electrons flowing through the electrode is measured versus time and plotted as a function of applied potential in a cyclic voltammogram, Fig. 2.4c. The CV contains information about kinetics of the electron transfer reactions and redox potentials of the electroactive species. [32,49]

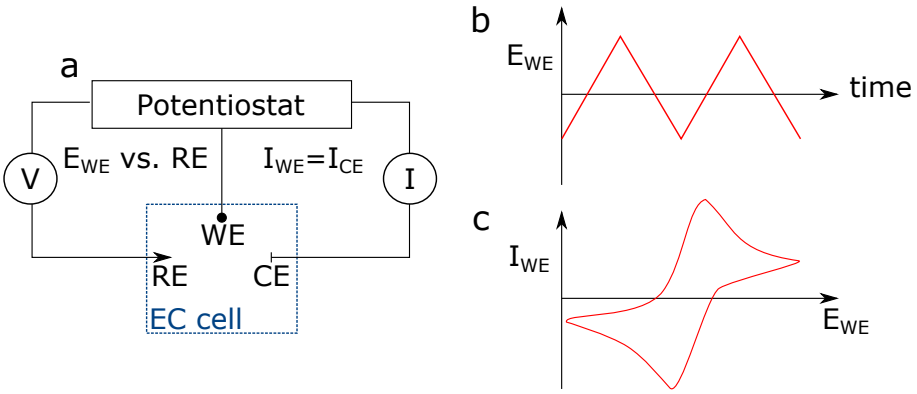

FIGURE 2.4. a: sketch of the three electrodes configuration in a potentiostat; WE, CE and RE are the working, counter and reference electrodes, E_{WE} and I_{WE} are the potential applied and resulting current in the WE. b: In CV the potential of the WE is ramped linearly back and forth between two vertex values versus time. The measured current flow is plotted versus applied potential in a cyclic voltammogram (c).

The current recorded in a CV is a convolution of faradaic and non-faradaic processes. Faradaic currents originate when electrons are transferred between WE and electrolyte, as for example in an oxidation or reduction process. Faradaic currents obey Faraday's law: the amount of oxidized or reduced species at the surface of the electrode is proportional to the current of electrons across the interface. [48] Faradaic currents appear in a CV as anodic and cathodic peaks. The peak height is proportional to the surface coverage (concentration per surface area) and the scan rate. Integration of the peak area gives information about

the charge transferred per unit of area across the interface.[51] At some potential ranges no charge transfer between electrode and electrolyte occurs, and yet an external current might be measured by the potentiostat. These currents are due to non-faradaic processes. Adsorption/desorption at solid/liquid interface or formation of the electrochemical double layer (EDL) are typical examples producing non-faradaic currents in the CV. When a potential is applied to the electrode a charge separation occurs at the interface: the electrode, generally a metal, has an excess charge that is balanced in the solution side by ions of opposite charge forming the EDL. The movement of charges to accumulate in both sides of the interface (electrons in the electrode side or ions in the solution side) produces an external current in the circuit even when no charge transfer across the interface occurs. This process is similar to the charging/discharging of an electrical capacitor. A capacitor is composed of two metallic electrodes separated by a dielectric material. When a potential is applied between electrodes, charges of opposite sign accumulate at each electrode according to the relation $q = C \cdot E$, being E the potential applied, q the charge stored and C the capacitance of the system indicating the ability of the capacitor to store charges. The charging process results in a current through the electrical circuit. The charging of the EDL appears in the CV as a constant capacitive current symmetric with respect to zero for positive and negative potential ramps.[33,34,48,51] In Chapter 6 a practical example of how reorientation of molecules at the electrode surface can affect the capacitance of the EDL is shown.

2.3 Scanning tunneling microscopy

SPM techniques are routinely used nowadays to study surfaces with sub-nanometric spatial resolution. In every SPM technique, a tip is scanned over the sample under investigation to interrogate the surface, either in direct contact or at sub-nanometric distance. The nanometric tip apex interacts with atoms and molecules in the surface and by monitoring such interactions one can gain information about the topography of the system as well as electronic properties with lateral spatial resolution determined by the tip dimension. There are two main types of SPM that are used in TERS: atomic force microscopy (AFM) and STM. The main difference between them is the feedback mechanism used to keep the tip-sample distance. In this work, we use an STM-based setup, and therefore in the following the discussion is focused on this type of SPM technique.

Invented in 1982 by Binnig and Rohrer and awarded a Nobel Prize in 1986,[52] STM has become nowadays a basic characterization technique in surface science. The physical principle behind STM is to measure quantum tunneling of

electrons through a classically forbidden energy barrier. According to quantum mechanics, when two metals are separated by vacuum, if the gap between them is close enough for their molecular orbitals to overlap, there is a non-zero probability of electrons (with energy, E, lower than the barrier height or work function ϕ) tunneling between them. In the gap region, the wave function,$\psi(z)$, decays exponentially with distance according to [53]

$$\psi(\mathrm{z}) = \psi(0) \cdot \mathrm{e}^{-\frac{\sqrt{2\mathrm{m}(\phi-\mathrm{E})}}{\hbar}\cdot \mathrm{d}} \tag{2.1}$$

with m the electron mass and $\hbar$ Planck's constant equal to $1.35{\cdot}10^{-34}$ Js.

In STM, tunneling between the tip and the sample under investigation is measured. Practically, if tip and sample are placed close to each other and we apply a bias voltage (E_b) between them, the Fermi levels of tip and sample will get misaligned and, depending on the sign of the voltage and the gap distance, electrons will tunnel from tip to sample or viceversa. This process is schematically depicted in Fig. 2.5.

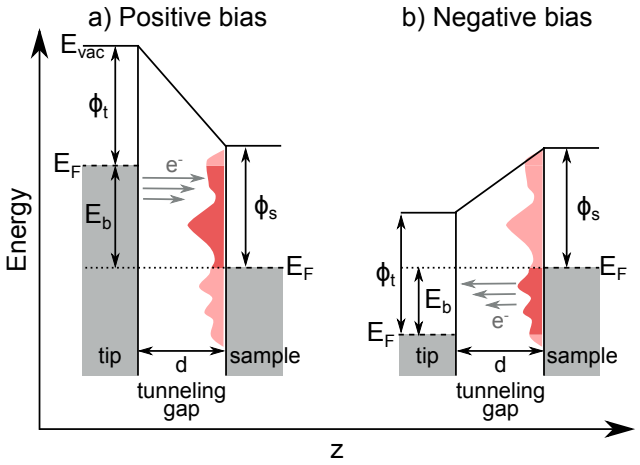

FIGURE 2.5. Schematic representation of the tunneling current in STM. Tip and sample are separated by a gap of width d. ϕ_t and ϕ_s are the work functions of tip and sample, respectively. When a bias voltage, E_b, is applied to the sample, the Fermi level (E_F) moves and electrons can tunnel from tip to sample in case of positive bias (a) or viceversa in case of negative bias (b). The tunneling current depends on the gap distance, the value of E_b applied and on the availability of empty states in tip and sample, or LDOS, illustrated in the figure by the red shadowed areas.

The tunneling current (I_t) decays exponentially with the gap distance and can be calculated by taking into account the density of states of the sample (LDOS) as: [53–57]

$$I_t \propto eE_b \cdot \rho(E_F) \cdot e^{-\beta \cdot d} \propto eE_b \cdot \rho(E_F) \cdot e^{-1.025\sqrt{\phi}d} \tag{2.2}$$

e is the elementary charge, β is the tunneling decay constant, $\beta = \frac{4\pi}{h}\sqrt{2m\phi}$ and $\rho(E_F)$ is the local density of states (LDOS) at the Fermi level.

The exponential dependence of I_t on the gap width is responsible for the high vertical resolution of the STM: decreasing the tip-sample gap by 1 Å results in an increase of the tunneling current by one order of magnitude. The gap distance is precisely controlled with a piezoelectric positioning system, which adjusts the tip position according to the feedback provided by the tunneling current.

To obtain the topography of the surface, the STM can operate in two modes: constant current and constant height. The experiments performed in this thesis were done in constant current mode, where the feedback loop adjusts the position of the tip to keep constant the tunneling current (set-point current) as the tip is scanned along the sample horizontally. The STM collects the vertical movements of the tip during scanning to retrieve the sample topography. Alternatively, the STM can be operated in constant height mode, where the feedback loop is disconnected and the tip vertical position is fixed while scanning, measuring a current map of the surface. This mode allows fast measurements due the lack of feedback mechanism, however scanning very rough samples (over few nm roughness) can result in a tip crash. Due to the dependence of the tunneling current on the density of states of the sample, the features in STM images are a convolution of topography and electronic structure. [52,58,59]

2.4 Raman spectroscopy

Raman spectroscopy is a vibrational spectroscopic technique based on the inelastic scattering of light. As such, Raman scattering is instantaneous, i. e. it does not imply the absorption of a photon as it is the case for other molecular spectroscopies like IR or fluorescence. It was first discovered by the Indian physicist Sir Chandrasekhara Venkata Raman in 1928, who was awarded the Nobel Prize for this discovery two years after.

When visible light interacts with a molecule, most of the incident photons are elastically scattered with the same energy in a process commonly known as Rayleigh scattering. Some small portion of the photons can promote electrons in the ground state to excited vibrational states, and therefore undergo inelastic scattering. The scattered photons will then have lower energy (Stokes scattering) than the incoming photons. In the same way, incoming light can interact

with a vibrationally excited molecule to bring electrons back to the ground state, and the scattered photon in this case will have higher energy than the incoming (anti-Stokes scattering). From the energy difference between incoming and scattered radiation, a magnitude called Raman shift representing the vibrational energy of a mode, a unique vibrational spectrum containing structural information of the system under study can be recovered and used as a powerful characterization tool. Fig. 2.6 shows the energy diagrams for the different scattering processes described.

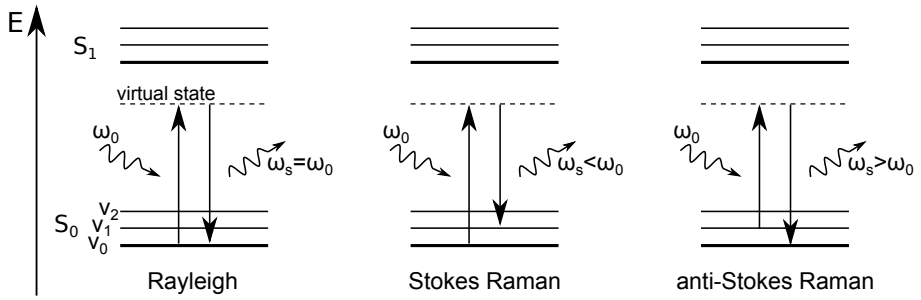

FIGURE 2.6. Energy diagram of elastic (left) and inelastic (center and right) scattering by molecules. Raman spectroscopy is based on inelastic scattering of light where incoming photons provoke transitions of electrons between the different vibrational levels (ν_0, ν_1, ν_2) of the molecule.

Mathematically, we can describe this process using a classical electromagnetic approach.[42,60] When a external electromagnetic field, $\vec{E}$, impacts on a molecule, it induces a dipole moment, $\vec{\mu}$, according to:

$$\vec{\mu} = \alpha \vec{E} \tag{2.3}$$

where α is the polarizability tensor describing the tendency of the electron density in the molecule to be distorted by the field. The polarizability is not a static parameter since it can change with the molecular oscillations, i. e. as the electron density adjusts to the nuclear motion. We can then express it as a Taylor expansion with respect to the normal nuclear coordinates:

$$\alpha = \alpha_0 + \sum_k \left(\frac{\partial \alpha}{\partial Q_k} \right)_0 Q_k + \frac{1}{2} \sum_{k,l} \left(\frac{\partial^2 \alpha}{\partial Q_k \partial Q_l} \right)_0 Q_k Q_l \ldots \tag{2.4}$$

α_0 is the value of α at equilibrium, Q_k, $Q_l \ldots$ are the normal coordinates of vibration associated with the molecular vibration frequencies of ω_k, $\omega_l \ldots$, and the subscript 0 indicates the equilibrium configuration. Neglecting higher-order terms than the linear (electric harmonic approximation), equation 2.4 can be

rewritten for one specific normal mode, Q_k, as:

$$\alpha_k = \alpha_0 + \alpha'_k Q_k \tag{2.5}$$

where $\alpha'_k = \left(\frac{\partial \alpha}{\partial Q_k}\right)_0$ is the derived polarizability. Vibration coordinate Q_k can be approximated as harmonic around the equilibrium position, Q_{k_0}:

$$Q_k = Q_{k_0} \cdot \cos(\omega_k t) \tag{2.6}$$

Additionally, for monochromatic incident radiation, $\vec{E}$ can be described by:

$$\vec{E} = \vec{E}_0 \cdot \cos(\omega_0 t) \tag{2.7}$$

Combining equations 2.5,2.6 and 2.7 into 2.3, we obtain:

$$\vec{\mu} = \left[\alpha_0 + \alpha'_k Q_{k_0} \cdot \cos(\omega_k t)\right] \vec{E}_0 \cdot \cos(\omega_0 t) \tag{2.8}$$

Using trigonometric relations, equation 2.8 can be written as:

$$\begin{aligned} \vec{\mu} = \overbrace{\alpha_0 \vec{E}_0 \cdot \cos(\omega_0 t)}^{\text{Rayleigh}} \\ + \underbrace{\frac{1}{2}\alpha'_k Q_{k_0} \vec{E}_0 \cdot \cos[(\omega_0 - \omega_k)t]}_{\text{Stokes Raman}} + \underbrace{\frac{1}{2}\alpha'_k Q_{k_0} \vec{E}_0 \cdot \cos[(\omega_0 + \omega_k)t]}_{\text{anti-Stokes Raman}} \end{aligned} \tag{2.9}$$

Equation 2.9 represents the induced dipole moment of a molecule in presence of an external EM field. This dipole is a radiation source with three terms describing different components of scattered light. The first term represents the elastic scattering (Rayleigh scattering), a radiation with the same frequency, ω_0, as the incoming field. The other two terms describe respectively Stokes and anti-Stokes Raman, i. e. inelastically scattered light at a frequency lower or higher than the incoming field, as depicted in figure 2.6. Stokes radiation is red-shifted with respect to the incoming light and represents the scattering resulting from promoting an electron from the fundamental to a vibrationally excited state. In contrast, anti-Stokes Raman results from the relaxation of molecules from a vibrationally excited mode to the fundamental, being therefore blue shifted with respect to the incoming light.

From this simple classical approximation, we can understand the selection rule for a mode to be Raman active: a mode is Raman active if there is a change in the polarizability tensor upon vibration, i. e. $\alpha'_k \neq 0$ in equation 2.9. For a more precise treatment of the scattering process a full quantum mechanical description is required. Such a discussion is beyond the scope of this work, and

therefore it will not be treated in this dissertation. For a detailed review the reader is referred to the works by D.A. Long and E. Le Ru. [42,60]

From the quantum mechanical theory of Raman scattering, other phenomena as *resonance Raman scattering* (RRS) can be theoretically understood. Briefly, RRS is detected when the incoming wavelength has an energy equal to a molecular electronic transition, i. e. in Fig. 2.6 the incoming photons possess enough energy to excite the molecules from S_0 to S_1. The intensity of the spectra from resonant molecules can be several orders of magnitude higher than normal (off-resonance) Raman intensities, and therefore RRS is very convenient to compensate for the generally very low Raman signals. Dye molecules are typical examples of resonant molecules in Raman. D.A. Long provides a detailed description of RRS in his book. [60]

2.4.1 Characteristics of the Raman spectrum

The Raman shift, defined as the loss (gain) of energy of the incoming photons after Stokes (anti-Stokes) scattering, $\mathrm{E_R} = \mathrm{E_0} - \mathrm{E_S}$ or $\nu_\mathrm{R} = \nu_0 - \nu_\mathrm{S}$, is traditionally expressed in wavenumbers (cm^{-1}) rather than frequency and corresponds to the energy of the vibrational mode. In a simplified model, one can compare a molecular vibration to an oscillating spring where the oscillation frequency follows the relation $\nu = \sqrt{\mathrm{k/m}}$, being k the spring constant and m the mass. Therefore, from the obtained vibrational frequencies of the Raman spectra, we can gain information about the interaction strength and the masses of the atoms involved in them. For example, vibrations involving double and triple bonds appear at higher wavenumbers than single bonds, while vibrations involving heavy atoms have lower Raman shift than the lighter ones.

A Raman spectrum consists of a plot of Raman intensity as a function of Raman shift, i. e. scattered intensity versus energy (or frequency). Peaks corresponding to the active molecular vibrations appear in the spectrum with different intensities, with a certain broadening usually defined as the full-width at half maximum (FWHM) of the peak. The broadening originates because excited states do not have infinite lifetime and therefore their energy is not exactly defined. As a consequence, a distribution of photons with energies centered around a central value ν_R is detected. Typical values of FWHM in Raman oscillate between few wavenumbers and few dozens. [42,60]

The power of Raman spectroscopy to efficiently characterize samples relates to the fact that the parameters defining a peak or vibration (position, intensity, and FWHM) strongly depend on the morphology and composition of the sample. For example, the chemical environment of the molecule probed affects the peak position. Changes in interaction strength between molecules and environment

(for example the substrate), or in general, any chemical reaction altering the molecular structure results in shifts of the position of the Raman lines (changes of m and/or k result in a shift of the frequency according to $\nu = \sqrt{\mathrm{k/m}}$). FWHM contains information about the crystallinity or purity of the samples. Since it is inversely proportional to the lifetime of the photon in the excited state, generally ordered samples (as crystalline solids) have narrower peaks than the amorphous configuration. The intensity of a Raman band depends on incident power, frequency, polarizability, temperature and scattering cross-section (defined as the ratio between incident power and scattered power, $\sigma = P_{scat}/P_{inc}$). The latter is usually treated in its differential form to account for the directionality of the scattering radiation:

$$\frac{\mathrm{dP_{sca}}}{\mathrm{d}\Omega}(\Omega) = \frac{\mathrm{d}\sigma_{\mathrm{sca}}}{\mathrm{d}\Omega}(\Omega) S_{inc}$$

Due to the complex relation of the intensity with different parameters, comparing Raman intensities between experiments requires fixing some experimental variables such as incident power or polarization, simplifying the dependency of the intensity on different parameters. Different normalizations can be applied to the spectra to analyze the meaning of intensity changes between different experimental conditions. For example, normalizing spectra to incident power can be used to analyze photodegradation of the sample, while normalization to a specific band intensity emphasizes relative band intensity changes. If analyzed carefully, the intensity changes of a specific band can provide information about the geometry of the sample (orientation of molecules with respect to the incoming field) through its dependency with the polarizability tensor. A detailed explanation of this through a practical example is shown in Chapter 6.

2.5 Tip-enhanced Raman spectroscopy

The main disadvantage of conventional Raman spectroscopy are the inherent low scattering cross-sections of vibrational modes of non-resonant organic molecules (in the range of 10^{-29} to 10^{-32} cm^2) [42] making it a low-sensitivity technique that can only be used to characterize bulk solid samples or highly concentrated solutions.

Enhanced-Raman techniques (SERS and TERS) make use of nanometric metallic structures to enhance and localize the electromagnetic (EM) field, leading to hot-spots acting as nano-antennas. An optical antenna is an object that converts between freely propagating (far-field) and localized (near-field) optical radiation. [61] The Raman enhancement factor produced by the optical antenna is calculated as the square of the field enhancement, i. e. g^2 with

g= $E_{enhanced}/E_{incident} = E_{near-field}/E_{far-field}$.[62] The nano-antenna enhances the incident field, g^2_{inc}, that interact with the sample resulting in near-field scattered radiation which is again coupled by the antenna into the far-field and enhanced accordingly, g^2_{sc} . Thus the total Raman enhancement factor is g^4 assuming g_{inc}=g_{sc}.[63–65] Raman signals from species in the hot-spot (near-field) are enhanced by factors of 10^7-10^{10} in comparison to conventional Raman. In this way, the technique can be extended to surface studies, where monolayer and even single molecule detection is possible. The tip apex of an SPM is the nano-antenna in TERS systems where the far-field light is focused into a highly enhanced and localized near-field region extending in the three spatial directions a few nm from the tip apex. The localization of the near-field around the antenna is the origin of the nanometric spatial resolution of near-field techniques. Spatial resolution (vertical and lateral) is treated in following sections.

The Raman enhancement is a combination of two main mechanisms: EM and chemical enhancement, with the EM enhancement being the main contribution to the total field enhancement. The chemical enhancement contributes to the overall enhancement by one or two orders of magnitude, while the rest is attributed to the EM enhancement.[42,63] The EM enhancement is based on the resonant excitation of LSP at the tip apex. The chemical enhancement corresponds to changes of the polarizability tensor upon adsorption of the molecule onto the metal (as a result of a charge-transfer between metal and adsorbate), in such a way that the modified polarizability is more resonant with the incident light than the original.[42,66–68]

Plasmons are defined as *quantum quasi-particle representing the elementary excitation, or modes, of the charge density oscillations in a plasma*[42] or, in simpler terms, plasmons are collective oscillations of the free electron gas in a metal. Different plasmons exist depending on their characteristics: When the plasmons are confined to a surface, we call them surface plasmons (SP), while if the surface is also confined (as in a nanoparticle or at the apex of an SPM tip) we talk about localized surface plasmons. The latter are the ones involved in the field enhancement in TERS and SERS. Plasmons are charge oscillations and therefore are also EM-field. As such, external fields like propagating light can interact with plasmons and excite them resonantly under appropriate conditions. Exciting directly SP at a planar surface is not possible due to momentum mismatch at the interface.To overcome this issue, momentum matching techniques as Otto or Kretschmann configurations can be used to excite SP at planar interfaces.[42] The conservation laws are relaxed when considering a metallic object with smaller dimensions than the excitation wavelength, as for example a nanoparticle. In this case, LSP can be excited by incident propagating light. The excitation of LSP results in a strongly enhanced EM field confined to the surface of the nanoparticle that originates from resonant energy

transfer between the incident light and the LSP. [36]

For the application of TERS, metals whose surface plasmon resonances lie in the visible frequencies are preferred. This is the case for coinage metals, with Au and Ag the commonly used materials for tips in TERS. The plasmonic resonances of the system depend on the material chosen, the size and shape of the tip and the surrounding dielectric medium.

2.5.1 Vertical resolution

The TERS intensity, I_{TERS}, has been shown inversely proportional to the 10th power of the tip-sample separation: [69–72]

$$I_{TERS}^{norm} \approx \left(1 + \frac{d}{\rho}\right)^{-10} \tag{2.10}$$

with d the gap distance and ρ the dipole radius (approximately the tip radius). Eq. 2.10 is derived from the consideration of an incident field exciting the LSP at the tip apex. When the LSP are excited, free electrons in the tip apex oscillate confined into the dimensions of the nanoparticle. This effect can be modelled as an oscillating dipole radiating an EM field (near-field) which decreases with the distance to the center of the dipole as $I \propto R^{-3}$ (for this model the tip apex in TERS is considered a sphere, and $R = r_{tip} + d$, being d the gap distance). Multiplying this dependency by the Raman enhancement g^4 described previously, we reach $I_{TERS} \propto R^{-12}$. By integrating over the surface area probed, the R^{-10} expression is obtained. For a detailed discussion of this model and considerations, the reader is referred to previous works. [63,70–72]

2.5.2 Lateral resolution

To address the origin of high lateral resolution of TERS, the concepts of near-field and far-field focus need to be clarified. Abbe limit of diffraction defines the maximum resolution that can be achieved with far-field optics. The lateral resolution achieved with a far-field focus is defined as $\Delta X = 0.61\lambda/\mathrm{NA}$, with NA the numerical aperture of the focusing element. Practically, this reaches an approximate resolution of $\lambda/2$ which leads to values in the range of 200-400 nm. [36] This limit is overcome in near-field approaches, where the confinement of the field to the nano-antenna (near-field focus) push this limit down and spatial resolutions of few nanometers and even sub-nm can be achieved.

The near-field or enhanced focus, of radius r_{ef}, is the projection of the near-field on the surface. The TERS radius, r_{TERS}, defined as the distance from the center

of the near-field focus where the TERS scattering intensity decays up to 1/e of the maximum value, gives the lateral spatial resolution of TERS. In a simplified model, the the near-field is considered to be confined around the whole extension of the tip apex, r_{ef}=r_{tip}, and the resolution is given by the tip dimensions. However, much lower TERS radii are found experimentally. Tip radius between 10 and 50 nm are standard in TERS experiments and lead to spatial resolutions in the range of 3-15 nm.[73–75] Different theoretical models have been proposed to calculate the spatial resolution, considering the tip size and geometry and other parameters such as the substrate employed or the gap distance. Considering the R^{-10} model described in the previous section, one can estimate r_{TERS} to be approximately half of r_{tip}. For a standard tip size of 20 nm, this leads to a resolution of 10 nm.[63] This is a conservative estimation of the achievable resolution with a given tip. In practice, sub-nanometer resolution has been achieved with 25 nm tips in gap mode configuration, allowing chemical mapping of single molecules.[27] In the next section, we describe gap-mode configuration in TERS and how it leads to improved spatial resolutions.

2.5.3 Gap-mode configuration

The nano-antenna in TERS converts freely propagating optical radiation into a localized near-field and vice versa. This concept can be extended to the substrate in the gap-mode configuration.

Upon tip illumination, a surface charge density is induced in the tip apex, that can be considered a point dipole. Since the gap distance is in the nanometric range, an image dipole is induced in the substrate if made out of a metal, usually the same as the tip. The tip-substrate plasmons are not independent in this situation, but a new hybrid mode called gap-mode plasmon is formed. Metallic substrates that exhibit gap-modes present stronger field confinement in the gap, leading to improved spatial resolution and higher enhancement factors.[65]

The lateral confinement of gap-modes has been found proportional to $\sqrt{r_{tip}d}$, being r_{tip} the tip apex radius and d the gap distance.[65,76,77] This relation implies that the field confinement can be tuned by changing the tip-sample gap and the tip radius, and therefore the spatial resolution can be improved by minimizing the tip-sample gap.[65,77] For a tip radius of 10 nm the model predicts a decrease of the lateral confinement of the near-field at gap distances lower than 6 nm (classical electrodynamics sets a lower limit of the confinement that reaches a minimum at 0.3 nm gap distance). A resolution of 3.5 nm is obtained for a gap distance of 0.5 nm. For gap distances over 6 nm the confinement reaches the limit of an isolated tip apex (normal LSP mode).[77] Because of the localization of the near-field to a smaller region, the field density in the gap is higher and

the Raman signals from the molecules in the gap are further enhanced.

2.6 Implementation of TERS setup

Up to know TERS has been treated from a theoretical point of view. In the remaining of the chapter, the main experimental considerations to take into account when building a TERS setup are detailed.

Since the first experimental reports on TERS [43–47], many efforts have been carried out to develop the technique into a standard characterization tool in surface science to study different systems in biology, physical-chemistry and materials science [26,78–85]. In air and UHV, TERS setups have been adjusted to meet the specific requirements of the system under study by, for example, choosing between STM or AFM probes for field enhancement, employing different illumination configurations, tuning the excitation laser wavelength or varying the substrate. [35–37]

The choice of experimental features and their combination (optical illumination in combination with SPM method, tip material, and excitation wavelength) define the versatilities and limitations of the resulting system. [35–37]. In this section, the different configurations of TERS systems routinely employed in air and UHV are introduced emphasizing their advantages and disadvantages. Additionally, a review of the few reports on liquid and electrochemical TERS is given, focusing on how the common TERS configurations have to be adapted in each case for experiments at the solid-liquid interface.

2.6.1 Illumination geometry

The way in which the light is coupled to the tip, or the illumination geometry, can heavily influence the TERS efficiency and poses limitations regarding the kind of samples that are accessible with a TERS instrument. The light can be focused/collected in transmission mode (bottom illumination) or reflection mode (side and top illumination) as sketched in Fig. 2.7. [37,86,87]

In bottom illumination, Fig. 2.7 left, the tip-sample gap is illuminated from underneath the sample (usually with a radially polarised beam) and the back-scattered light is collected through the same path. [80,88] In general, this illumination is limited to transparent samples but does not have space constraints; therefore it is possible to use high numerical aperture (N.A. in the range of 1.4-1.6) and small working distance objectives providing high collection efficiencies, i. e. the collection efficiency determines the amount of scattered radiation collected. In addition small laser focus are obtained, minimizing far-field con-

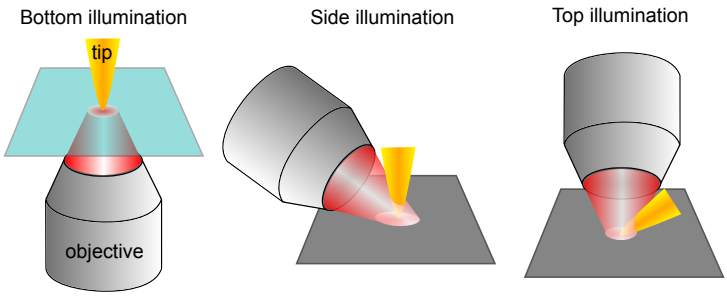

FIGURE 2.7. Possible illumination geometries in a TERS experiment: bottom (left), side (center) and top illumination (right).

tributions.[35,37,89] The requirement of transparent samples makes it difficult to work in gap-mode configuration. Nevertheless, Deckert and coworkers found a way to measure opaque samples in gap-mode with a transmission setup.[90] They use an opaque sample on a transparent substrate. The focused laser passes through the transparent side of the sample and is reflected into the tip apex by a dichroic mirror. The TERS signal is collected in the same way.

In side illumination, Fig. 2.7 center, opaque samples are accessible by focusing the laser (p-polarised) into the tip apex with a long-working distance objective at angles in the range of 45-70° relative to the tip axis.[1,27] Limited by spatial constraints due to the SPM head, smaller N.A. objectives (generally less than 0.55) are used with the consequent loss of collection efficiency. The illumination angle makes the focus spot larger and elliptically shaped, resulting in larger far-field contributions. These limitations can be overcome by working in gap mode since thick metallic substrates can be used in this configuration (as explained in Section 2.5.3).[35,37,89]

Optimal plasmon excitation for TERS requires a large component of polarized light parallel to the long tip axis.[87,91] This is the reason why in side-illumination the focusing angle is kept in the range of 45-70° with linearly polarised light (p-polarization). In bottom illumination, the high N.A. and radially-polarised light used is beneficial since it creates strong logitudinal field along the tip axis.[37,86]

In top illumination, Fig. 2.7 right, the laser illuminates the sample parallel the surface normal.[75,92] This configuration allows TERS acquisition from opaque samples and improves the focus quality (with symmetric focus spot). Despite implemented with long working distance objectives, top illumination generally leads to higher TERS collection efficiency since larger N.A. (up to 0.7) than in side illumination is possible. As a disadvantage, to avoid shadowing effects, the tip must be tilted in this configuration.[35,37,89]

A special type of top illumination consists of using a parabolic mirror instead of a lens for focusing and collection of light. Thanks to the high N.A. of the parabolic mirror (up to 1), the laser is tightly focused into the tip apex. A hole is drilled in the mirror to accommodate the tip. Accurate alignment of the mirror is required to avoid aberrations of the focus point and can be achieved by the use of piezo-stages.[37,93,94]

2.6.2 SPM technique and tip production

Mainly, TERS systems use STM or AFM as the feedback mechanism to control the tip-sample gap in TERS experiments.[35,36,86,87] In STM, the tunneling current between tip and sample is the feedback that maintains the gap distance and therefore is limited to conductive or semiconductive samples. STM-TERS usually provides signal enhancement around two orders of magnitude higher than AFM-based configurations[95,96] and high spatial resolution has been reported in STM-based systems because of the sharpness of the tips and the better control of the gap distance.[27,35,37]

AFM-TERS has a force-controlled feedback mechanism.[35,36,86,87] It is based on the interaction between tip and sample topography with resulting change in amplitude/phase (tapping mode) or in deflection of the cantilever (contact mode). It can be combined with any illumination geometry and it has no specific sample requirements (no conductivity is required). If operated in contact mode, the tip can get easily contaminated by picking adsorbates from the substrate. AFM-based setups operating in shear-force mode (SFM)[97] have also been reported.[98,99] In SFM, the tip is mounted into a tunning fork that oscillates laterally, generating a shear-force between tip and sample used as a feedback mechanism.

Obviously, tip production and quality is very different depending on the SPM technique used and plays a role in the choice of SPM for a TERS system since it affects production costs and reproducibility.[100] Full metallic tips are used in STM-TERS, produced by electrochemically etching metallic wires, i. e. by anodically dissolving the metal wire in an etching electrolyte.[101,102] The etching procedure is routinely employed due to its simplicity, however, experimental factors such as the composition of the etching solution, etching voltage, concentration of the chemicals, temperature or cut-off method can affect the final shape and size of the tip which might affect TERS experimental reproducibility. In AFM-TERS the most usual strategy consists of coating commercial silicon cantilevers with gold or silver by thermal evaporation or chemical deposition. Alternatively, fabrication of specialized cantilevers optimized for TERS applications has been achieved by functionalizing AFM tips with nanoparticles (by in

situ pick-up or selective deposition). Fully gold cantilevers specially optimized for TERS applications have also been reported.[103]

Tip material and excitation wavelength: The material of the tip determines the excitation wavelength required for optimal LSP excitation. Gold and silver are the most common material used in TERS because of their LSP resonances in the visible region, high free electron density and stability.[100] Many parameters such as the size and shape of the antenna and the surrounding dielectric influence the plasmonic resonances. In general, gold tips produce high enhancement in the red region, while the optimal enhancement for silver lies in the green frequencies. While silver produces stronger enhancements than gold and can be effectively used over a wider range of frequencies, it degrades faster, and therefore the usable lifetime of gold tips is longer which makes it a more convenient material if long experiments are required.

2.6.3 Experimental challenges

Given the small distance between tip and sample in TERS from sub-nm to few nm, it is possible that the tip picks up molecules from the substrate/environment. This contamination is an issue since the goal of the experiment is to analyze substrate/adsorbate interactions, while molecules at the tip contribute to a SERS near-field signal from the tip. Therefore every TERS experiment is routinely followed by checks for tip contamination by acquiring TER spectra with the same tip on clean substrates, or spectra when the tip is retracted by few nanometers.

Additionally, the gap distance should be controlled since it affects the spectral features. Blue shifts of the background maximum and strong reduction of both the background and peak intensities result from a gap distance increase. Therefore it is important to ensure stable gap distance when comparing results from different experiments. In Chapter 5 a detailed discussion about the relation between TERS signals and gap size is presented.

Other sources of signal fluctuations such as drift of the SPM tip or molecular blinking must be taken into consideration as well. Temperature fluctuations in the environment can cause severe drifts of the tip that results in variable signals as the tip moves and collects enhanced Raman signal from different parts of the sample. In general, the effect of the drift can be evaluated by systematically acquiring SPM images through the course of an experiment to ensure stable positioning. In addition, factors such as diffusion, photo bleaching or photo damaging of the probed molecules can result in strong fluctuations of the TERS bands.[104,105] Performing UHV and low-temperature experiments

reduce these effects. In air, acquisition of spectra at different powers can be done to control if and how molecular species have been damaged.

2.6.4 Moving into liquids

Over the last years, few groups are working on exploring how different experimental configurations can be tuned to work in liquid and EC-TERS conditions. The first report of solid/liquid TERS was published in 2009 by Zenobi and coworkers.[31] A bottom illumination geometry in an AFM-based TERS system (Fig. 2.8a) allowed the authors to efficiently measure a monolayer of thiophenol on a thin, optically transparent Au substrate with Raman enhancement factors of 5 x 10^3. In 2013, Nakata *et. al.* used a similar setup to detect lipid bilayers on mica in native aqueous environment[106].

In 2015, the groups of Ren and Van Duyne published independently the first electrochemical TERS (EC-TERS) studies.[88,107] Van Duyne and coworkers reported an AFM-based solid/liquid TERS under potential control to probe the nanoscale redox behavior of Nile Blue dye molecules.[88] They efficiently monitor the reduction and oxidation of the probed molecules in the EC-TER spectra and follow the oxidation of few molecules by plotting TERS voltammograms. A year after, the setup was employed to measure nanoscale spatial variations in the formal potential of single Nile Blue molecules.[108]

Ren's group reported for the first time an STM-based TERS approach to investigate an electrochemical interface. The use of a solid, atomically flat Au(111) substrate is enabled by a home-built fiber-based setup that features a slightly inclined substrate geometry to allow efficient light coupling from the side of the STM tip (Fig. 2.8b). They measure the TERS response of 4-PBT (aromatic molecule) at two different potential values. Protonation and deprotonation of the adsorbates are deduced from the measured TER spectral changes.

Top illumination in liquids has been reported recently in STM[109] and AFM-based systems[110]. In both cases, the thickness of the liquid layer was minimized by adding a small droplet of liquid on the sample as a way to reduce optical distortion (Fig. 2.8c).

The AFM bottom illumination approaches used by Zenobi and Van Duyne pose significant milestones in the development of solid/liquid TERS. The use of an AFM-based transmission configuration limits the user to optically transparent substrates and often provides lower signal enhancement than STM-based configurations[95,96] as discussed above. Nevertheless, TERS was efficiently measured in transparent substrates, with no additional enhancement by gap-mode configuration. In addition, in electrochemical AFM no tip coating is required as is

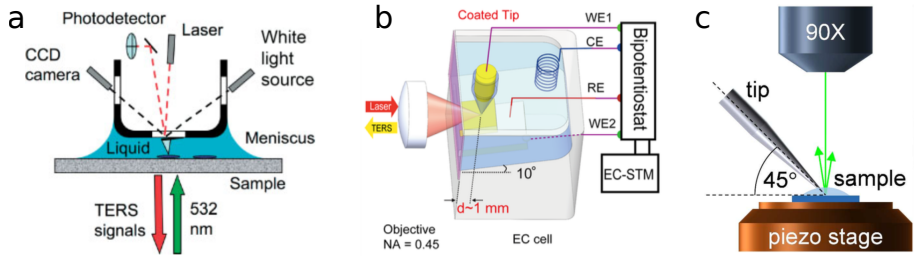

FIGURE 2.8. a: AFM-based bottom illumination setup from Zenobi's group. Reprinted with permission from Ref. [31], copyright 2009 John Wiley & Sons, Ltd. b: STM-based system in side illumination reported by Ren and coworkers, reprinted with permission from Ref. [107], copyright 2015 American Chemical Society. c: STM in top illumination approach, reprinted with permission from Ref. [110], copyright 2016 American Chemical Society.

the case for STM systems. The EC-STM in side illumination of Ren's group is more versatile in terms of sample choice. However, it requires tip coating to prevent Faraday currents flowing through the tip. Additionally, spherical aberrations of the focus point at the air/liquid interface appear in side illumination, decreasing the intensity of the TER spectra. By placing the tip close to the glass window of the liquid cell, focus distortion is minimized. To achieve it, the substrate was tilted by 10° thus affecting scanning capabilities.

The previously described works set the basis for systematic EC-TERS experiments, however, the system is still far from being fully understood and developed. There is still a lack of comparative EC-TERS studies on different molecules and environments. While AFM based EC-TERS has been demonstrated in different labs, only Ren and coworkers have reported an STM based EC-TERS system. Focus distortion in side-illumination and Faraday currents through the tip in EC-STM make difficult systematic development of this kind of instruments.

Motivated by the need of expanding further our knowledge on the main mechanisms affecting EC-TERS we reported our first liquid-TERS results in 2016, in a side illumination configuration with an STM-based setup similar to Ren's approach, however with no substrate tilting. [1] We offered a comparison between air and liquid results of resonant and non-resonant adsorbates to quantify enhancement factors and loses due to focus distortion. Additionally, in 2017 we published TERS experiments of molecular monolayers in controlled environments (argon and water) to explore the effect of the STM parameters in the liquid-TERS response. [3] Finally, we published the first STM EC-TERS study STM with a continuous potential ramp. The system was used to understand molecular reorientation of adenine molecules under potential control. [4] These

experiments are the subject of Chapters 4, 5 and 6 respectively. This thesis is devoted to the description and discussion of those experiments. In the next chapters, the setup development itself is described in detail followed by all the experimental findings.

Chapter 3

Setup development and instrumentation

The development of an EC-TERS system is one of the principal goals of the present work. Therefore, this chapter is dedicated to the introduction of our home-build setup, experimental details and technical challenges faced during the building process. The content of this chapter has been partially published previously in Refs.[1] and [4]. Text and figures are adapted with permission from *Analytical Chemistry, 88*, 7108-7114 (2016), `http://pubs.acs.org/doi/abs/10.1021/acs.analchem.6b01080`, Copyright 2016 American Chemical Society;[1] and from *Angewandte Chemie Int. Ed.*, 88, 7108-7114 (2016), `http://onlinelibrary.wiley.com/doi/10.1002/anie.201704460/abstract`, Copyright 2017 Wiley-VCH Verlag GmbH & Co. KGaA, Weinheim.[4][a]

[a] the reader is referred to the American Chemical Society and Wiley-VCH Verlag GmbH & Co. for further permissions regarding these materials

3.1 Tip-enhanced Raman spectrometer

Our STM-based setup is built in standard side illumination configuration, with a red laser linearly-polarized coupled to electrochemically etched gold tips. The main limitation of the STM is the requirement of conductive samples, however, electrochemical interfaces always feature a (semi)conductive electrode. We implemented an STM based system to take advantage of the generally higher enhancement factors (around two orders of magnitude) reported in air for STM-systems. [95,96] With side illumination we are able to work with opaque samples, which is a clear advantage in electrochemistry to analyze the behavior of thick metallic substrates, and benefits TERS measurements by making gap-mode experiments feasible. Side illumination is also an advantage with respect to top illumination because it allows us to work with bulk electrolyte solutions instead of being limited to thin liquid layers where diffusion processes are modified. The choice of gold tips coupled to a red laser was based on the quick degradation of the alternative silver tips. The main disadvantages of the chosen configuration are the optical distortion of the focus point in side-illumination in liquid and the necessity of applying an insulating coating layer to the tips. The tip coating is needed to prevent Faraday currents at the tip that would make impossible the detection of tunneling currents in the pA-nA range. These effects and the strategy we follow to overcome them are discussed in the following sections together with a full description of the different elements in the setup.

3.1.1 Optical setup and liquid cell

The main optical elements of the TERS setup are schematically depicted in Fig. 3.1. The setup, mounted on an optical table with active vibration isolation (TMC, CleanTop), is based on the coupling of a commercial STM (Keysight technologies GmbH, former Agilent 5420, equipped with a bipotentiostat for EC experiments) with a red He-Ne laser (632.8 nm; REO LSPR-3501, 35 mW maximum output power, p-polarized). The only modification of the commercially available STM for TERS usage that we performed is a few-mm elongation of the tip holder to stably accommodate the long and thus particularly fragile Au tips (visible in Fig. 3.2a). The elongation of the tip holder is required to fit the long working-distance objective in the limited space left by the STM head, ensuring mechanical stability during experiments. As a result, in our design - different from the setup geometry presented by Zeng *et. al.* [107] with a 10° substrate inclination - the flat-lying surface of the original STM geometry is maintained, thus preserving the (µm-large) scan-range specifications of the STM.

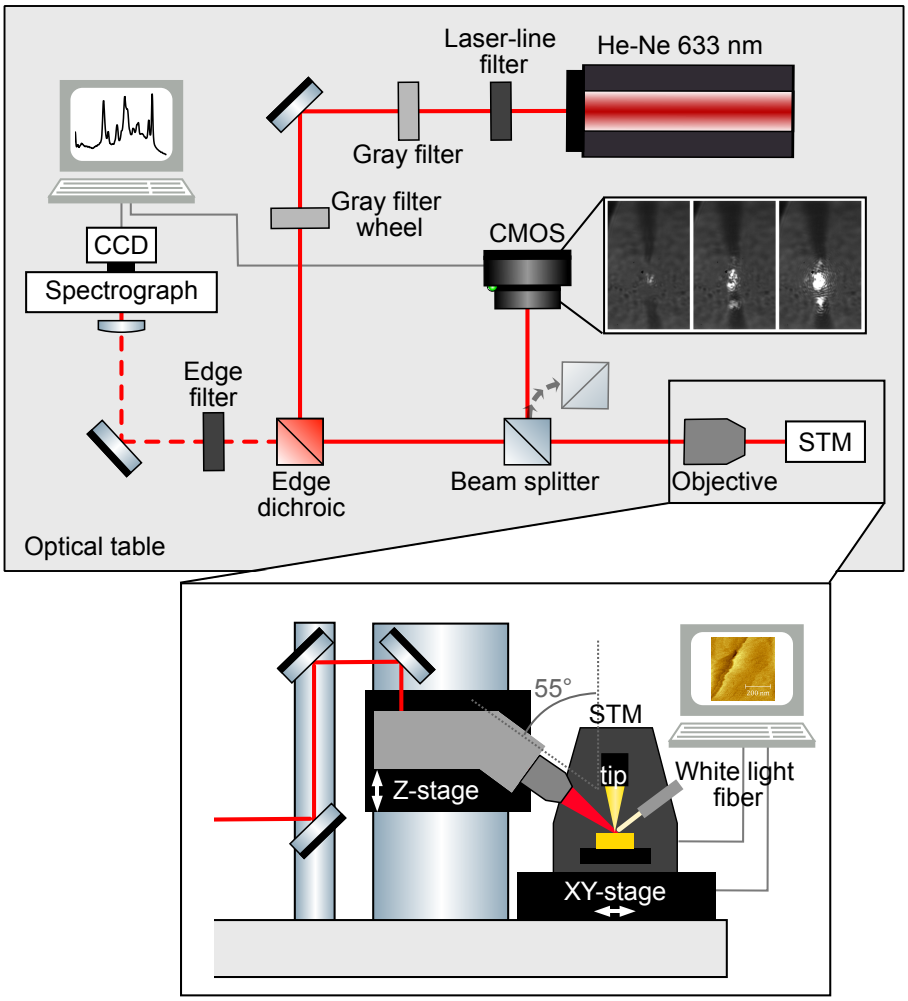

FIGURE 3.1. Top: schematic depiction of our home-built TERS setup in a top view. Bottom: detail of the coupling between incoming beam, back-scattered light and STM in a frontal view.

A laser clean-up filter (Semrock MAXLINE LL-632.8-25.0M) and different gray filters for laser beam power control (Thorlabs, filter wheel FW212C) are installed at the exit of the laser, which is directed towards the STM tip-apex in a side illumination configuration (55° between incoming beam and surface normal). Incident laser and scattered light are focused/collected through an Olympus 50X long-working distance objective (WD=10.6 mm, NA=0.5). Mirrors, pinholes and other standard optical elements were purchased from Thorlabs. A long-pass filter (Semrock RazorEdge ultra steep long-pass edge filter LP02-633RE-25) and a dichroic long-pass beam splitter (Semrock RazorEdge Dichroic LPD02-633RU-25) with cut-off values of 79 and 156 cm^{-1}, respectively, in the detection path filter out the Rayleigh elastic scattering. A Horiba iHR 550 spectrograph (equipped with 3 different gratings of 600, 1200 and 1800 g/mm) with a nitrogen-cooled CCD camera (Symphony II, Horiba) is used as a detector.

We have designed a special sample cell for the experiments in liquids shown in Fig. 3.2. The cell consists of two parts: the main body made of KEL-F and a glass window (coverslip 22x22 mm^2, 170 µm thick, Carl Roth) that is pasted to the main body with UV glue (Loctite 3321). The angle of the cell wall is such that the laser beam is perpendicular to the glass surface. The cell and the glass window can be cleaned separately. An O-ring is placed between substrate and cell to prevent solution from leaking.

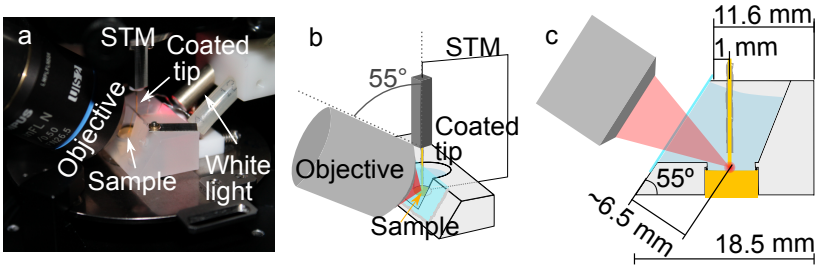

FIGURE 3.2. a: Solid/liquid TERS sample cell. b: 3D-schematic representation of the side illumination geometry. c: Side view of the liquid cell indicating dimensions. Reproduced with permission from *Analytical Chemistry, 88*, 7108-7114 (2016); Copyright 2016 American Chemical Society. [1]

3.1.2 Focusing procedure

The laser is focused precisely onto the tip apex in two steps: first, images of tip and focus are collected in a CMOS camera for a coarse focusing; second, a fine tuning of the focus is performed by optimizing TER spectra. For the first step, a white-light fiber (KL 1600 LED, Schott) is placed opposite to the objective at

an angle of 55° to the sample surface normal, as shown in the bottom part of Fig. 3.1. The white light illuminates the tip from the opposite side of the laser, it is then reflected by the sample into the objective and reaches a CMOS camera (EoSens MC 1362, Mikrotron) through a beam splitter (Fig. 3.1). In this way, an image of the shadow of the tip and the laser focus is produced, as shown in Fig. 3.3. The two tips (and laser spots) seen in the images are the tip and its mirror image in a Au(111) single-crystal substrate for different tip-sample distances. For experiments in liquid, due to the translucency of the KEL-F the liquid cell is made of, the intense white light of the fiber can penetrate through the cell walls to the sample and create similar images of tip and focus on the CMOS camera as for air experiments.

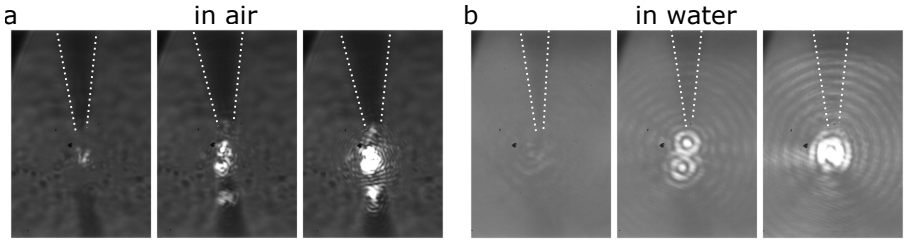

FIGURE 3.3. Microscope images of the tip-focusing process in air (a) and in water (b) when the tip is retracted more than 3 µm (left), approaching the surface (middle), and in tunneling conditions (right). Reproduced with permission from *Analytical Chemistry, 88*, 7108-7114 (2016); Copyright 2016 American Chemical Society. [1]

The STM rests on an x,y-piezo stage (custom-made by Steinmeyer Mechatronics, former Feinmess Dresden, Fig. 3.1) that allows positioning of the STM, i.e. of the tip with respect to the focus, with 3 nm precision over a maximum distance of 10 mm. An additional piezo stage serves as a base for the objective arm and moves the focus in the z-direction. In this way, focus (objective) and tip (STM) can be moved independently from each other to find the appropriate focus position on the tip apex while monitoring the focusing image with the CMOS camera. With our setup design, this focusing procedure works well both in air and in water, Fig. 3.3. The images in the CMOS can be used to find approximately the position of tip and laser spot to excite the LSP and generate a near-field signal, however being based only on the microscopic images of the camera it is difficult to find the optimal TERS enhancement.

A second focusing step is done for fine-tuning of the focus based on the TER spectra collected with the spectrograph and the CCD camera. It consists of moving the piezo-stages (in the 3 directions independently) and monitoring the TER spectral response to maximize peak intensity, i. e. the optimal focus

corresponds to the most intense spectrum. For this step, the beam splitter is moved out of its position to collect all scattered radiation.

3.2 Focus distortion

As previously mentioned, one of the main problems arising when using a side illumination configuration in a liquid TERS experiment is the distortion of the focus point when the beam has to pass through different interfaces.[111–113] In our experimental configuration, spherical focus aberrations leading to a distortion of the focal plane occur because of refractive index mismatch at the air/glass/water interfaces. According to Snell's law, the rays of the laser beam will be differently refracted at the glass window depending on their incidence angle to the surface normal, i. e. outer, middle and central parts of the laser beam will be focused to different optical planes, δf, and far away from the nominal focal plane (NFP) in air,[111–113] as graphically displayed in Fig. 3.4a. As the incidence angle to the air/glass interface decreases from the rays in the outer part of the objective window to the ones in the center, the refraction angle decreases in the water interface as predicted by Snell's law:

$$\mathrm{n_{air}} \cdot \sin(\theta_{\mathrm{inc}}) = \mathrm{n_{glass}} \cdot \sin(\theta_{\mathrm{glass}}) = \mathrm{n_{water}} \cdot \sin(\theta_{\mathrm{water}}) \tag{3.1}$$

$$\sin(\theta_{\mathrm{water}}) = \frac{\mathrm{n_{air}}}{\mathrm{n_{water}}} \cdot \sin(\theta_{\mathrm{inc}}) \tag{3.2}$$

With n being the refractive index, θ_{inc} the incidence angle and θ_{glass}, θ_{water} the refraction angles in the air/glass and glass/water intefaces respectively. This results in a larger working distance in liquid with respect to air (NFP-δf distance) and an aberrated focus point in liquid, where concentrical rings of the beam (rays with same incidence angle) are focused in a range of focal planes determined by δf. Given the characteristics of the objective (NA=0.5, WD=10.6 mm), the outer rays have an incidence angle of 30° with the glass window. δf between incident light at 30° and 1° can be calculated from simple geometrical considerations and applying equations 3.1 and 3.2. Considering for example a light path in air of 5 mm before finding the glass window, the penetration depth in water oscillates between 7.14 and 7.29 mm resulting in a δf of 152 µm. Experimentally we observe an aberrated focus in water for a range of 140 µm upon vertical movement of the objective, in agreement with the previous estimation. The distance from δf to the NFP is 1.72 mm.

The magnitude of the total focus aberrations due to refractive index mismatch (δf) scales with increasing beam path after the interface, i. e. penetration depth in glass and water.[111,112,114] In Fig. 3.4b two examples are shown where the

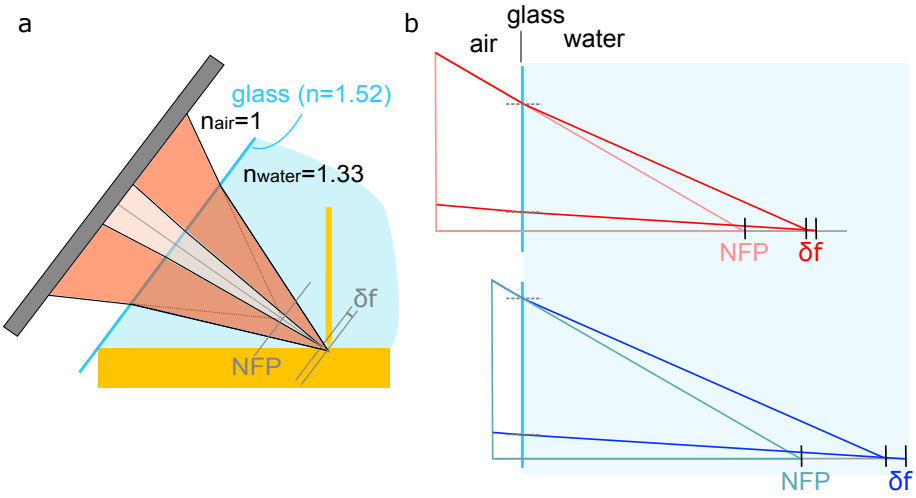

FIGURE 3.4. a: Spherical aberrations of the beam in liquid experiments arise from refractive index mismatch at the air-glass-water interface. b: The magnitude of the aberrations, or distance between the focal planes of outer and central rays in the beam (δf), scales with path in the liquid layer (the glass thickness of 0.17 mm is constant in our setup). NFP is the nominal focal plane in air.

objective is placed close (blue) or far (red) from the glass window. If the liquid cell is positioned close to the objective, the beam path in liquid is larger and δf increases as well as its distance to the NFP (blue). If the liquid cell is placed far from the objective (red, pink), the beam path in liquid is small and δf decreases. For a path in air of 10 mm, we obtain a penetration in water of 646 µm and δf of 13.4 µm, in contrast with the values for a 5 mm path in air given above.

Larger focus aberrations (may) lead to less efficient plasmon excitation due to a loss of photons in the center of the focus point, and, consequently, to lower TER enhancement. Ideally, the water layer thickness should be as short as possible, a strategy followed by Ren and coworkers in their STM-based setup, Fig. 2.8b.[107] They work with a water layer of 1 mm ensuring minimal aberrations, by illuminating at 90° with respect to the tip axis. To achieve this, the substrate is tilted to couple the beam to the tip apex.

The penetration depth in water in our experimental configuration is primarily determined by the given liquid-cell geometry (the dimensions of the cell are given in Fig. 3.2c). The width of the cell is 18.5 mm (bottom part) and 11.6 mm (top part). The tip (holder) is placed at ca. 1 ± 0.5 mm from the top edge of the glass window. This is the minimal distance that still ensures that no accidental collisions that could very easily damage the tip during the experiment. Performing simple geometrical calculations, we can estimate a liquid layer of

6.5 mm if the tip is exactly positioned 1 mm away from the top of the glass window. The liquid layer in our instrument is therefore considerably large and results in spherical focus aberrations that are clearly observed experimentally, as obvious in Fig. 3.5, where back-reflected focus images of the CMOS camera are shown for the air (a) and liquid cases (b). While the light in air is efficiently focused in a circular single focus point, in the case of water obvious spherical aberrations appear in the shape of concentrical circles.

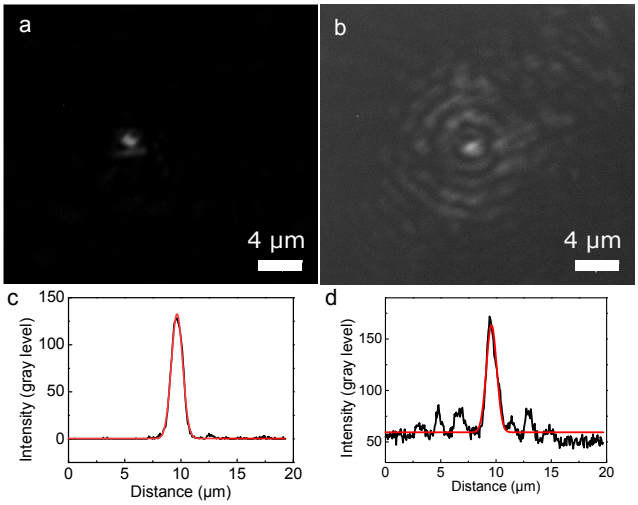

FIGURE 3.5. Images of the focus points taken with the CMOS camera in a: air at 127 µW, exposure time 10 µs, S/N=21 and b: water at 600 µW (at the exit of the objective), exposure time 40 µs, S/N=11. c: Lateral profile of the focus (black) fitted to a Gaussian profile (red) in air (d: water). Reproduced with permission from *Analytical Chemistry, 88*, 7108-7114 (2016); Copyright 2016 American Chemical Society. [1]

The average size of the focus point in air and in water can be deduced from the pictures in Fig. 3.5. From each image, five different profiles at different angles were extracted, an example of which is included in Fig. 3.5c and d. The estimated focus size corresponds to the average full-width-at-half-maximum (FWHM) extracted from Gaussian fittings to each of the different profiles measured. For the air focus, an average focus radius of 507 ± 80 nm is obtained while in water, the radius is found to be 590 ± 65 nm. Note that in the water calculation, only the area of the central peak is considered since the intensity of the further rings is smaller than the intensity at FWHM of the central spot. From these numbers, we can deduce that the larger focus in liquid implies a smaller photon density in the central spot (where the nanometric tip is placed). Additional power losses have to be considered from the photons focused on the outer rings of the aberrated focus in liquid. Therefore an important decrease if the TERS intensity in liquid experiments is expected.

Surprisingly, we realized that the effect of aberrations in our experiments is not significant enough to completely inhibit TERS signal in liquid. In our experimental configuration, we can obtain enough near-field signal to form spectra with acceptable S/N ratio, despite the intensity reduction due to spherical aberrations. The magnitude of the loss of TERS intensity in liquid experiments versus air experiments is extensively discussed in Chapter 4. Provided that collecting TERS in liquid is possible despite focus distortion, in order to compare results from different experiments it is required to keep the aberrations constant: great care has to be taken to reproducibly control the distance between the glass window and tip apex (water layer thickness).

As a control experiment, we have compared the intensity of the central far-field focus peak (curve in Fig. 3.5 d) for different tip positions at 0.5, 1 and 1.5 mm distance from the window edge, corresponding to water layer thicknesses of 6.05, 6.5 and 6.9 mm, respectively. We assume that we can control the relative position tip-glass window with a precision of $\pm$ 0.5 mm. The obtained peak intensities (after flat background subtraction) show no significant variation with water layer thickness under the given experimental conditions, with 142 $\pm$ 23 cts/a.u. (for 6.05 mm), 146 $\pm$ 14 cts/a.u. (for 6.6 mm) and 147 $\pm$ 23 cts/a.u. (for 6.9 mm). The standard deviations result from measuring five different foci for each water layer thickness. From this control experiment, we conclude that small variations of water layer thickness due to the positioning of the tip with respect to the glass window, do not affect the intensity in the center of the focus (region used for generating the near-field), and therefore the TERS intensity.

3.2.1 Aberration correction

While focus aberrations don't prevent the detection of liquid-TERS spectra, they play an important role in reducing the TERS intensity in liquid experiments in comparison to air (as it will be demonstrated in the following chapters). Focusing in liquid requires training and experience. Generally, the TERS intensity detected in liquid experiments is few orders of magnitude lower than in air. Ideally, if we got rid of the aberrations, the success rate of liquid experiments would increase and get closer to the one in air. We are working on a strategy to correct the aberrations by means of a spatial light modulator (SLM). Based on liquid crystal technology, an SLM can change the phase and amplitude of the beam pixel by pixel in an independent manner, which can be used to precompensate the spherical aberrations of the focus by finding the optimal phase value for each ray of the beam.[113,115–117]

The SLM (Boulder Nonlinear Systems, BNS-XY-PH-P256 in reflective mode,

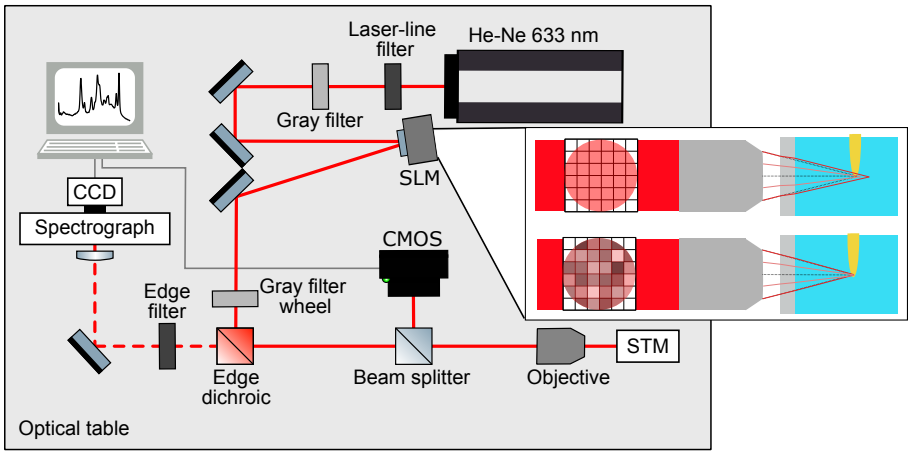

FIGURE 3.6. The SLM is mounted on the optical table in reflection mode before the dichroic mirror. Inset: Schematic of the SLM correction strategy. When the SLM is not used, the focus in liquid is distorted and presents spherical aberrations, if the optimal phase of the pixels in the SLM is found, the aberrations can be precompensated.

phase modulator) is mounted in the optical setup before the dichroic mirror, as shown in Fig. 3.6. The goal is to select the optimal phase for each pixel, resulting in the best (least aberrated) focus point, Fig. 3.6 inset. To find the appropriate phase, we have implemented an iterative method based on the stepwise sequential algorithm reported by Vellekoop *et. al.*, using the images of the focus point or the TER spectra as feedback.[116] More specifically, the phase of a pixel in the SLM is scanned while the others are kept constant and the result evaluated through the feedback mechanism. Then, for each pixel, based on the feedback result, the optimal phase value is selected and the process repeated for all remaining pixels in the SLM. Once all pixels have been evaluated, the optimal phase for each of them is applied and used as starting modulated SLM image. The pixel-by-pixel scan is repeated up to three times to improve further the results.

As feedback mechanism, we have used the images of the focus in the CMOS camera (as the ones in Fig. 3.5) being the optimal value of phase the one producing higher intensity in the center of the focus point. This algorithm is fast (in the order of few minutes) since the time required to obtain images in the CMOS camera is in the range of ms. Many parameters can be tuned in the SLM modulation algorithm to optimize the correction which have also an effect on the iteration time. With 256x256 pixels, the SLM is divided into larger super pixels to reduce dimensionality and hence the number of superpixels is one of the adjustable parameters (matrixes of 8x8, 16x16 and 32x32 have been tested).

Additionally, the different phases applied to each pixel has to be adjusted (typical values oscillate between 10 and 30 different phase values per pixels) as well as the region of interest (ROI) optimized in the CMOS image. Acquisition parameters of the CMOS images such as exposure time and framerate can also be tuned, changing the laser power accordingly. While this is a work in progress and some combinations still need to be tested, generally, an intensity increase in the center of the focus is achieved after 3 iterations of the algorithm.

As an initial approach, the modulation algorithm was tested on conventional Raman experiments to evaluate its capability to confine a distorted far-field focus. Fig. 3.7 shows the result of SLM modulation on conventional Raman spectra of MoS_2 nanotubes on Au(111) using the focus image as optimization feedback in air and water experiments. In air, the optimal focus was found and manually distorted by a vertical movement of the z-position of the objective. The distorted focus (with the light distributed over a larger area on the sample with smaller photon density) was used as a starting point for the modulation. In water, the spherical aberrated far-field focus was used as a starting point. The SLM correction always increases the intensity in the center of the focus point (evaluating an area of 500 nm diameter in the center of the focus). $I_{f,mod}/I_{f,inital}$ oscillates between 1.7 and 2.55 in this particular experiment, as indicated in the graphs for each case.

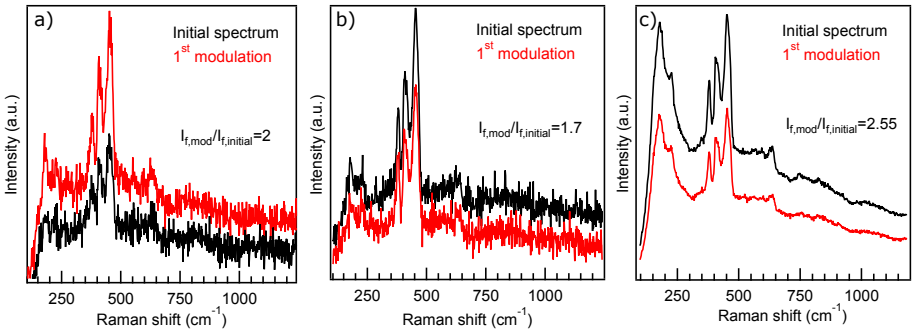

FIGURE 3.7. Representative examples pf conventional Raman spectra of MoS2 nanotubes on a Au(111) substrate corresponding to distorted focus (black) and corrected focus (red) in air (a and b) and water (c) using as a feedback mechanism the images of the focus in the CMOS camera. $I_{f,mod}/I_{f,inital}$ indicates the increase of intensity in the center of the focus point after SLM modulation in each case. The modulation always results in an increase of intensity in the center of the focus, however this does not result in an increase of Raman intensity.

Despite the intensity increase in the focus, a rise of the Raman signal is not always obtained. In Fig. 3.7a, a successful experiment is shown where the intensity of the focus doubles after one modulation. As a result, the Raman spectrum

is enhanced as well. Figs.3.7b and c, in air and water respectively, show the opposite trend. In both cases, the intensity at the center of the focus increases, but the resulting Raman spectra present lower intensities. This behavior can be partially explained by the inhomogeneous coverage of MoS_2 tubes on the substrate: a more confined and intense focus might result in a smaller amount of tubes being within the far-field focus and producing signal.

Samples with homogeneous coverage, like molecular monolayers on a flat substrate, give better results with this modulation algorithm. As an example, the effect of the focus correction in a TERS experiment of a monolayer of thiophenol (PhS) on a Au(111) electrode in air is presented in Fig. 3.8. The increase of TERS intensity for 3 consecutive modulations using the images of the focus as feedback is shown. The initial (non-corrected) spectrum is showed in black and the modulated ones in pink-red. An obvious increase of TERS intensity is achieved by sequentially optimizing the intensity of center of the far-field focus (where the tip is later placed to generate the near-field). The intensity of the stronger bands at 998, 1020 and 1074 cm^{-1} increases by a factor of 6.2, 4.5 and 10 after 3 iterations, respectively. More importantly, the appearance of a previously undetected band at ca. 415 cm^{-1} in the second and third modulations proves the capability of this correction strategy to improve the sensitivity of TERS experiments.

While promising, the modulation based on the focus images not always results in an increase of TERS intensity as the case of conventional Raman experiments in inhomogeneous samples. Further experiments need to be done to find the appropriate parameters for optimal correction and to understand how a far-field focus correction affect the intensity of TERS bands and backgrounds. As an alternative approach, we have tried to directly use the TER spectra as feedback mechanism and select the phase value for each pixel based on the maximum intensity of the TERS bands. While this method produces better results in recovering TERS intensity losses, the iteration algorithm takes longer (usually several minutes), since the acquisition time of TER spectra is in the order of seconds.

To use this modulation, one has to decide which part of the spectrum is gonna be optimized by the algorithm. TERS experiments of a monolayer of PhS on Au(111) were performed to test the new approach. In Fig. 3.9a, results of an optimization based on maximizing the total intensity of the spectrum (including the background and all Raman bands) is shown. After 2 iterations convergence was reached. In this case, the intensity of the same bands considered before at 998, 1020 and 1074 cm^{-1} increases by a factor of 3.13, 8.21 and 4.01 respectively. If the intensity of a single band is used as feedback mechanism (Fig. 3.9b), the intensity increases by a factor of 1.34, 1.84 and 1.31 for the at 998, 1020

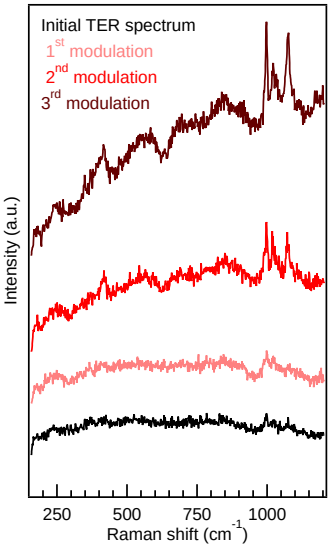

FIGURE 3.8. Effect of SLM modulation on the TERS spectra of a monolayer of thiophenol on Au(111) using focus image as feedback mechanism. Initial TERS spectrum before modulation (tunneling parameters: 1 nA and 0.1 V, black) and spectra after the first (pink),second (red) and third (dark red) phase modulations in the SLM taking as optimal phase level for a pixel the value providing the highest intensity at the center of the focus point on the CMOS camera.

and 1074 cm^{-1} peaks respectively after one iteration. Further optimization by additional iterations was not successful. In both cases, the band at 415 cm^{-1} is recovered after the modulation.

So far all the tests performed with a modulation based on spectral features have resulted in a rise of TERS intensity. The modulation has still to be tested adjusting the variables such as the number of super pixels, number of phases in the SLM or spectral region optimized. This approach is very recent and we have not found yet the optimal modulation strategy, however it is likely more appropriate for TERS optimization given the preliminary results: it always results in a Raman intensity increase in contrast to the modulation based on focus optimization where roughly 50% of the times tested, the focus intensity increase did not relate to a TERS intensity increase.

In view of the results presented, we conclude that beam modulation is a promising strategy not only to compensate the losses of intensity due to focus distortion but also to push the TERS sensitivity to higher limits in air, liquid, and electrochemical environment. In the remaining of this thesis, all the experimental results presented were obtained without beam correction.

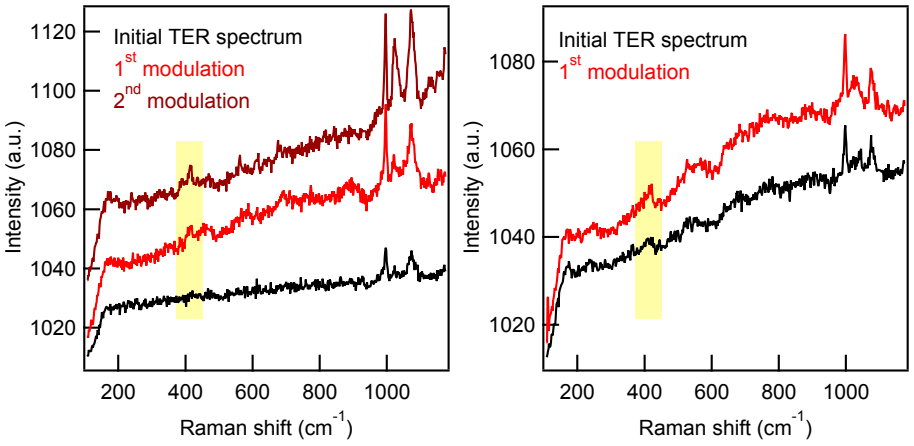

FIGURE 3.9. Effect of SLM modulation on the TERS spectra of a monolayer of thiophenol on Au(111) using spectral features as feedback mechanism. Left: initial TERS spectrum (tunneling parameters: 0.5 nA and 0.1 V, black) and spectra after the first (red), second (dark red) phase modulations in the SLM taking as a feedback the overall Raman counts (including peaks and background). 5 sec. acquisition and 500 μW. Right: Same selecting as a phase level for a pixel the value providing the highest intensity of the Raman band at 999 cm^{-1} (background subtracted). 1 sec acq. and 200 μW.

3.3 Electrochemical TERS

EC-TERS experiments are performed on the previously described optical setup and the electrochemical control is provided by the bipotentiostat of the STM. Therefore the only modification with respect to the liquid and air experiments consist in operating the STM in electrochemical mode and placing the counter and reference electrodes on the same liquid cell described above.

In the bipotentiostat, tip and sample are both working electrodes and their potentials can be controlled independently versus the RE, while they are related through the bias potential, E_b, applied to generate tunneling conditions:

$$E_b = E_{sample} - E_{tip} \tag{3.3}$$

$$E_{sample} = WE_2 - RE \tag{3.4}$$

$$E_{tip} = WE_1 - RE \tag{3.5}$$

Fig. 3.10 shows an sketch of the setup (left) and the relations between potentials of the sample, tip, RE and bias (right).

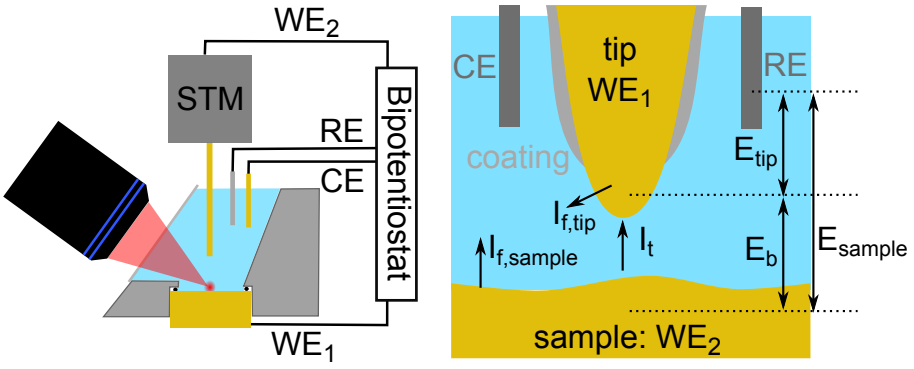

FIGURE 3.10. left: sketch of the EC-TERS configuration and electrodes. Reproduced with permission from *Angewandte Chemie Int. Ed.*, 88, 7108-7114 (2016); Copyright 2017 Wiley-VCH Verlag GmbH & Co. KGaA. [4] Right: zoom into the tip apex region, indicating Faraday currents (I_f of tip and sample) and tunneling current (I_t); adapted from [34].

When ramping E_{sample} during an EC-TERS experiment, given the previous relations, it is possible to operate either at constant E_b and variable E_{tip}, or vice-versa. Operating at constant bias has the advantage of keeping constant the tip-sample distance. This is important because the gap distance affects greatly the intensity of the TERS peaks (this topic is treated in detail in Chapter 5); if the gap distance is affected as a result of tuning the bias, intensity changes in the spectra cannot be unambiguously attributed to changes in the electrochemical interface but to a combination of both surface chemistry and gap distance change. Therefore, we operate always at constant E_b. In this configuration, when the potential of the sample is ramped, the system has to adjust automatically the tip potential to keep their difference, E_b, constant. In turn, changing E_{tip} may induce electrochemical processes at the tip, that depending on the potential range scanned can result in a tip contamination. For example if, as a result of varying E_{sample}, molecules are desorbed from the electrode surface, these can be adsorbed at the tip surface. Molecules adsorbed around the nanometric tip apex, where the nearfield is created, produce SERS signal, thus the measured nearfield spectra in this situation contain signal from the molecules at the sample surface and the tip apex. It is therefore important that prior to starting an EC-TERS experiment, we know the voltammetric response of the system so the potential values (E_{sample} range and E_b) are chosen to minimize or prevent possible electrochemical reactions in the tip. The sign of the bias can be changed to keep the tip potential higher or lower than the sample depending on what is more convenient for the specific system probed, and the magnitude of the bias can be chosen so the potential range applied to the tip does not reach electrochemical processes at the tip (choosing a range where no

oxidation/reduction peaks appear).

Additionally, in an EC-STM experiment, Faraday currents at the tip surface ($I_{f,tip}$ in Fig. 3.10) have to be minimized to maintain the tunneling current through the tip as the main current contribution. Note that only the total current through the tip can be measured by the STM (tunneling current between sample and tip and Faradaic/non-Faradaic processes contribute to the total current measured) and the value obtained provides feedback to the STM to adjust the gap distance. The leakage current (defined as every contribution to the total current flowing from/to the tip not coming from the tunneling process, i. e. Faradic and non-Faradaic currents) has to be at least couple of orders of magnitude lower than the tunneling current, so the tip-sample distance can be controlled properly ($I_{f,tip} << I_t$). To do so, the tips in EC experiments are coated with a protective insulating layer that leaves exposed only the tip apex to allow tunneling current in the gap region. The process is explained in detail in the next section.

3.3.1 Electrodes in EC-TERS experiments

Due to the limited space in the liquid cell, we need to use micro electrodes. In the experiments presented in this work, a gold wire (Mateck, 5N, 0.25 mm diameter) is used as the counter electrode (CE) and cleaned prior to use by soft flame annealing for a few seconds followed by rinsing with MilliQ. A homemade Pd/H_2 wire is used as RE.

The RE is prepared electrochemically before use. A palladium wire (Mateck, 0.25 mm diameter, 99.95% purity) is flame annealed and rinsed with Milli-Q water before immersion in a 0.1M H_2SO_4 solution. A ring-shaped Au wire (0.25 mm diameter, 5N purity, Mateck), cleaned in the same way, is immersed in the solution and used as a counter electrode. A voltage of 5 V is applied between the Pd wire and the Au CE during 5 min approximately to allow hydrogen adsorption. During hydrogen adsorption visible bubbles are produced around the Pd wire. Bubbling starts increasing slowly after potential is applied until a strong flow is observed. After few minutes, the amount of bubbles decrease and the electrode is ready. At this moment the Pd wire is taken out of the acid, rinsed with Milli-Q and mounted into the EC-TERS cell immediately after preparation.

3.4 Tip preparation

To achieve a TERS active tip (with a sharp symmetrical pencil-shaped apex), we perform electrochemical etching of gold wire in a 1:1 solution of ethanol and fuming HCl.[100,101] Au wire of 0.25 mm diameter (5N purity, Mateck) is cut in pieces of roughly 1.5 cm length (the length is determined by the dimensions of our sample cell). The wire is cleaned by rinsing with ethanol and MilliQ water and a soft flame annealing. Another gold wire of 0.5 mm diameter (5N purity, Mateck) is bent in a circular shape and used as counter electrode. The tip is held vertically in the center of the circular counter electrode, a couple of mm inside the solution as shown in Fig. 3.11; this scheme ensures a symmetrical etching of the wire. A constant DC voltage of 2.4 V is applied between electrodes to drive the electrochemical etching. The etching device that supplies the voltage between electrodes is a home-made DC (variable) voltage generator, which allows monitoring the electrochemical current flowing through the tip. Fig. 3.12 shows a typical current-time curve for a complete tip etching, lasting around 6 minutes. The average of the measured current decreases with time as the wire is getting etched at the air-electrolyte interface and less surface is exposed to the solution, red line in Fig. 3.12. When the neck is thin enough, the lower part falls down and no more current is measured. The etching device takes the measured current as a feedback to control the etching process: when the current detected drops close to zero, the voltage is switched to open circuit potential automatically and the tip is pulled up from the solution by a magnet connected to it and controlled by the etching device. After etching, the tips are rinsed with MilliQ to remove any residual etching solution.

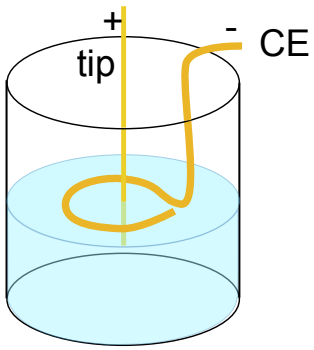

FIGURE 3.11. Electrodes geometry for tip etching.

In Fig. 3.12 (inset), a detail of the current measured during few seconds is given. As observed, a high frequency oscillation of the current is measured with average value decreasing over time as a result of etching. The oscillations originate

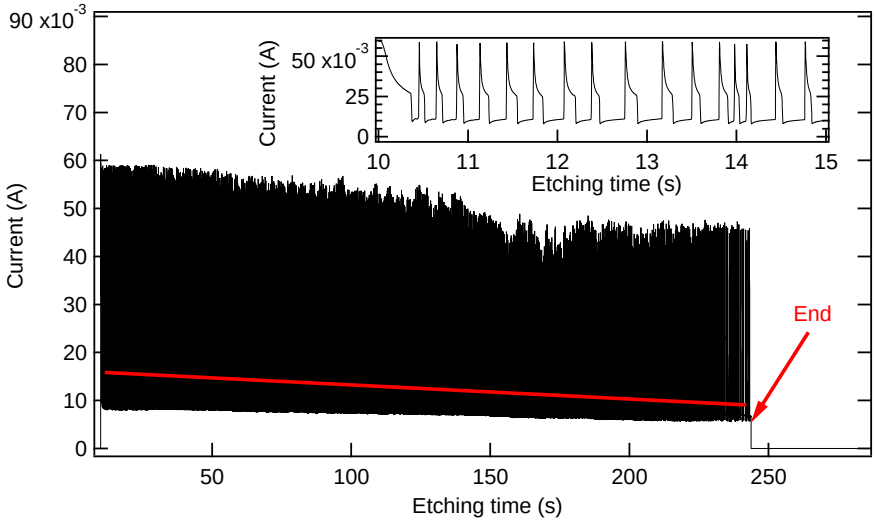

FIGURE 3.12. Typical current versus time curve obtained while etching a gold wire to produce a TERS tip. The red arrow indicates the end of the etching when the measured current drops to zero. The red line indicates the linear decrease of the average current with time. Inset: detail of the etching current during 5 seconds period showing the high frequency oscillations resulting from a change of concentration of Cl^- locally around the gold surface.

from depletion and resupply of Cl^- around the gold wire during the etching, as a consequence of the electrochemical reactions taking place in the described system:[101,118]

$$\mathrm{Au} + 4\,\mathrm{Cl}^- \longrightarrow \mathrm{AuCl}_4^- + 3\,\mathrm{e}^-$$
$$\mathrm{Au} + 2\,\mathrm{Cl}^- \longrightarrow \mathrm{AuCl}_2^- + \mathrm{e}^-$$
$$\mathrm{AuCl}_2^- + 2\,\mathrm{Cl}^- \longrightarrow \mathrm{AuCl}_4^- + 2\,\mathrm{e}^-$$

While etching the gold wire, these reactions consume a large amount of Cl^- at the interface, leading to a local decrease of $[Cl^-]$ next to the gold surface which leads to the formation of gold oxides. Gold oxides passivate the surface resulting in a decrease of current.[100,101,119] As the Cl^- ions are resupplied from the bulk solution, oxide dissolution is facilitated leaving the bare gold exposed with the consequent current increase. This process is repeated constantly leading to the observed oscillations.

This method has been used for producing TERS probes for STM for years, however reproducibility of tips has been found to be extremely dependent on the experimental parameters such as etching voltage, concentration of chemicals,

temperature, bubble formation in the counter electrode as a result of reduction reactions etc.[118] In our experience, not more than 50% of the tips produced leads to large TERS enhancement, and therefore for a TERS experiment several tips need to be prepared. This is the first step of tip preparation needed for air, liquid and EC experiments.

3.4.1 Tip coating

In the case of electrochemical experiments, an insulating coating layer has to be applied to the whole wire except for the apex, to prevent leakage currents interfering with the tunneling current that keeps the tip-sample distance. The requirements for the coating material are:

- To be electrically insulating chemically and stable (not dissolving) in the electrolyte.
- To be clean in order not to contaminate the electrodes and electrolyte.
- To be a non-fluorescent material to avoid fluorescence background in the TER spectra. Fluorescence is around 10^10 times stronger than Raman, and therefore if present, it may easily mask the weak Raman peaks.

The common coating materials used in EC-STM, such as Apiezon wax, Epoxy or nail-varnish[34,120] are insulating and prevent Faraday currents, however not suitable in our experience for TERS applications either because they produce fluorescence backgrounds or because they dissolve in our electrolytes. We found that Zapon lack (CLOU, Germany) fulfills all the requirements and can be used as an effective coating material for the TERS probes.

The coating method is the same as used in EC-STM applications. A thin insulating coating layer of Zapon lack is applied onto the etched Au wires in the following way (Fig. 3.13): A small droplet of Zapon is poured into the groove of a U-shaped Cu wire with a 2 mm wide groove. The Zapon droplet spreads inside the groove forming a thin layer. The bottom part of an etched Au tip is held vertically (perpendicularly to the Cu-wire groove), with the apex pointing up, moved sideways into the droplet of Zapon, and pulled down through the Zapon droplet. When the bottom part of the tip is inside the droplet of Zapon, the etched tip should go down slowly at a constant speed and vertically in order not to bend the tip apex, allowing all surface area of the wire to go through the Zapon droplet, including finally the apex at the end (top part). While the tip goes down, a thin layer of Zapon attaches to the walls of the Au wire while the tip end stays free of Zapon because surface tension on the sharply curved

apex breaks the coating. (In the experiment, the coating-free apex allows the tunneling current to pass). The coating procedure is repeated three times, with a waiting time in between of 3 to 5 minutes to allow the layers to dry. While waiting, the tips are kept vertically, with the apex pointing up, to allow excess Zapon to flow down the wire until dried. Fig. 3.13 a-c shows images of the coating process, d and e show SEM images of an etched and coated tip apex in different magnification scales. Fig. 3.13 d, shows the opening of the coating at the tip apex of approximately 10 µm. In Fig. 3.13 e, a tip apex of around 50 nm diameter can be seen.

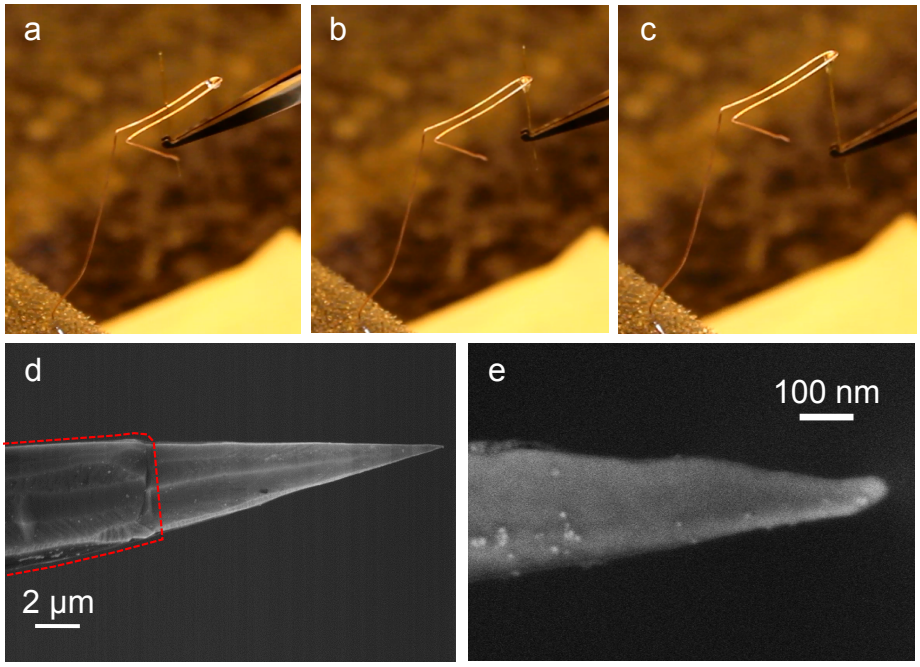

FIGURE 3.13. (a)-(c) sequence of images of the coating procedure. (d) and (e) SEM images of a Zapon-coated Au tip. Red dashed line in (d) indicates where the coating ends. Reproduced with permission from *Analytical Chemistry, 88*, 7108-7114 (2016); Copyright 2016 American Chemical Society. [1]

As explained Section 3.3, the requirement for a coating to be valid is that it keeps the leakage current significantly lower than the tunneling current. The coating procedure is, as the etching one, highly dependent on experimental conditions such as the viscosity of the zapon, groove width, user etc. Even in the same batch of tips, only a percentage of about 50% of them finish with an aproppriate coating. In our experiments, we measure the leakage currents in the STM oscilloscope prior to tunneling conditions. Normally, in electrochemical conditions we work at constant current mode with setpoint values, I_t, of around

1 nA. Therefore every tip with leakage currents larger than 100 pA is discarded for TERS and re-coated. In Fig. 3.14, the current measured for a well-coated (top) and a bad-coated tip are presented as an example.

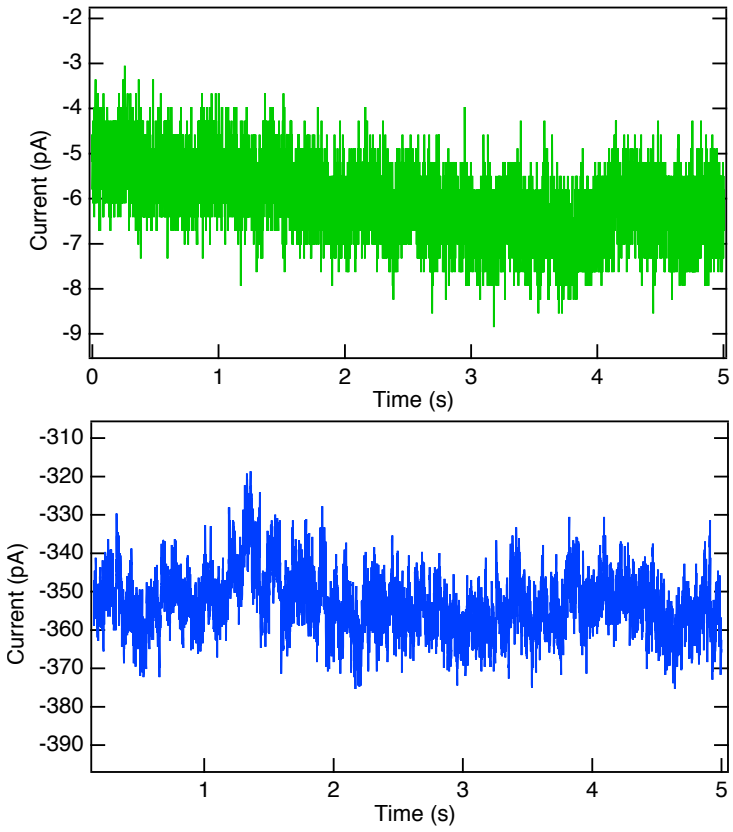

FIGURE 3.14. Leakage currents flowing through a well coated tip (top) and a bad coated tip (bottom). Recorded with the STM, at E_{sample}=0.65 V and E_{tip}=0.30 V in electrochemical mode, on a gold substrate in contact with 0.01M H_2SO_4.

While the coating is strictly needed only for electrochemical experiments (MilliQ water has high resistivity over 18 MΩ/cm and therefore the leakage should not be predominant in pure liquid experiments), the coating layer results in more robust tips that, in our experience, are more difficult to damage. Therefore we use coated tips for all our experiments to provide endurance and robustness to the tips.

3.5 Sample preparation: cleaning procedure, substrates and monolayers

3.5.1 Contamination issue

In a TERS experiment, we usually aim to capture Raman signals from a very small number of molecules. This great feature that yields sub-monolayer and even single molecule sensitivity, involves also a challenging issue: surface contamination of just a few molecules, can show up in the TERS spectra and mask the bands of the system under study. It is therefore of great importance for the reproducibility and success of our experiments to work under very clean conditions especially since we work in air and liquid environments where ambient contamination can easily affect the results. This requirement for TERS experiments is also a must in electrochemistry where contamination of the electrolyte can greatly affect the surface properties being measured.

Therefore, a crucial step in all our experiments is to clean carefully all parts and tools used. Gloves are worn at all times to avoid contamination of components, Teflon tools are used whenever possible and fine metallic tweezers are wrapped with Teflon tape. All glassware, Teflon tools, liquid cell, coverslips and substrates have to be cleaned from any organic contaminant. We achieve it by immersing them in piranha solution (H_2SO_4 : H_2O_2 of 3:1) over night, followed by rinsing in boiling MilliQ water (Ultrapure water, Millipore-Q with a resistivity higher than 18 MΩ/cm). Non-delicate parts such as glassware and Teflon tools are kept together in pyranha in large glass beakers (2-5 L). Pyranha is removed carefully and the whole container is fully rinsed at least 4 times to remove all leftovers of piranha. After that, the container (with the tools inside) is filled with MilliQ and heated in a hot plate until the water boils. The boiling water is removed and the whole process (rinsing and boiling) repeated consecutively for 3 times. To prevent damage of the delicate components, gold substrates and liquid cell are rinsed separately for several minutes with MilliQ at ambient temperature, followed by rinsing with approximately 50 mL of boiling MilliQ (heated separately in a clean beaker). H_2O_2 (18304, 34.5-36.5%) from Sigma-Aldrich and sulfuric acid (purity $\geq$95%) from FisherChem are used for piranha preparation. Starting clean does not ensure cleanliness of the surface and electrolyte during the hour-long experiments. In order to keep the surface free of contaminants, we apply a gentle argon flow on top of the sample/liquid cell through a Teflon tube placed right next to the white light, as seen in Fig. 3.2 a.

3.5.2 Substrate preparation and monolayer adsorption

In all the experiments presented in this thesis, we work with gold substrates. Au(111) is easy to prepare and clean. It allows us to work in gap-mode, and its structure is well-defined which facilitates the interpretation of results. A cylindrical (10 mm diameter, 4 mm height) Au(111) single crystal of 5N purity (Mateck) is used as substrate in all experiments. Once cleaned, the single crystal is flame-annealed according to the Clavilier method,[121], cooled in Ar atmosphere (5N, Westfalen) for 5 to 10 minutes and either immersed in the respective adsorbate solution or kept clean immersed in MilliQ water in a clean container.

For adsorption of a molecular monolayer, the clean gold electrode is immersed in an aqueous (or ethanolic) solution containing the species under study for a specific amount of time dependent on the particular system. The specific details of each experiment will be provided in the corresponding chapter.

3.6 Conclusions

The combination of a Raman platform with an SPM and the electrochemical/liquid environment results in a large list of possible combinations of experimental configurations. In this chapter, an overall introduction to the main experimental aspects of a TERS instrument is provided and followed by extensive discussion about the advantages and challenges of our particular setup.

Because of the side illumination, we can access opaque samples, however at expenses of an intensity decrease in liquids due to focus distortions. The STM provides high enhancements but requires a tip coating to operate.

Given the building details and introduction to our approach, the following chapters are focused on evaluating the performance of the setup. In Chapter 4, the initial trials of the machine on a simplified solid/liquid interface are provided. The chapter is focused on the comparison of in-air and in-liquid experiments to quantify the effect of the focus aberrations and other experimental parameters. Chapter 5, motivated by the results of Chapter 4, focuses on analyzing the effects of STM parameters (bias and tunneling current) on the TER spectra. Last, in Chapter 6, electrochemical experiments are introduced and the potential of the setup to interrogate molecular reorientation and chemical changes demonstrated.

Chapter 4

Tip-enhanced Raman spectroscopy in liquids

A first step toward the development of an EC-TERS setup is to optimize TERS experiments at solid/liquid interfaces. On the one hand, liquid-TERS reveals a new exciting field of application of the technique with more realistic working conditions than air and UHV experiments for many real-life systems. On the other hand, it allows to compare the enhancement and near-field effects in liquid versus air (or UHV) and evaluate the effect of aberrations in the overall device sensitivity without additional complications such as leaking currents or chemical conversion at the surface. To prove the efficiency of our setup in liquid environment, showcase resonant dyes are first measured, followed by the more general case of non-resonant adsorbates. The results suggest that beam aberrations due to the presence of the aqueous phase are small enough not to limit TER signal detection while the STM parameters are found to play a crucial role for solid/liquid TERS sensitivity. Raman enhancement factors of 10^5 at µW laser power demonstrate the great potential of presented experimental configuration for solid/liquid interfacial spectroscopic studies.

The content of this chapter has been published previously in Ref.[1]. Text and figures are reproduced with permission from *Analytical Chemistry, 88*, 7108-7114 (2016), `http://pubs.acs.org/doi/abs/10.1021/acs.analchem.6b01080`, Copyright 2016 American Chemical Society.[1] [a]

[a] the reader is referred to the American Chemical Society for further permissions regarding these materials

4.1 Materials and methods

The reference samples discussed in this chapter are monolayers of malachite green isothiocyanate (MGITC) and thiophenol (PhS) on Au(111) single crystals. These systems have been studied widely with TERS in air [122–124] and thus are useful to benchmark the instrument performance in terms of stability and sensitivity. Both species are known to form chemisorbed monolayers through stable S-Au bonds which limits molecular desorption in the liquid experiments. MGITC is electronically resonant with the excitation wavelength, which significantly facilitates signal detection as it leads to approximately two orders of magnitude higher TER enhancement than for nonresonant species. [125]

MGITC was purchased from Setarech Biotech. All other chemicals were purchased from Sigma-Aldrich in the highest purity available. MilliQ water was used for the liquid experiments. $5{\cdot}10^{-5}$ M and 10^{-5} M ethanolic solutions of MGITC and PhS, respectively, are freshly prepared before use. After annealing of the substrate, it is left in the solution for 12 hours and then rinsed carefully with ethanol to remove multilayers.

Since the goal of these experiments is to evaluate the performance of the system in air versus liquid environment, we compare spectra taken in air and in water with the same (coated) tip, normalized to the same acquisition conditions. Before spectral acquisition, STM imaging is performed to localize a flat gold terrace where the spectra are taken. To prevent sample degradation, the laser beam is turned on only for the focusing procedure and spectra acquisition, and off for STM imaging and waiting time between air and liquid experiments. For both air and water experiments, a gentle argon flow is injected into the cell-sample environment to prevent oxidation and/or contamination of tip and sample.

4.2 Resonant liquid TERRS: MGITC/Au(111)

4.2.1 Results

As shown in Fig. 4.1, the quality of the STM images obtained in air (a) and water (b) with long Au TERS tips is reasonable. Atomically flat terraces and monoatomic Au steps (average height of 0.19 ± 0.05 nm in air and 0.18 ± 0.02 nm in water) can be discerned proving that our solid/liquid TERS setup design does not compromise the STM performance. Atomic resolution to visualize individual molecules cannot be reached in these experiments due to the soft gold tip, its length and the fact that the STM is not completely isolated from

the environment to reduce acoustic and mechanical noise.

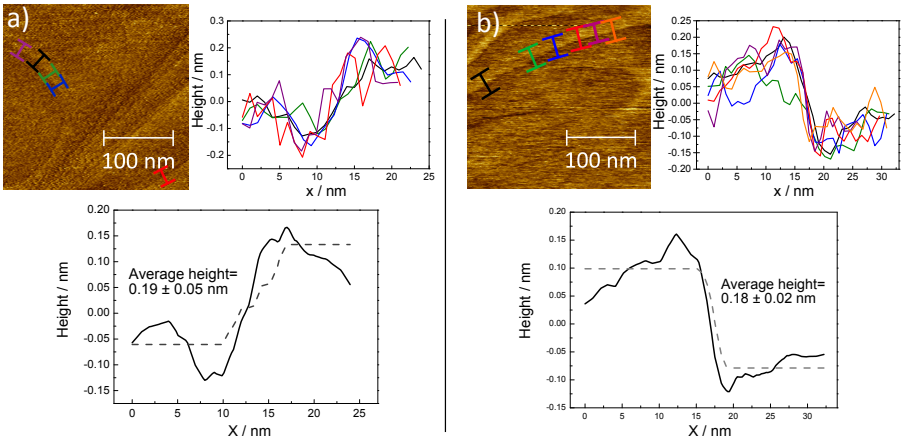

FIGURE 4.1. (a) STM image in air (top left), individual plots of the profile lines drawn in the STM image (top right), average profile (black) and fitting (gray dotted line) to a step function to estimate the height of the Au steps (bottom). (b) Same in MilliQ. Reproduced with permission from *Analytical Chemistry, 88*, 7108-7114 (2016); Copyright 2016 American Chemical Society. [1]

To calculate the height of the terraces of the Au(111) substrate, we analyzed five individual line profiles in the air image and six in the water image using the image processing software Gwyddion. The settings of the STM were adjusted in each case to produce the best image quality (E_b=0.4 V, I_t=0.1 nA in air, E_b=0.44 V, I_t=1.22 nA in water), and the images were flattened and denoised by 2D-FFT filtering. 30-pixel wide lines were employed for the individual profiles, plotted next to the STM images in Fig. 4.1. To estimate the average height of the steps observed in the images, the profiles were fitted to a step function and the height measured for each of them. Averaging the heights measured along the steps, we obtained 0.19 and 0.1 nm for air and water images, respectively, in agreement with the expected value of 0.2 nm from literature. [126] In Fig. 4.1 (bottom) an average of the individual curves as well as the fitted step functions are presented for both air (a) and MilliQ (b).

Fig. 4.2 shows TER resonant (TERR) spectra of MGITC/Au(111) in air (a, black) and in MilliQ (c, blue). Individual spectra are Savitsky-Golay smoothened (least-squares fit of second order polynomial to domains of 11 data point size). The acquisition parameters used in the experiments were 3 s exposure time and a power at the exit of the objective of 150 µW for air (700 µW for water); for clear comparison, all spectra are normalized to 2 mW laser power and 1 s acquisition time. The corresponding far-field spectra at a

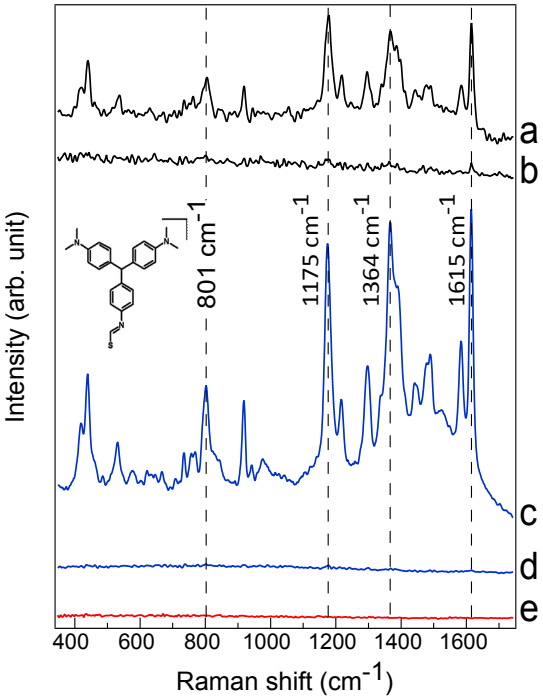

FIGURE 4.2. Raman spectra of MGITC/Au(111) in air (a,b) and in MilliQ (c,d); e: tip check. a: TERR in air (E_{bias}=0.4 V, I_t=0.1 nA); b: far-field Raman with 20 nm tip retraction in air; c: TERR in MilliQ water (E_{bias}=0.04 V, I_t= 1.2 nA); d: far-field Raman with 20 nm tip retraction in water. All spectra are normalized to 2 mW power and 1 s acquisition time, and y-offset for clarity. Inset: MGITC. Reproduced with permission from *Analytical Chemistry, 88*, 7108-7114 (2016); Copyright 2016 American Chemical Society. [1]

tip-sample distance of 20 nm are shown below the respective near-field TERR spectra (b: air; d: water; a zoom into the far-field spectra with better visible far-field signals can be found in Fig. 4.3). E_b and I_t were chosen such as to achieve most stable imaging, or tip-sample gap (air: I_t =0.1 nA, E_b =0.4 V; water: I_t =1.2 nA, E_b =0.04 V).

The TERR spectra show a clear fingerprint of the dye molecules in both air and water where all main MGITC bands are well resolved and band positions agree excellently with the ones reported previously. [122,123] The 1:3 ratio of the band intensities at 1584 and 1615 cm^{-1} indicates a chemically intact MGITC monolayer with no signs of degradation. [78]

After all experiments, the tip cleanliness was checked in a TERS experiment

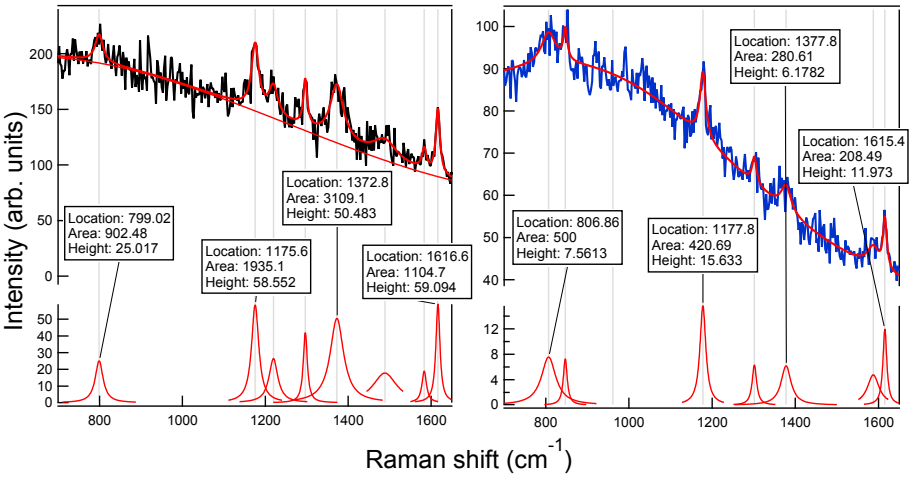

FIGURE 4.3. Far-field Raman scattering from MGITC/Au(111) in air (left) and in water (right) with Lorentzian fits to the most prominent bands. The fitting values are used to calculate the EF. Reproduced with permission from *Analytical Chemistry, 88*, 7108-7114 (2016); Copyright 2016 American Chemical Society. [1]

on a clean Au(111) surface to ensure that the MGITC spectra resulted from molecules on the Au(111) substrate and not on the Au tip (Fig. 4.2e). Note that in our lab, the spectral signal-to-noise obtained under identical TER conditions shows a maximum variation of about 30%, independent of the user and chemical system under study, that can be mainly ascribed to variations in tip and focus qualities. To minimize the influence of underperforming tips and suboptimal focusing on the results presented in this study, we employ the same tip for all experiments of one type of molecule and compare and analyze spectra with best signal-to-noise ratios.

4.2.2 Discussion

Rather surprisingly, the normalized TERR scattering intensity in water is roughly double than the one in air. In principle, one would expect a signal reduction because of the beam aberrations at the air/glass and glass/water interfaces in the beam path between objective and tip apex that are present when working in the given side illumination geometry. Indeed, the tip-retracted far-field Raman signals are found to be reduced in water by factors between 3.3 and 4.9 compared to air due to the focus distortion (calculated for the four prominent bands at 801, 1175, 1584 and 1615 cm^{-1} as shown in Fig. 4.3).

This unexpected behavior can be explained by taking a closer look at the

tip-sample gap resulting from the chosen STM parameters for TERRS of MGITC/Au(111) in air (I_t = 0.1 nA, E_b=0.4 V) and in water (I_t=1.2 nA, E_b=0.04 V) which are known to affect TER spectral responses.[127]

The tunneling barrier in vacuum (and, at a first approximation, in air) can be described by Eq. 2.2 as explained in Chapter 2:[120,128]

$$\mathrm{I_t} \propto \mathrm{eE_b} \cdot \rho(\mathrm{E_F}) \cdot \mathrm{e}^{-\beta \cdot \mathrm{d}} \Rightarrow \mathrm{d} \propto \ln(\frac{\mathrm{E_b}}{\mathrm{I_t}}) \tag{4.1}$$

being the gap distance d, tunneling decay constant β, e the elementary charge and $\rho(\mathrm{E_F})$ the local density of states (LDOS) at the Fermi level.

Consequently, the tip-sample distance is directly proportional to $ln(\frac{E_b}{I_t})$ and therefore, in vacuum, for ϕ values of the most common metals, an increase in I_t (decrease in E_b) by a factor of 10 brings the tip a few Å closer to the sample.

Quantifying precisely the difference in the gap distance in air compared to the one in water is challenging since for the liquid experiment further parameters need to be taken into account: The tunneling barrier, ϕ, has been observed to be smaller in liquid due to tunneling processes via intermediate states.[129,130] For the system gold/water/gold, ϕ is expected to depend also on E_b.[131] Furthermore, for small gap distances as the ones we expect in water given the high set point and low bias, the $I_t/E_b(d)$ curve does not show an exponential behavior and new models need to be considered.[132,133] Thus, establishing ϕ for the liquid case is not straightforward. Nonetheless, to provide a crude approximation following the exponential model, a lower ϕ in water results in a larger gap distance, while higher I_t and lower E_b lead to a smaller tip-sample distance in water compared to air. Since the product I/E is 0.25 in air and 30.5 in water while ϕ values of Au are of comparable magnitude in air $\sqrt{\phi} \approx= \sqrt{4.8} = 2.1$ and in water $\sqrt{\phi} \approx \sqrt{1.8} = 1.34$,[131] we conclude that tunneling setpoint and bias voltage have a more significant effect on the gap size than the work function.

Qualitatively, from the given STM parameters, it is safe to deduce that the tip-sample distance is smaller for the in-water than for the in-air experiment. The TER(R) signal intensity is known to increase exponentially with decreasing tip-sample distance.[71,72,134–136] Thus, under the given experimental conditions in water with a comparatively smaller tip-sample distance, the sample produces stronger TERR signals than in air which can overcome the signal loss due to beam path aberrations. The observed shift of the TERR background maximum toward higher wavenumbers in water (788 $\mathrm{cm^{-1}}$, or 1.861 eV) compared to air (649 $\mathrm{cm^{-1}}$, or 1.878 eV), see Section A.1, is also in line with a smaller tip-sample gap in water[71,72], supporting our argumentation.

An overview of the discussed effects that the various experimental parameters

Experimental parameter	TER intensity	TER background maximum
↑ focus aberrations	↓	n.a.
↓ work function, ϕ	↓	blueshift
↑ tunneling setpoint, I_t	↑	redshift
↓ tip-sample bias, E_{bias}	↑	redshift

TABLE I. Effect of experimental parameters on TER scattering intensity and background maximum (gap plasmon resonance) location.

have on the TER scattering intensity and the location of the background maximum is given in Table I and can be summarized as follows: 1) Focus aberrations lead to a TER signal decrease while leaving the spectral background maximum (i.e. imprint of the gap plasmon resonance) unaffected. 2) A smaller work function (as is the case for water vs air environment) ends up in a larger tip-sample distance, which in turn results in a smaller TER signal and a blueshift of the background maximum (when keeping E_{bias} and I_t the same). 3) Regarding the STM parameters, an increase in I_t and a decrease in E_{bias} independently lead to a smaller tip-sample distance and thus to an increase in TER signal and a redshift of the spectral background maximum. Following Table I, our results show roughly twice the TERR scattering intensity from MGITC/Au(111) in water than in air. This effect can be explained if one considers the given experimental parameters (chosen such as to ensure optimally stable tunneling). A quantitative systematic investigation of the influence of the STM parameters on the TER response is extensively discussed in Chapter 5.

Note that, in principle, changing the gap medium from air to water could also strongly influence the Raman enhancement as the plasmon resonance frequency depends on the dielectric constant of the surrounding medium. However, calculations for a Au-water-Au system, essentially identical to the one presented here, show that 632.8 nm excitation produces comparable values for Raman enhancements in air and water, despite an overall redshift of the LSP resonance distribution.[107] Assuming the calculations hold for our system, we expect the effect of the different dielectric constants in air and water on the TERR signal intensity to be negligible.

Enhancement factors

Comparing the TERR/far-field intensity contrast and taking into account the respective scattering areas, we calculate Raman enhancement factors (EFs) for four bands that are distinguishable from the noise in the retracted spectra for

band	contrast air	EF air	contrast water	EF water
$801\,cm^{-1}$	9.9	$1.6{\cdot}10^4$	87	$1.9{\cdot}10^5$
$1175\,cm^{-1}$	11	$1.8{\cdot}10^4$	107	$2.4{\cdot}10^5$
$1364\,cm^{-1}$	9.5	$1.5{\cdot}10^4$	244	$5.4{\cdot}10^5$
$1615\,cm^{-1}$	11.6	$1.9{\cdot}10^4$	158.5	$3.5{\cdot}10^5$

TABLE II. TERR/far-field contrast and Raman enhancement factors(EF) for MGITC/Au(111) in air and in water.

both air and water according to the expression:[137]

$$EF = (\frac{I_{TERR} - I_{farfield}}{I_{farfield}})(\frac{V_{farfield}}{V_{TERR}}) \tag{4.2}$$

The first term in Eq. 4.2 (ratio between integrated intensities) is called contrast (factor). The scattering volumes of far-field and TERR can be approximated by areas for monolayer adsorbates, as is the case here, resulting in $\frac{A_{farfield}}{A_{TERR}} = (\frac{R_{farfield}}{R_{TERR}})^2$. We consider a far-field focus radius of 500 nm in air and 590 nm in water (measured from the CMOS images of the focus in air and water as explained in Chapter 3) and a tip radius of 25 nm (as deduced from SEM images of the tips, see Chapter 3). As described in Chapter 2, the TERR scattering radius is calculated as $\frac{1}{2}R_{tip}$.[95]

The calculated values of contrast and corresponding EFs are displayed in Table II. For the four peaks considered, the EFs in water range from $1.9{\cdot}10^5$ to $5.4{\cdot}10^5$ while the values in air lie between $1.5{\cdot}10^4$ to $1.9{\cdot}10^4$. The one order of magnitude difference in the EFs can be explained by taking into account the following considerations: 1) the increase of the TERR signal intensity, 2) the decrease of the far-field signal and 3) the increase of the area of the far-field focus in water with respect to air. These values are reasonable compared with previous reports in literature for similar systems (Au tip-Au substrate, STM-TERS), where values between 10^3 and 10^7 have been achieved in air for resonant molecules.[95]

To summarize this section, the presented solid/liquid TERS setup provides very good Raman enhancement and allows to collect excellent signal-to-noise TERR spectra from MGITC/Au(111) in water. The losses due to the distortion of the focus (as clearly observed in the far-field signal) can be overcome with STM-TERS by the choice of proper STM parameters which have a notable effect on the tip-sample distance and thus on the resulting TER(R) signal. In the remaining of the manuscript, we explore the possibilities of solid/liquid TERS for a more generic adsorbate case, namely, non-resonant PhS monolayer samples.

4.3 Non-resonant TERS: thiophenol

4.3.1 Results

Fig. 4.4 shows TER spectra of PhS/Au(111) in air (a: black) and in water (c: blue) as well as the corresponding far-field Raman spectra at 10 nm tip retraction (b: air; d: water). Excitation power and acquisition time were 260 µW and 5 s in air (840 µW and 10 s in water) for both TER and far-field experiments. Note that all shown spectra are normalized to 260 µW and 5 s integration time and the water results are multiplied by a factor of 20 for clarity.

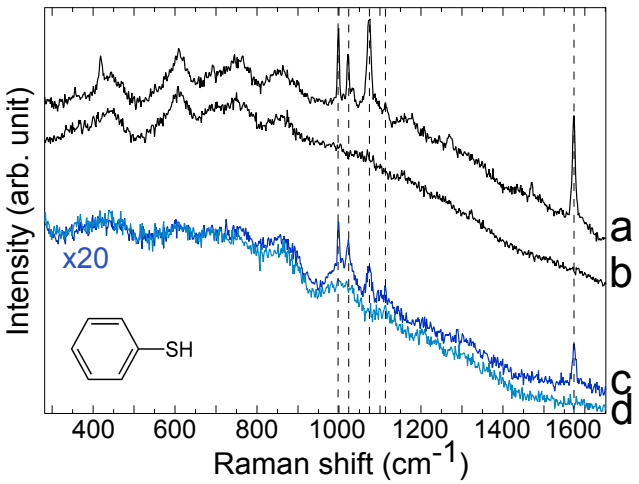

FIGURE 4.4. Raman spectra of PhS/Au(111) in air (a,b) and in MilliQ (c,d). a: TER in air (E_{bias}=0.1 V, I_t=0.1 nA); b: far-field Raman with 10 nm tip retraction in air; c: TER in water (E_{bias}=0.1 V, I_t=1 nA); d: far-field Raman with 10 nm tip retraction in water. All spectra are normalized to 260 µW power and 5 s acquisition time (water spectrum: x20) and y-offset for clarity. Inset: PhS. Reproduced with permission from *Analytical Chemistry, 88*, 7108-7114 (2016); Copyright 2016 American Chemical Society. [1]

Both air and water TER spectra allow unambiguous identification of PhS: For TER scattering in water, the aromatic ring vibrations at 998, 1022, 1073 and 1573 cm^{-1} and a weaker band at 1113 cm^{-1} are observed which are the typically employed marker bands of PhS [124]. In the air spectra, additional bands appear at 418, 691 and 1469 cm^{-1} (see Table III).

Contrary to the case of MGITC, the detection of a monolayer PhS/Au(111) in the far-field is not possible because of the smaller scattering cross-sections and lack of electronic resonance enhancement. Note that the undulated back-

Position (Blum 2013)	Position air (cm^-1)	Position water (cm^-1)	Assignment
417	418	-	$\nu_{CS} + \nu_{AuS}$
692	691	-	$\delta_{CCC} + r - i - d$
999	998	998	$r - i - d + \nu_{CC}$
1022	1022	1022	$\nu_{CC} + \delta_{CH}$
1074	1073	1074	$\nu_{CC} + \delta_{CH}$
	1114	1113	
1473	1469	-	$\delta_{CH} + \nu_{CC}$
1581	1573	1573	ν_{CC}

TABLE III. Band assignment of PhS based on Refs. 124,138,139. r-i-d: ring in plane deformation; ν: stretching; δ: bending

ground is instrument-induced by beam interference on the dichroic filter. Similar background undulations are observed also for MGITC/Au(111) (Fig. A.1), despite less obvious due to the much stronger resonant signal. STM images of PhS/Au(111) in air and in water reveal flat terraces and monoatomic steps similar to the ones observed for MGITC.

4.3.2 Discussion

We evaluated the setup performance by comparison of air and water TER experiments following the analysis reported in the interlaboratory TERS study on PhS/Au(111) in air. The mentioned study aimed at exploring the reproducibility of TERS results of different setups and experimental configurations of experienced TERS groups by Blum *et. al.* and constitutes an important step to establish a standard quality check of results produced by new instruments. [124]

We fitted the five strong modes (vertical dashed lines in Fig. 4.4) with Lorentzian functions to extract relative peak positions and intensities. An overview of the results for peaks 998 (P1), 1022 (P2) and 1073 cm^{-1} (P3) is presented in Tables III and IV.

The reported peak positions, the results both in air and in water show perfect consistency with previous studies [124]. The relative band intensity P3/P1 in air is 1.21 compared to 1.35±0.31 reported, indicating excellent performance of the setup in air. While the P2/P1 ratio does not change much switching from air (0.65) to water (0.71), the intensity of P3 is lowered in the liquid experiment, resulting in relative intensity factors of 0.52 for P3/P1 and 0.73 for P3/P2, a factor 2.4 lower than the ones found in air. In Ref. 124, an average value of 1.35 ratio P3/P1 is given for the entire study; however, the average values from

intensity ratio	air	water	air [124]
P3/P1	1.21	0.52	1.35±0.31
P3/P2	1.85	0.73	-
P2/P1	0.65	0.71	-

TABLE IV. Relative peak intensities for three PhS marker bands P1: 998 cm^{-1}, P2: 1022 cm^{-1}, P3: 1073 m^{-1} for TERS in air and in water. Literature values from Ref. 124 are listed for comparison.

individual setups range from 0.83 to 1.66, and individual spectra averages on different setups lie between 0.61 and 2.25. While our in-air and in-water results are thus both comparable to values reported in Ref. 124, the origin of the large variance of P3 intensity between individual measurements remains unclear.

For PhS/Au(111), the overall TER scattering intensity in water is reduced by a factor of ca. 20 and the background maximum is blueshifted compared to air. These results can be discussed and explained qualitatively by the chosen experimental parameters, following the overview given in Table I. An intensity decrease is expected when switching from air to water because of the focus point aberrations. Regarding the STM parameters in the PhS experiments (again chosen to give the most stable STM tunneling), the STM set-point was 0.1 nA in air and 1 nA in water, and the bias voltage was 0.1 V both in air and in water. In the case of MGITC the larger intensity in the liquid experiments is attributed to the large difference in set-point and bias that can overcome the reduction of the work function in the liquid environment. In contrast, in the case of PhS, the variation in I_t is smaller and E_b was kept constant. Thus changes in ϕ are expected to play a more dominant role. As a result, for the PhS experiments, the tip-sample distance is expected to be larger in water compared to air which is consistent with the observed TER signal intensity drop.

Moreover, the difference in the position of the Lorentzian-shaped background maximum (Fig. A.2 and Table I) supports this conclusion: the maximum of the more intense TER spectrum in air appears at higher wavenumbers than the water maximum (690 cm^{-1}, or 1.87 eV, in air versus 511 cm^{-1}, or 1.90 eV, in water). This blue shift of the TER background indicates a larger tip-sample gap in water resulting in lower TER enhancements. [71,72]

4.4 Conclusions

The system's performance was benchmarked by measuring monolayer adsorbates of both resonant MGITC dye and non-resonant PhS on optically non-

transparent Au(111) single crystals in water. We observed that beam aberrations due to the presence of the liquid phase reduce the (conventional) far-field response by a factor three, as expected due to severe far-field focus distortions. Interestingly, these distortions were found to play only a minor role for near-field Raman measurements. Our setup design allowed us to obtain excellent signal-to-noise ratios in the TER responses from both resonant and non-resonant molecules, with Raman enhancement factors in the order of 10^5. Furthermore, we noticed that the chosen STM parameters have a significant influence on the TER signal intensity as sample bias and tunneling current directly affect the tip-sample distance and thus the field (and Raman) enhancement.

In order to understand better the effect of the STM parameters on the TERS signal and how they can be used to maximize signals in air an liquid, we perform a series of experiments to systematically vary E_b or I_t while monitoring the TERS response. The experiments and results obtained are described in Chapter 5.

Chapter 5

The effect of STM parameters on the TERS signal

In the previous chapter, higher intensity in liquid spectra than in air was found for MGITC, in spite of the expected decrease in liquid due to focus aberrations. This observation is initially attributed to a tip-sample distance change due to the tunning of the STM parameters. In order to verify and understand this hypothesis, new experiments evaluating the effect of tunneling current, I_t, and bias voltage, E_b, on the TERS signal are performed and detailed in this chapter. More concretely, the dependence of TER spectra of a monolayer of thiophenol at a Au(111) electrode on the STM parameters I_t and E_b is systematically evaluated, comparing experiments in inert gas (Ar) and in water. We analyse the trends of intensity changes when varying I_t and/or E_b. A theoretical model of these effects allows us to predict optimal STM parameters in TERS experiments to exploit maximum signal enhancement and thus experiment sensitivity.

The content of this chapter has been published previously in Ref.[3]. Text and figures are reproduced with permission from *Faraday discussions, 205*, 233-243 (2017); `http://pubs.rsc.org/en/content/articlelanding/2017/fd/c7fd00164a#!divAbstract`, published by the Royal Society of Chemistry. [3] [a]

[a] the reader is referred to the Royal Society of Chemistry for further permissions regarding these materials

5.1 Introduction

The unexpected high intensity recorded in the initial liquid TERRS experiments of resonant molecules reported in Chapter 4 was qualitatively attributed to a change in gap distance in air versus water due to the settings of the STM (E_b and I_t) applied in each environment. While logical, this hypothesis was not evaluated experimentally. In this chapter, we perform a series of experiments to explore the effect of tuning these parameters on the TER spectra. Since the extremely high intensities detected in liquid were attributed to this effect, a further understanding can be efficiently used to improve TERS enhancement.

As detailed in Chapter 2, maximizing the enhancement in a TERS experiment is possible by minimizing the gap distance between tip and sample.[69–72,136] The TERS intensity, I_{TERS}, is inversely proportional to the 8th to the 10th power of the tip-sample separation following Eq. 2.10:[70,71]

$$I_{TERS}^{norm} \approx \left(1 + \frac{d}{\rho}\right)^{-p} \tag{5.1}$$

with d the gap distance, ρ the dipole radius (approximately the tip radius) and p = 10 for fully incoherent scattering.

Additionally, in STM the gap distance depends on the tunneling parameters, I_t and E_b. Electron transport between electrodes separated by a thin insulating film in the low bias range is described by Eq. 5.2:[53,54,57,140]

$$I_t = \frac{E_b}{R(z_0)} \cdot e^{-\beta \cdot d} \Rightarrow d = \frac{1}{\beta} \ln\left(\frac{E_b}{I_t \cdot R(z_0)}\right) \tag{5.2}$$

where $R(z_0)$ is the junction resistance at the landing position, z_0, and β is the tunneling decay constant, $\beta = \frac{4\pi}{h}\sqrt{2m\phi}$, with ϕ the work function or barrier height, m the electron mass and h Planck's constant. According to equation Eq. 5.2, the tip approaches the sample with increasing I_t or decreasing E_b. Combining eqs. (5.1) and (5.2), we derive an expression relating the TERS intensity to the gap distance in constant current mode experiments:

$$I_{TERS}^{norm} \approx \left[1 + \frac{1}{\rho\beta}[\ln(E_b) - \ln(I_t) - \ln(R(z_0))]\right]^{-10} \tag{5.3}$$

Equation (5.3) predicts the behavior of the TER signal intensity as a function of gap size as determined by the STM parameters. Despite its potential impact on increasing TERS sensitivity, only a few studies have reported how TER spectra vary with chosen I_t and E_b[1,27,127,140] and a systematic study for both

I_t and E_b under identical conditions (same tip, same sample) is still lacking. In general, the expected trends were observed in individual studies, i.e. an increasing I_t results in a rise of peak and background intensities as expected from the corresponding gap distance decrease,[27] and a similar effect has been observed upon decreasing the bias voltage.[127] For a monolayer of azobenzene, an unexpected deviation from the STM-parameter dependent distance relation was observed where I_{TERS} decreased with increasing bias voltages faster than would be expected from a mere gap size increase.[140] The quantitative discrepancies between model and experiment were suggested to arise from molecular bending induced by the local electric field in the tunneling region created by E_b. Hence, the relation between E_b and I_{TERS} was suggested to be a convolution of different effects including gap distance and related variation of the near-field enhancement magnitude and molecular reordering.

Here, we perform experiments with the same tip and sample tuning systematically E_b (I_t) while keeping I_t (E_b) constant and evaluate the effect of these changes in the spectral response of PhS. We find an increase of TER intensity upon set-point increase or bias decrease as expected from a gap-distance reduction. The relations obtained follow the theoretical model considering a simple gap-distance change when tuning the mentioned parameters.

5.2 Materials and methods

Sample preparation

Ethanol (purity 99.9%) and thiophenol from Sigma-Aldrich and MilliQ were used in the experiments. The annealed substrate was immersed into 1 mM ethanolic PhS solution for 8 hours and rinsed extensively afterward to remove adsorbate multilayers. The sample was mounted immediately after preparation. A gentle flow of Ar (5N, Westfalen) was poured over the sample during the experiment (except during spectral acquisition) to prevent contamination.

Experimental procedure and analysis

Ar and water experiments were performed on different days and with several different tips following the same procedure and preparation. For each experiment, different series of I_t (E_b) ramps at constant E_b (I_t) were taken.

Tuning E_b in our STM is achieved by grounding the tip and ramping the sample potential. Due to technical constraints, tuning the bias voltage by changing the potential of the tip while keeping the sample potential constant is only possible in electrochemical mode.

Each experimental series consists of TER spectra taken at different values of

I_t (or E_b) cycled at least once from high to low values and vice-versa. I_t was ramped between 0.1 and 1.8 nA with constant E_b of 0.02 V, 0.04 V and 0.1 V. E_b was ramped between 0.02 and 0.5 V at constant I_t of 1.3, 0.8 and 0.3 nA. For each combination of values, 5 consecutive spectra were taken and the average used for fitting purposes. STM parameters were ramped in tunneling conditions, and all spectra in one series were taken at the same location on a flat terrace of the Au(111) substrate as determined by STM topographic imaging prior to the experiment, and with the same far-field focusing conditions. The far-field spectra (acquired by retracting the tip 20 nm from the tunneling position) were taken several times during a series by disabling the feedback mechanism of the STM (no motor retraction) to prove cleanliness and stability of the tip during the hour-long experiments.

The same band fitting (masks, background, and constraints) was performed on all spectra of different series and days using IgorPRO (wavemetrics). Unless stated differently, the results presented in the figures correspond to averages of spectra taken with the same tip under the same conditions (of E_b and I_t) during scans up and down, and the errors correspond to the statistical standard deviation. Spectra were acquired with integration times of 5 seconds in Ar and of 30 seconds in water with 600 μW excitation power at the exit of the objective. In the figures, they are presented normalized to the same time and power. Note that signal losses are expected when working in liquid due to beam aberrations and far-field focus distortion as discussed in previous chapters. [1,113]

5.3 Results

The system under study in this work is a monolayer of thiophenol (PhS, inset Fig. 5.1) adsorbed at a Au(111) single crystal. This sample was chosen because of the strong chemisorption of PhS at Au through the S atom, providing stability of the monolayer and a strong and reproducible TER signal suitable to perform hour-long experiments where many combinations of STM parameters can be explored with the same tip. Additionally, the extensive TERS literature of PhS/Au(111) facilitates band assignment and comparison with previous results. [1,31,124] Note that MGITC, the resonant adsorbate used in Chapter 4 degrades easily with increasing laser power and exposure time. [105,141] Therefore it is not a good reference sample for the present experiments since collecting spectra for all combinations I_t /E_b in the same sample and with the same tip takes long time which makes convenient the choice of a more stable adsorbate.

Fig. 5.1 shows examples of raw TER spectra acquired during series of A) varying I_t at constant E_b =0.04 V and B) varying E_b at constant I_t =1.3 nA in Ar (green) and in water (blue). The most prominent bands of PhS are visible with high

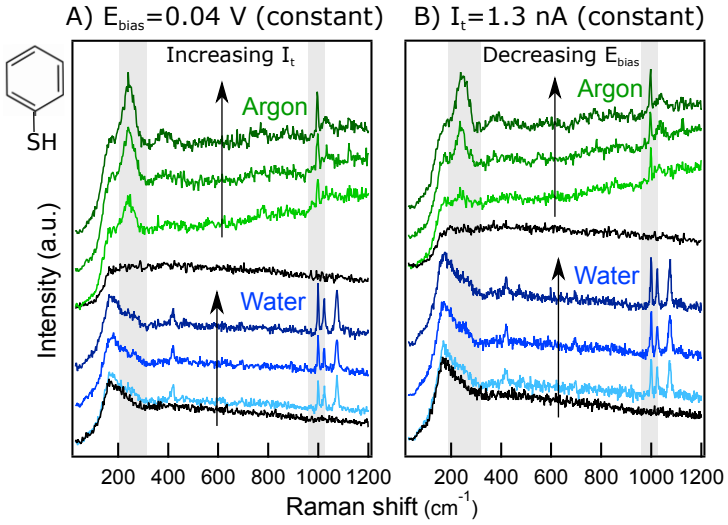

FIGURE 5.1. Raw spectra recorded in Ar (green) and in water (blue) for A: I_t ramp at constant E_b of 0.04 V, B: E_b ramp at constant I_t of 1.3 nA. For each series, 20 nm retraction spectra (far-field) are included in black. Gray rectangles indicate marker bands. Spectra are y-offset for clarity. Inset: PhS chemical structure. Reproduced with permission from *Faraday discussions, 205*, 233-243 (2017); published by the Royal Society of Chemistry. [3]

signal-to-noise ratio (S/N) in all spectra and are in agreement with previous TERS reports for PhS/Au(111). [1,31,124]

All spectra exhibit two prominent bands at ca. 245 (δ_{CS}+ν_{AuS}) and at 997 cm^{-1} (r-i-d +ν_{CC}). In Ar, the spectra show also two weak, broad bands at ca. 390 (γ_{CH}) and at 1024 cm^{-1} ($\nu_{CC} + \delta_{CH}$). [142] The liquid spectra features a broad far-field band at low wavenumbers (see retracted spectra, black), partially masking the 245 cm^{-1} Au-S band that here is visible only as a shoulder. This far-field peak is present in all liquid and electrochemical spectra acquired in our lab [1] and can be attributed to the aqueous work environment. Details of the fitting of Raman bands partially masked by this broad feature in liquid is reported in Section A.2. In the water spectra, the peak at 1024 ($\nu_{CC} + \delta_{CH}$) is more prominent than in Ar, and an extra mode at 1074 cm^{-1} ($\nu_{CC} + \delta_{CH}$) shows up. The weak broad band at 390 cm^{-1} is not present in the liquid spectra, but an additional sharp peak appears at ca. 420 cm^{-1} ($\nu_{CS} + \nu_{AuS}$). [b]

[b] In the literature, different TER spectral signatures for PhS/Au have been reported whose chemical origin has remained unclear. [124] Within our lab, we also detect day-to-day variations of the spectral signature of PhS mainly in relative intensities, as obvious when comparing the TERS results of PhS presented in the previous and the present Chapters. As discussed in the previous chapter, these changes might be attributed to variations in the tip geometry or sample preparation and therefore, the more accurate way to proceed is to compare, as far as

Here, we focus the discussion on the relative intensity changes of the Au-S mode at 245 cm^{-1} and the ring-in-plane deformation mode at 997 cm^{-1} that are present both in liquid and in Ar spectra and are therefore ideal for singling out the influence of STM parameters in different environments. Additionally, given the technical specifications of our instrument, the mode at 245 cm^{-1} can be used as direct reporter on the effect of the sample potential on the adsorbate-substrate interaction.

Fig. 5.1A includes three example spectra at increasing I_t (from bottom to top) in Ar and in water each. Increasing the tunneling current set-point results in an increase of the marker bands for both Ar and water experiments. Similarly, ramping the bias voltage to lower values increases the intensity of the marker bands (Fig. 5.1B). These trends are in qualitative agreement with the expected decrease of the gap distance upon I_t increase or E_b decrease as deduced from Eq. 5.2. To gain quantitative insight into this relation, Lorentzian band fittings have been performed for the different series and are discussed in the rest of the chapter.

5.4 Discussion: fitting results

In Fig. 5.2 we present the integrated intensity of the 245 cm^{-1} (A) and 997 cm^{-1} (B) bands as a function of I_t for constant values of bias voltage in Ar (0.02 V green, 0.04 V dark blue, 0.1 V purple) and water (0.04 V, light blue) and the integrated intensity of the 245 cm^{-1} (C) and 997 cm^{-1} (D) bands as a function of E_b for constant values of tunelling current in Ar (0.3 nA orange, 0.8 nA red, 1.3 nA black) and water (1.3 nA, light blue). All Ar results presented in this figure were acquired on the same day and with the same tip at different locations of a flat Au(111) terrace while the liquid results were taken on a different day with a different tip.

5.4.1 Influence of the tunneling current in the TERS response

We find that the I_{TERS} increases upon current increase as expected from a gap distance reduction, eqs. (5.1) to (5.3). In Ar, the absolute TERS intensity of the 245 cm^{-1} peak increases linearly with I_t, while in water the intensity remains almost unchanged (Fig. 5.2 A). The slopes obtained by linear fits, indicating

possible, spectra acquired in the same conditions (tip, sample). The TERS community is at the moment making efforts to develop reference samples for TERS instruments in order to establish standards for the reproducibility of the technique.

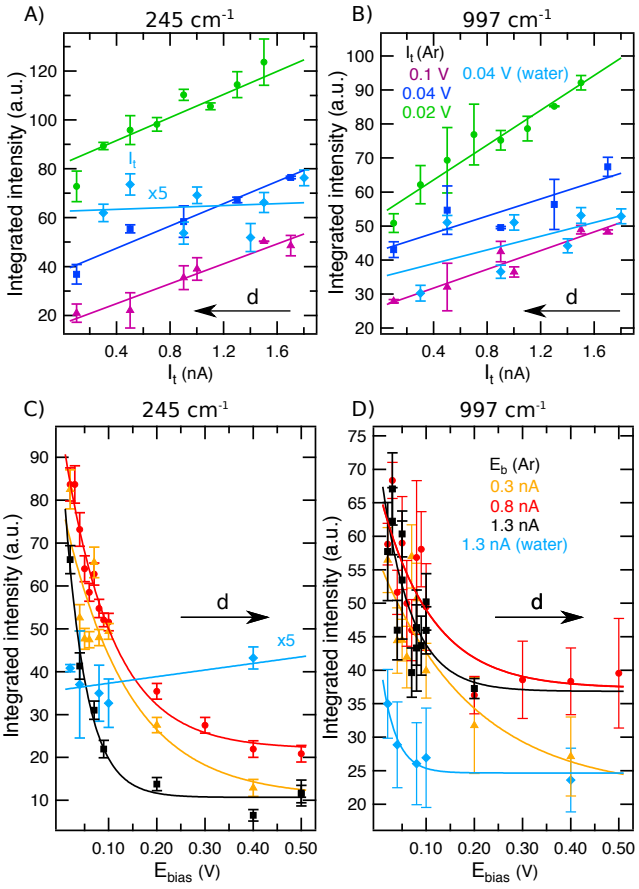

FIGURE 5.2. A: Integrated intensity of the 245 cm^{-1} mode (B: 997 cm^{-1}) as a function of I_t at constant E_b values of 0.02 V (green), 0.04 V (dark blue), 0.1 V (purple) in Ar and 0.04 V in water (light blue). C: Integrated intensity of the 245 cm^{-1} mode (D: 997 cm^{-1}) as a function of E_b at constant I_t values of 0.3 nA (orange), 0.8 nA (red), 1.3 nA (black) in Ar and 1.3 nA in water (light blue). Normalized to the same power and integration time. Averaged results from spectra taken in scans up and down are presented with standard deviation as error. Solid lines represent linear fittings (A and B) and exponential fittings (C and D) of the experimental data points. Reproduced with permission from *Faraday discussions, 205*, 233-243 (2017); published by the Royal Society of Chemistry. [3]

the rate of growth, are 20±3, 23±3 and 31±4 counts/nA at 0.1, 0.04 and 0.02 V respectively in Ar, and 0.4±2 at 0.04 V in water. This band is covered in liquid by a far-field feature that hinders the fitting procedure, being a possible cause for the large difference in trend (note that the liquid results in Fig. 5.2 A are multiplied by a factor of 5 to facilitate the comparison, much weaker intensities were detected in liquid). The total intensity increase of the 245 cm^{-1} peak in the current range scanned is 70%, 107% and 131% in Ar at 0.02 V, 0.04 V and 0.1 V, respectively, and only 23% in water.

The 997 cm^{-1} peak (Fig. 5.2B) increases linearly with I_t in Ar and water with slopes of 14±3, 13±4 and 26±3 counts/nA at 0.1, 0.04 and 0.02 V, respectively, in Ar, and 10±6 at 0.04 V in water. The slower growth of this peak with current leads to slightly lower absolute intensity gains: 81%, 57% and 73% in Ar at 0.02 V, 0.04 V and 0.1 V respectively and 76% in water. These results are summarized in Table I

E_b/V	slope/counts·nA^{-1}		Increase I_{TERS}/%	
	245 cm^{-1}	997 cm^{-1}	245 cm^{-1}	997 cm^{-1}
0.1	20 ± 3	14 ± 3	131	73
0.04	23 ± 3	13 ± 4	107	57
0.02	31 ± 4	26 ± 3	70	81
0.04 (water)	0.4 ± 2	10 ± 6	23	76

TABLE I. Results of linear fittings to the I_{TERS} vs I_t data points of Fig. 5.2A and B

The constant value of E_b applied while varying the current has an influence on the absolute TERS intensity. For higher voltages (0.1 V, purple) the overall intensity detected is smaller than for lower values (0.02 V, green) in agreement with the relative larger tip-sample gap at high E_b. Additionally, the rate of growth of both bands (slopes in the fittings) is higher at 0.02 V, by 31% (245 cm^{-1}) and 50% (997 cm^{-1}).

When comparing the two peaks analysed, we observe that the slopes and percentage of signal gain are higher for the Au-S mode, that is thus more affected by the current ramp. Note that this hypothesis does not hold in the case of liquid experiments where a slope close to zero is obtained for the 245 cm^{-1} peak. The results of the 997 cm^{-1} peak show a very similar trend between Ar and water results. This mode is more intense in the liquid spectra where the low wavenumber region is affected by a broad far-field contribution (Fig. 5.1). In view of this, we assume that the intensity results of the 245 cm^{-1} mode in water are possibly affected by the fitting procedure and conclude that the effect of ramping I_t in the TERS intensity is similar in Ar and water, with average values of intensity gain (taking into account both bands and different values

of E_b applied) of 87% in Ar and 76% in water (discarding in water the results obtained from the 245 cm^{-1} band).

Therefore in a TERS experiment, higher values of tunneling current are preferred if the maximum enhancement is sought both in Ar and liquid experiments. Tuning the current to large values (larger than 1 nA) decreases the gap distance and achieves very high intensities without inducing any obvious chemical change that might further alter the signal intensity or band position (as will be discussed in Section 5.6) while the tip-sample separation is still large enough to prevent tip crash or contamination.

5.4.2 Influence of the bias voltage on the TERS response

Decreasing E_b reduces the tip-sample gap size and therefore results in an increase of I_{TERS}, eqs. (5.1) to (5.3), as observed in Fig. 5.2C and D. From the figure, it is apparent that the choice of I_t has a negligible effect on the TERS intensity over the investigated E_b range, in contrast to ramping I_t where I_{TERS} was higher for lower E_b values. The orange, red and black curves in Fig. 5.2D for the 997 cm^{-1} (taken at 0.3, 0.8 and 1.3 nA, respectively) overlap. For the 245 cm^{-1} peak, the overall intensity at 1.3 nA is lower than the intensity at 0.3 nA and 0.8 nA.

The integrated intensity as a function of E_b shown in Fig. 5.2 C and D shows very different behavior than the results obtained when ramping I_t. It is obvious from the figures that the trend of I_{TERS} upon bias increase deviates from the linearity obtained when tuning the tunneling current (Fig. 5.2 A and B). In Ar, the intensity decrease of the 245 cm^{-1} peak can be modeled with an exponential decay function for all values of constant I_t. In contrast, the water results show an initial decrease in the range 0.02-0.1 V and the band intensity grows again at 0.5 V. As discussed, the fitting of this band is not straightforward due to a broad far-field feature in the low-wavenumber region, and therefore the results are not as reliable as for the 997 cm^{-1} mode. The band intensity of the 997 peak shows an exponential dependence with E_b in Ar and liquid experiments.

When decreasing the bias, the absolute intensity of the 245 cm^{-1} is increased by 478%, 300% and 539% at I_t values of 1.3, 0.8 and 0.3 nA, respectively in Ar and 28% in liquid. I_{ters} of the 997 cm^{-1} mode shows a weaker dependence on E_b. The absolute intensity of this mode rises by 80%, 73% and 108% at I_t values of 1.3, 0.8 and 0.3 nA in Ar, respectively and 47% in water at 1.3 nA. The results are summarized in Table II

In average (considering both bands and the different values of constant I_t applied), the intensity increase achieved during bias ramp is 263% in Ar and 47%

I_t/nA	Increase I_{TERS}/%	
	245 cm^{-1}	997 cm^{-1}
0.3	539	108
0.8	300	73
1.3	478	80
1.3 (water)	28*	47

TABLE II. Absolute intensity increase of the Raman bands obtained when decreasing the bias value from 0.5 V up to 0.02 V. *Note that this value is calculated considering the initial decrease from 0.02 V to 0.1 V.

in liquid, in contrast with the values of 87% in Ar and 76% in water obtained in the variable current series presented in previous section. In view of these results, it seems obvious that the value of E_b applied in a TERS experiment is much more likely to influence the near-field enhancement and thus the intensity detected than the tuneling current in the ranges explored in these experiments.

When searching for the highest sensitivity in a TERS experiment, higher values of I_t (higher than 1 nA) and lower values of E_b (under 0.1 V) are preferred being E_b the more critical parameter compared to I_t regarding TER signal intensity. Interestingly, we find that the described effect on I_{TERS} is lower in water than it is in Ar for the given parameter space. Further investigations exploring the ranges of $I_t > 1.7$ nA and $E_b < 0.02$ V in water could provide more insight on this observation. In general, this first systematic qualitative evaluation allows us to quantitatively correlate the effect of both I_t and E_b on I_{TERS}.

5.5 Distance dependence model

Up to now, a general description of the data was provided where, in the range scanned, E_b seems to influence the TERS response more than I_t. In the following paragraphs, the discussion is focused on relating the data obtained with the simple mathematical model of Eq. 5.3.

Fig. 5.3 shows the integrated intensity of the 245 cm^{-1} (A) and 997 cm^{-1} (B) bands as a function of $Ln(I_t)$ for constant E_b in Ar (0.02 V green circles, 0.04 V dark blue squares, 0.1 V purple triangles) and in water (0.04 V light blue diamonds). Note that these are the same results as in Fig. 5.2 A and B but in logarithmic scale; in linear scale, I_{TERS} as a function of I_t shows a linear increase upon current increase. A logarithmic x-axis scale has been chosen in this case based on the gap-distance dependence on I_t and E_b according to Eq. 5.3. Similarly, Fig. 5.4 displays the integrated intensity of the 245 cm^{-1} (A) and

997 cm^{-1} (B) bands as a function of Ln(E_b) for constant values of tunneling current set-point in Ar (0.3 nA orange triangles, 0.8 nA red circles, 1.3 nA black squares) and water (1.3 nA light blue diamonds).

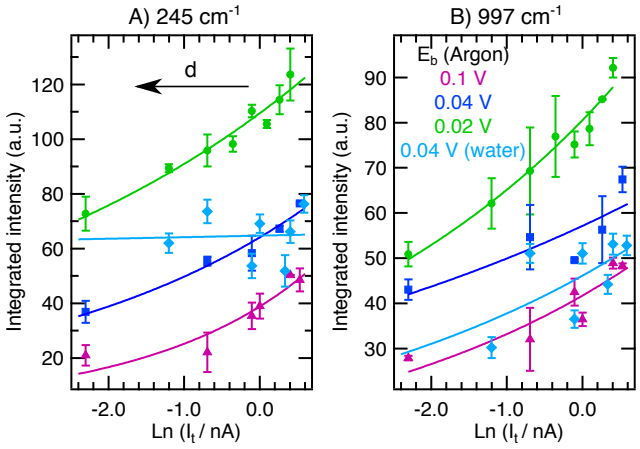

FIGURE 5.3. A: Integrated intensity of the 245 cm^{-1} mode (B: 997 cm^{-1}) as a function of Ln(I_t) at constant E_b values of 0.02 V (green circles), 0.04 V (dark blue squares), 0.1 V (purple triangles) in Ar and 0.04 V in water (light blue diamonds). Averaged results from spectra taken in scans up and down are presented with standard deviation as error. Fittings to Eq. 5.3 are included (solid lines). Reproduced with permission from *Faraday discussions, 205*, 233-243 (2017); published by the Royal Society of Chemistry. [3]

To evaluate if the dependence of the TER signal intensity on tunneling current set-point and bias voltage follows a simple distance dependence in the case of PhS/Au(111), we fitted the experimental data from Figs. 5.3 and 5.4 with Eq. 5.3 (solid lines in figures) in a free fitting, obtaining ρ, β and R(z_0) for each of the series. The averaged fitting results are summarized in Table III for the current set-point and bias voltage ramps, for different bands and different values of I_t or E_b from two different experiments in Ar (with different tips) and one in water. All fittings were performed with the same initial guesses of the fitting parameters (ρ=15 nm, β=0.3 $Å^{-1}$ and R(z_0)=50 MΩ). As obvious, the fitting function describes accurately the experimental data in all cases.

The obtained values for the tip radius (i.e. dipole radius ρ) from different days (including air and water results), in average 17 ± 3 nm are in agreement with the average tip sizes produced in our lab as estimated from SEM images included in Section 3.4. [1]

The fitting procedure returned values of β of 0.32 and 0.33 $Å^{-1}$ in air and in water, respectively. The tunneling decay constant, β, has been measured experimentally for a number of similar molecules in previous works. Frisbie *et*

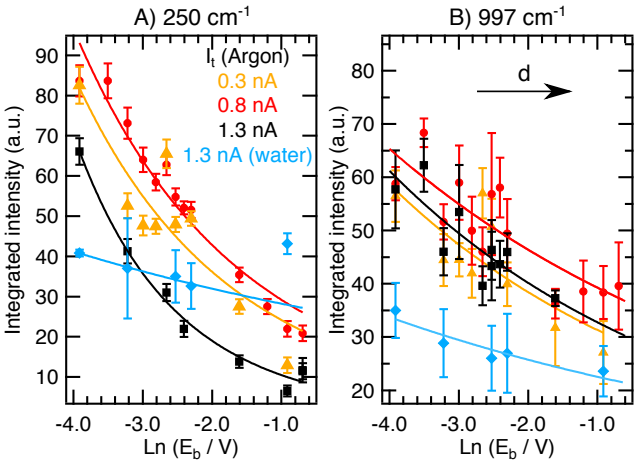

FIGURE 5.4. A: Integrated intensity of the 245 cm^{-1} mode (B: 997 cm^{-1}) as a function of E_b at constant I_t values of 0.3 nA (orange triangles), 0.8 nA (red circles), 1.3 nA (black squares) in Ar and 1.3 nA in water (light blue diamonds). Averaged results from spectra taken in scans up and down are presented with standard deviation as error. Fittings to Eq. 5.3 are included (solid lines). Reproduced with permission from *Faraday discussions, 205*, 233-243 (2017); published by the Royal Society of Chemistry. [3]

al. [143] found an average β=0.4 $Å^{-1}$ for alkanethiols of different lengths, with a tip-to-tip variation in the same range as we find for different days. In [140], β=0.27 $Å^{-1}$ was reported for an azobenzene monolayer on Au(111). Electrochemical experiments of similar aromatic molecules give values of β between 0.35 and 0.57 $Å^{-1}$. [144,145] Our β values lie well within the reported variability. The small discrepancies between the above mentioned reported values can be due to differences in chemical structure, orientation or packing of the monolayer that directly affect the electron transport in the junction. [140,146,147] Interestingly, the obtained decay constant values in Ar and in water experiments are very similar, despite the smaller values of the work function that are expected in liquid. [129–131]

The values for the junction resistance at landing position obtained from the fittings are 30 and 16 MΩ for air and liquid, respectively. Contact resistance $R(-z_0)$[c] literature values between 0.1 and 50 MΩ have been found for similar molecules, among which ≈0.1 MΩ for the PhS/Au(111) system. [143,148] Higher values are expected for $R(z_0)$ since here molecular length and gap distance are also considered. Toccafondi *et al.* [140] recently reported $R(z_0)$ to be 694 MΩ for azobenzene /Au(111) in a E_b-dependence TERS study. Compared to the

[c] While $R(-z_0)$ accounts for the resistance of the junction in contact between tip and sample, the parameter in Eq. 5.3, $R(z_0)$, is the junction resistance at landing position.

	ρ / nm	β / Å^{-1}	R(z_0) / MΩ
Ar (day 1)	14 ± 3	0.27 ± 0.07	34.5 ± 20
Ar (day 2)	17 ± 6	0.36 ± 0.12	24.5 ± 10
Ar (average)	16 ± 2	0.32 ± 0.05	30 ± 7
Water	20 ± 2	0.33 ± 0.04	16 ± 4

TABLE III. Averaged fitting parameters for the data points in Figs. 5.3 and 5.4. ρ dipole radius; decay constant $\beta = \frac{4\pi}{h}\sqrt{2m\phi}$ and R(z_0) tunneling resistance at landing position.

literature values, the experimental values of 30 and 16 MΩ that we obtain in Ar and in water, respectively, lie well within the expected range, considering that PhS is shorter than azobenzene. Furthermore, a lower resistance in water is in agreement with a better electric conductivity of MilliQ (resistivity of ca. 18 MΩ) compared to Ar.

In summary, the fittings quantitatively describe our experimental data points. Additionally, the values of the fitting parameters obtained are in agreement with literature values for both Ar and water for current set-point and voltage ramps. Therefore it can be concluded that the TER signal intensity follows the expected distance-dependent relationship of Eq. 5.3 for both in-Ar and in-water I_t and E_b ramps. Additional geometric effects such as molecular bending that has been reported for longer molecules [140] do not need to be taken into account in the case of PhS/Au(111).

5.6 Effect of STM parameters on the Raman frequencies

In Fig. 5.5 we present the Raman shift of the 245 cm^{-1} as a function of I_t (A) for constant values of bias voltage in Ar (0.02 V green, 0.04 V dark blue, 0.1 V purple) and water (0.04 V, light blue), and as a function of E_b (B) for constant values of tunelling current in Ar (0.3 nA orange, 0.8 nA red, 1.3 nA black) and water (1.3 nA, light blue). C and D show the equivalent shifts for the 997 cm^{-1} peak.

From the figure, it is obvious that, in addition to changes in I_{TERS}, we also observe a shift of the 245 cm^{-1} band as a function of E_b. In the series of measurements at constant E_b and variable I_t shown in Fig. 5.5A, the 245 cm^{-1} mode appears at a constant position throughout the scanned set-point range. However, the peak maximum is shifted to lower wavenumbers upon E_b increase. This effect is obvious in the series of measurements at constant I_t and variable

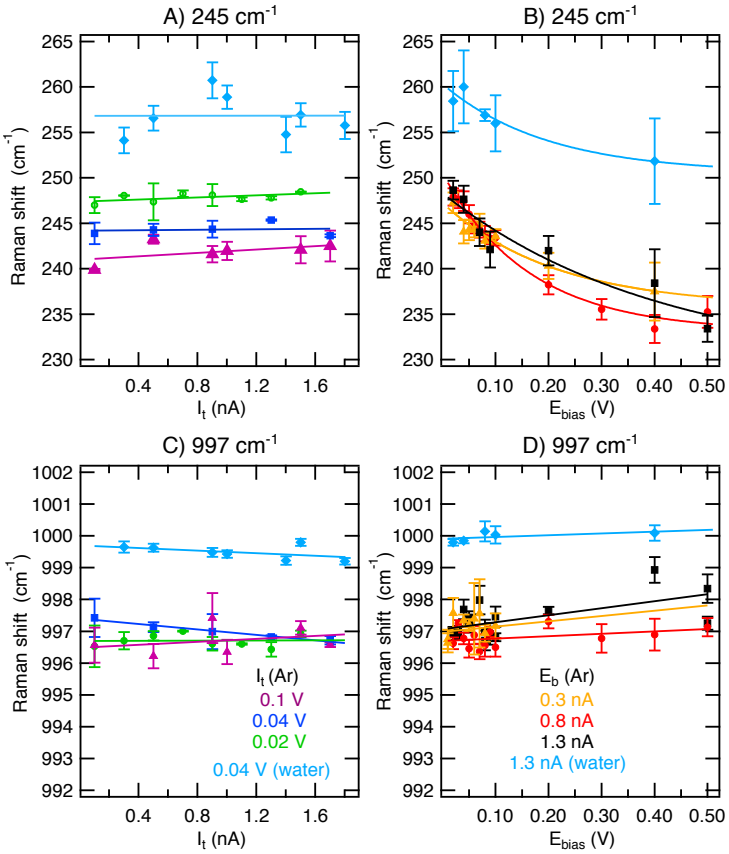

FIGURE 5.5. Raman shift of the 245 cm^{-1} as a function of I_t (A) for constant values of bias voltage in Ar (0.02 V green, 0.04 V dark blue, 0.1 V purple) and water (0.04 V, light blue), and as a function of E_b (B) for constant values of tunelling current in Ar (0.3 nA orange, 0.8 nA red, 1.3 nA black) and water (1.3 nA, light blue). C and D show the equivalent shifts for the 997 cm^{-1} band. Averaged results from spectra taken in scans up and down are presented with standard deviation as error. Solid lines represent linear fittings (A, C and D) and exponential fittings (B) of the experimental data points. Reproduced with permission from *Faraday discussions, 205*, 233-243 (2017); published by the Royal Society of Chemistry. [3]

bias presented in Fig. 5.5B. The position of the band at $245\,cm^{-1}$ experiences a large red-shift upon bias increase independently of the environment or the value of constant set-point applied. The total shift within the potential window scanned is ca. $14\,cm^{-1}$. In contrast, no notable Raman shift is detected for the $997\,cm^{-1}$ band (Fig. 5.5C and D).

Tuning the current does not drastically affect the position of the bands at $245\,cm^{-1}$ (A) and $997\,cm^{-1}$ (C). The curves can be fitted to linear functions with slopes close to zero (Table IV). The largest shift is experienced by the $245\,cm^{-1}$ mode at 0.1 V, however the shift is as small as $1\,cm^{-1}$ through the whole current range scanned. Such small variations in peak positions while ramping I_t, together with the fact that the intensity changes discussed follow a relation as expected solely from a gap distance change, indicate that no chemical interaction is occurring while ramping the tunneling current. Ramping the bias voltage results in similar linear dependence of the position of the $997\,cm^{-1}$ band (fitting results are included in Table IV), while it induces shifts in the $245\,cm^{-1}$ Au-S mode.

E_b/V	slope/$cm^{-1}\cdot nA^{-1}$	
	245 cm^{-1}	997 cm^{-1}
0.1	0.9 ± 0.9	0.2 ± 0.3
0.04	0.1 ± 0.6	-0.4 ± 0.04
0.02	0.6 ± 0.3	0.01 ± 0.1
0.04 (water)	0.01 ± 1	-0.2 ± 0.2
I_t/V	slope/$cm^{-1}\cdot V^{-1}$	
	245 cm^{-1}	997 cm^{-1}
0.3	n.a.	1.7 ± 0.8
0.8	n.a.	0.7 ± 0.5
1.3	n.a.	2.2 ± 0.8
1.3 (water)	n.a.	0.6 ± 0.5

Table IV. Results of linear fittings to the Raman shift vs I_t data points of Fig. 5.5 A and C, and to the Raman shift vs E_b data points of Fig. 5.5 D.

The fact that only the $245\,cm^{-1}$ band shifts and this happens only when E_b is ramped, can be explained by the changing interaction strength of the S-Au bond when ramping the substrate potential (here E_b due to the technical specifications of our instrument). A similar effect has been found in the electrochemical TERS study for the N-Au interaction of adenine/Au(111) presented in Chapter 6. [4] To quantify the influence of the STM parameters on the position of the TERS bands, it would be interesting to quantify the binding strength between PhS and Au as a function of substrate potential in future experiments and theoretical simulations. An overall increase of the Raman shift in all experiments in water

with respect to the corresponding measurements in argon is found. This effect is currently under investigation by performing DFT calculations.

5.7 Conclusions

We have systematically studied the behavior of STM-TER spectra as a function of bias voltage and tunneling current set-point in Ar and in water experiments. In both cases, for the PhS/Au(111) system, I_{TERS} follows a dependence on the STM parameters in line to what would have been expected from a simple gap-distance reduction upon set-point increase or bias decrease.

In water, the intensity changes are found in general more moderate than in Argon experiments. Regarding the absolute intensity increase, tuning the bias voltage in the 0.5 to 0.02 V range results in an exponential band intensity increase while tuning the current set-point in the range of 0.1 to 1.7 nA shows a linear dependence in Ar. In practice, both parameters can be tuned to achieve optimal enhancement factors in STM-TERS experiments with best results obtained for I_t >1 nA and E_b <0.1 V for the given PhS/Au(111) system under study. If changing the bias voltage is achieved by tuning the potential of the sample with respect to the tip - as often the case with commercial STMs -, the interaction strength of the PhS-Au bond is altered when changing E_b. This results in Raman shifts of the Au-S stretch vibration while the other band positions in the spectrum remain unchanged. We conclude by pointing out the possibilities that a smart choice of STM parameters has for ultrasensitive TERS studies of solid/liquid interfaces and/or single molecules.

Chapter 6

EC-TERS: Potential induced molecular reorientation

In the present chapter, the capabilities of the EC-TERS are tested on a monolayer of adenine on Au(111). We can detect the vibrational fingerprint of less than 100 small, non-resonant adenine molecules, which gives information about their adsorption geometry and chemical reactivity as a function of applied potential. Combining experimental and simulation data, we conclude that protonated physisorbed adenine assumes a tilted orientation at low potentials while it is vertically adsorbed around the potential of zero charge. Further potential increase induces adenine deprotonation and reorientation to a planar configuration. The extension of EC-TERS to the study of adsorbate reorientation significantly broadens the applicability of this advanced spectroelectrochemical tool for the nanoscale characterization of a full range of electrochemical interfaces. This work demonstrates the capabilities of the setup to efficiently characterize these interfaces and is an important technological advance for the electrochemical and TERS scientific communities.

The content of this chapter has been published previously in Ref.[4]. Text and figures are reproduced with permission from *Angewandte Chemie Int. Ed.*, 88, 7108-7114 (2016), `http://onlinelibrary.wiley.com/doi/10.1002/anie.201704460/abstract`, Copyright 2017 Wiley-VCH Verlag GmbH & Co. KGaA, Weinheim. [4][a]

[a] the reader is referred to Wiley-VCH Verlag GmbH & Co. for further permissions regarding these materials

6.1 Introduction

One crucial parameter that determines surface reactivity or device functionality in a large variety of applications, such as heterogeneous catalysis, electrochemical energy conversion, biotechnology or molecular electronics, is the adsorption geometry of the (re)active molecules. For example, it has been suggested that the spatial tilt of π-bonds with respect to the substrate strongly influences the catalytic activity or electron conductance of adsorbates.[149–151] Accessing adsorbate orientation in relation to specific surface sites in situ or in operando is a first crucial step towards controlling interfacial geometries for improved device architecture. However, suitable in-situ techniques to study molecular orientation at well-defined adsorption sites are still scarce. Surface-specific in situ Raman- or IR-based linear and nonlinear vibrational spectroscopies (EC-SERS, EC-SEIRAS, EC-SFG) provide the required sensitivity and chemical specificity for investigating molecular geometries at potential-controlled solid/liquid interfaces at the ensemble level, i.e. the signals represent an average response from a large amount of molecules and surface sites present in the focus spot.[16,23,152,153] EC-SPM enables the visualization of individual adsorbate structures with nanometer spatial resolution, albeit at the expense of chemical specificity.[154,155]

TERS offers an elegant solution to achieve both the required surface (sub)monolayer chemical sensitivity and nanometer resolution. Our EC-TERS system, enables the study of the potential-dependent behavior of small non-resonant molecules adsorbed at an opaque substrate. As a showcase, we monitor the EC-TERS response of a monolayer of the DNA base adenine adsorbed at a well-defined Au(111) single crystal. Given the importance of understanding the interactions between DNA bases and noble metals for biosensing applications and for the development of biocompatible materials,[156,157] it is surprising that the DNA base orientation with respect to the Au surface (e.g. upright, tilted, flat) and the chemical state of the DNA base (e.g. (de)protonated, anionic) has remained a point of controverse discussion, despite extensive efforts to characterize the system with traditional CV approaches in combination with SPM or (ensemble) spectro-electrochemistry.[158–166]

EC-TERS offers the unique advantage of placing the near-field probe at a location of interest chosen according to the SPM topographic information gathered simultaneously. In contrast, in EC-SERS and EC-SEIRAS studies the substrate roughness leads to an inherent variation of the geometry of the surface adsorption sites. Thus, a broad distribution of molecular adsorption geometries is probed. Our approach enables selectively monitoring of potential-dependent TER spectral changes from less than 100 adenine molecules adsorbed at a Au(111) terrace due to a uniform adsorption geometry at the Au(111) surface

an averaging effect from different substrate/adsorbate geometries is limited. The experimental EC-TERS results are complemented with density functional theory (DFT) gas-phase approximations for data analysis and interpretation.

6.2 Materials and methods

Sample preparation

Ethanol (purity 99.9%) and adenine (A8626, purity $\geq 99\%$) from Sigma-Aldrich were used for sample preparation. To deposit the adenine monolayer, the annealed and clean substrate (Section 3.5.2) was immersed in 1 mM ethanolic solution of adenine for 8 hours and rinsed extensively with ethanol to remove multilayers. The sample was mounted in the home-made liquid cell described in Section 3.1.1 and Fig. 3.2.

0.01 M H_2SO_4 was used as electrolyte and degassed with Ar (Argon 6.0, A00560150 Westfalen) before use. A gold wire (Mateck, 5N, 0.25 mm diameter) was used as micro counter electrode and a homemade Pd/H_2 wire as reference electrode (electrode preparation described in Section 3.3) mounted into the liquid cell immediately after preparation. For convenience, all potentials are reported vs Ag/AgCl 3 M. In order to convert properly between electrodes the voltage between the Pd/H_2 and a commercial Ag/AgCl (SI Analytics, 3 M KCl) was measured and found to be equal to 0.2 ± 0.01 V.

To keep cleanliness during the experiment, a soft Ar flow (0.5 bar through a 0.5 cm diameter Teflon tube) was always poured on top of the EC-cell except during spectral acquisition and STM imaging to ensure stability and prevent the tip from crashing.

Experimental procedure

The sample was mounted into the setup and directly immersed in electrolyte at 0.2 V vs Ag/AgCl. The tip was approached into tunneling conditions.

To keep the gap distance constant (requirement explained in Section 3.3), we fixed E_{bias} at 0.4 V and I_t at 1.35 nA throughout experiment. Due to the electrode configuration, the system adjusts the potential of the tip accordingly while ramping the sample potential to keep a difference of 0.4 V between E_{tip} and E_{sample}, according to the relation E_{tip}=E_{sample}-E_{bias} (see Section 3.3).

CVs were recorded periodically during the course of the experiment to check the state of the monolayer. After a first CV, STM images were acquired to find a spot for spectral acquisition in the middle of a flat Au(111) terrace. Topographical images at different sample potentials were taken. These images do not show

any differences at the spatial resolution reached with our device. A second CV was taken after the images and right before spectral acquisition. Afterward, EC-TER spectra were acquired while ramping the sample potential. For each potential value, approached (TERS) and 20 nm retracted (by disabling piezo-control) spectra are taken to check the tip cleanliness. All spectra presented here were acquired at a laser power of 1.77 mW (at the exit of the objective, losses are expected at the sample due to the liquid cell) and acquisition time of 5 s; an average of 5 spectra is presented for each potential. No further correction has been applied. After spectral acquisition, an additional CV is recorded. The tip cleanliness was checked in an air TERS experiment on a clean Au(111) substrate after the EC-TERS experiment.

6.3 Results

A neutral adenine molecule is depicted in Fig. 6.1a. All spectra were recorded with the tip located in the center of a flat Au(111) terrace (Figure 6.1b, white dot) as confirmed by EC-STM imaging prior to and after spectral acquisition. The STM image shows the Au(111) electrode flat terrace and step (of approximately 0.2 nm height as shown in the profile plotted in 6.1b, right), however the resolution does not allow identification of individual adenine molecules.

Figure 6.1c shows EC-TER spectra recorded at different sample potentials (E_{sample}) in chronological order of acquisition from bottom to top. At low potentials, one prominent peak is present at ca. 736 cm^{-1} (ring-breathing), and weaker bands appear at around 1320 cm^{-1} (CN and CC stretch) and 1464 cm^{-1} (N7-C8 stretch, C8-H bend and NH_2 scissor), in agreement with previous reports of adenine/Au(111).[125,165,167–169] At all potentials, a broad band features below 300 cm^{-1} that can be decomposed into three components with help of Lorentzian band fitting (Figure 6.1d): The two peaks located at 172 and 220 cm^{-1} are also observed in all far-field spectra acquired upon tip retraction and do not show any potential-dependent changes; as their molecular origin is unclear, they will not be discussed further. Notably, the fitting reveals a near-field band at $\approx 260\,cm^{-1}$ at potentials > 0.6 V that has been assigned to Au-N interactions.[169] Details of the fitting of the low wavenumber region are given in Section A.2.

Fig. 6.1c displays example of spectra at different sample potentials. During the experiment, several ramps from low to high potentials and vice-versa were taken during a total time of 40 minutes, in order to verify the reproducibility and stability of the spectral changes. Fig. 6.2 shows the intensity evolution of the ring-breathing mode (736 cm^{-1}) during the mentioned up and down potential ramps. For each spectrum acquired (horizontal axis represents the temporal se-

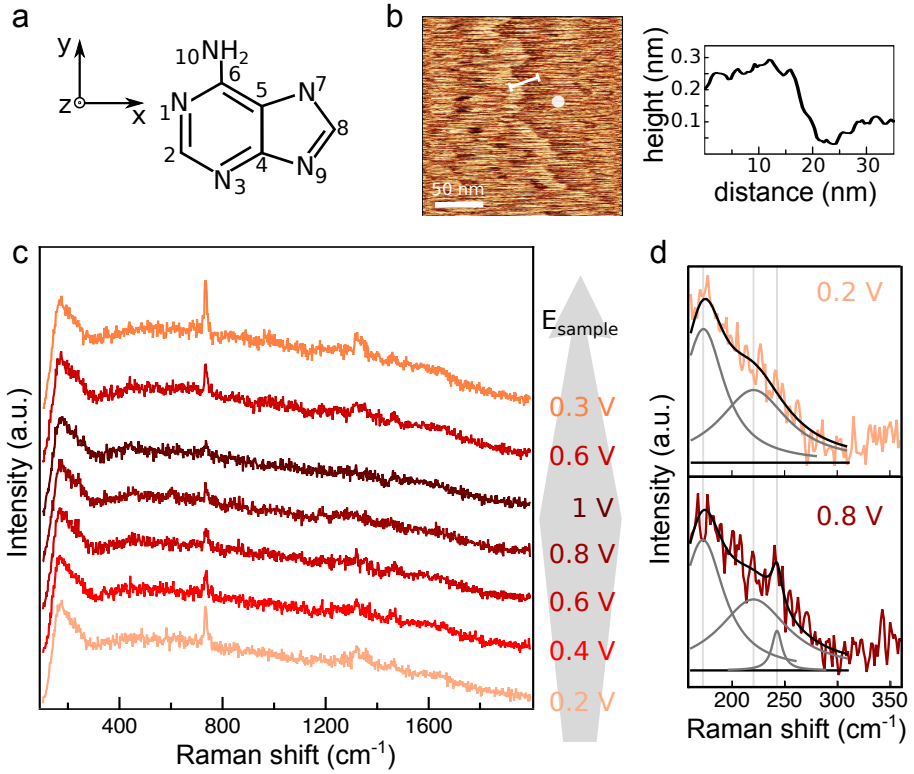

Figure 6.1. a: neutral adenine sketch. b: Left: 228x228 nm^2 STM image ($E_{sample} = 0.5$ V, $E_{bias} = 0.4$ V, $I_t = 1.35$ nA); white dot indicates EC-TERS position. Right: Au step profile as indicated in STM image. c: EC-TER spectral evolution upon E_{sample} potential ramp (1.77 mW laser power, 5 s acquisition time). d: Lorentzian band fitting example for the low wavenumber region at 0.2 and 0.8 V E_{sample}. Reproduced with permission from *Angewandte Chemie Int. Ed.*, 88, 7108-7114 (2016); Copyright 2017 Wiley-VCH Verlag GmbH & Co. KGaA.[4]

quence of measurements) the corresponding potential (white dots, right vertical axis) and the integrated peak intensity (black dots, left vertical axis) are plotted. For sufficiently high potentials, the 736 cm^{-1} peak disappears, to appear again upon potential decrease. The trend is consistent during the whole experiment. Importantly, the full band intensity can always be recovered, indicating a constant surface coverage upon potential ramps.

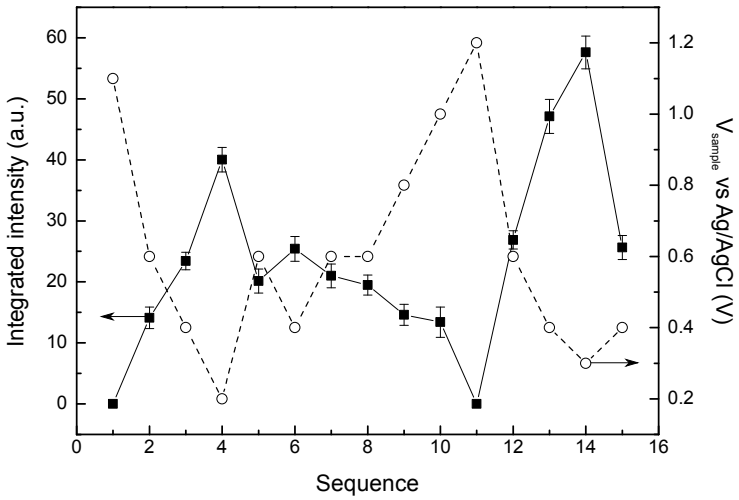

Figure 6.2. Overview of the sequence of EC-TER spectra at different potentials. Integrated intensity of the 736 cm^{-1} ring-breathing mode (solid dots joined by solid line, left vertical axis) as a function of the consecutive measurements at different potentials (empty circles, dashed line, right vertical axis). Reproduced with permission from *Angewandte Chemie Int. Ed.*, 88, 7108-7114 (2016); Copyright 2017 Wiley-VCH Verlag GmbH & Co. KGaA.[4]

To analyze the spectral changes as a function of E_{sample}, we plot amplitude and peak frequency of the 260, 736 and 1464 cm^{-1} modes obtained from Lorentzian fits (Fig. 6.3, fitting details in Section A.3). The corresponding CV recorded at 50 mV/s inside the EC-TERS cell is shown as inset in Figure 6.3B.

The CV exhibits the two well-known peaks at 0.36 and 0.62 V (0.34 and 0.59 V) in the anodic (cathodic) scan direction[160,161,163]. The first peak can be attributed to an increase in capacitance as a result of molecular reorientation from a physisorbed tilted arrangement to a vertical geometry around the potential of zero charge,[170] such that more Au surface is exposed to the adenine-free electrolyte, in agreement with previous studies.[159,161,171] The second peak at around 0.6 V results from deprotonation and partial charge transfer from adenine to the Au electrode (around 0.68 electrons per molecule as determined by Aldaz and corworkers[172]).[159,161,171] Note that the oxidation of adenine

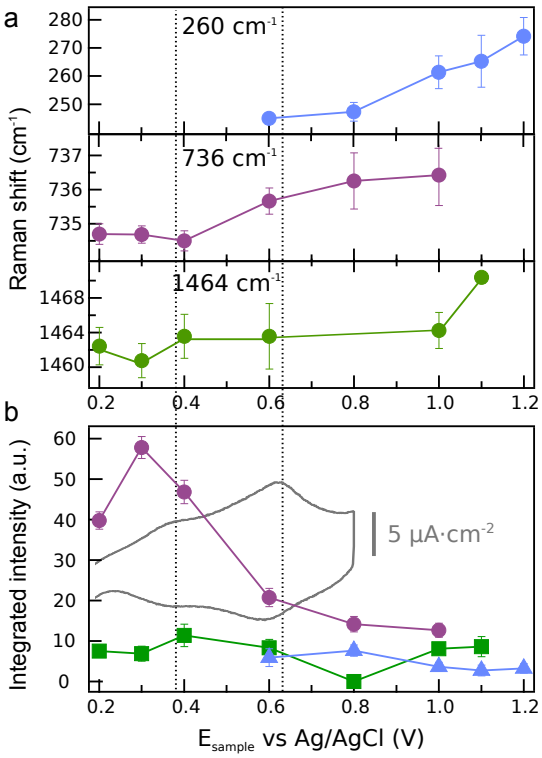

Figure 6.3. a: Raman shift and b: integrated intensity of the the 260 cm^{-1} (blue), 736 cm^{-1} (purple) and 1464 cm^{-1} (green) bands as a function of sample potential. Error bars result from fittings. CV of a monolayer of adenine on Au(111) in 0.01 M H_2SO_4, v = 50 mV/s (b, inset). Reproduced with permission from *Angewandte Chemie Int. Ed.*, 88, 7108-7114 (2016); Copyright 2017 Wiley-VCH Verlag GmbH & Co. KGaA.[4]

to its oxo forms occurs at potentials higher than 1.2 V, i.e. outside our potential window.[173,174] Importantly, the CV was identical before and after the EC-TERS experiment (after ramping up to 1.2 V several times), indicating that (partial) Au oxidation does not alter the adenine behavior at the electrode (see Section 6.3.1 for further details).

The Au-N mode at ca. 260 cm^{-1} only appears after the second anodic peak and blue-shifts from 245 cm^{-1} at 0.6 V to 274 cm^{-1} at 1.2 V (Figure 6.3a, blue) while maintaining a constant intensity (variations within the noise level, Figure 6.3b, blue). In contrast, the intensity of the 736 cm^{-1} mode shows a maximum at 0.3 V (Figure 6.3b, purple). It shows an initial intensity increase from 0.2 to 0.3 V. In the region between the two anodic peaks in the CV (between 0.36 and

0.62 V), the band significantly drops in intensity and further decreases after the second peak at a less pronounced rate before disappearing at potentials >1 V. Furthermore, the band shows a small, but measurable blue shift from 734.6 cm^{-1} at 0.3 V to 736.4 cm^{-1} at 1 V (Figure 6.3a, purple). The 1464 cm^{-1} mode shows a constant intensity between 0.2 and 0.6 V. It vanishes at 0.8 V to reappear at 1 V (Figure 6.3, green). This band blue-shifts by ca. 10 cm^{-1} at high potentials.

6.3.1 Cyclic voltammetry of adenine/Au(111)

The EC-TERS system is designed to provide optimal spectroscopic results, thus the performance of STM imaging and voltammetry are limited by the requirements of the optical setup. The CV shown in Fig. 6.3 is taken in the EC-TERS liquid cell, which has a capacity of less than 10 mL of electrolyte. The electrolyte is degassed prior to insertion in the TERS cell and Ar flow is poured on top of it during the experiment to avoid oxygen contamination of the solution. In spite of these precaution measures the voltammetry results acquired in the EC-TERS cell are not as precise as they would be in a standard electrochemical

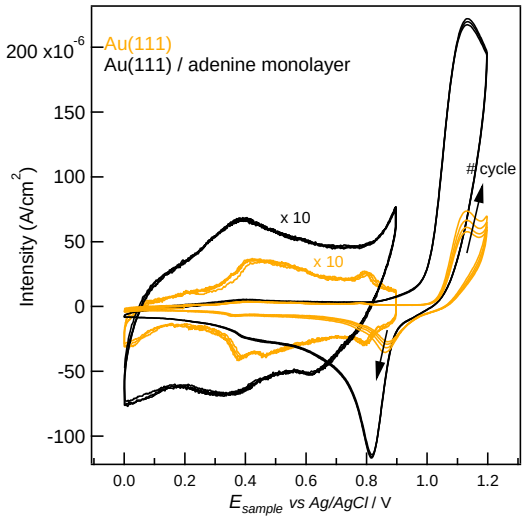

Figure 6.4. Comparison of the CV of pristine Au(111) (yellow) and a monolayer of adenine in Au(111) (black) in 0.01 M H_2SO_4 acquired up to 0.9 V and in the full potential window. Scan rate 20 mV/s. 4 cycles for each CV are included. Reproduced with permission from *Angewandte Chemie Int. Ed.*, 88, 7108-7114 (2016); Copyright 2017 Wiley-VCH Verlag GmbH & Co. KGaA.[4]

cell. To corroborate the previous results, CVs of the same gold electrode used in the EC-TERS experiments are taken in a standard EC cell using a potentiostat (Schlumberger/Solartron 1286). The results are displayed in Fig. 6.4.

Cyclic voltammograms of a monolayer of adenine adsorbed in Au(111) in adenine-free electrolyte in the low potential region up to 0.9 V and in the full potential range up to 1.2 V are included in black. In yellow, the corresponding CVs of pristine Au(111) in the same electrolyte are displayed. These data are obtained in adenine-free electrolyte (0.01 M H_2SO_4) with Au wire as a counter electrode and a Ag/AgCl 3 M reference electrode.

The voltammetry of Au(111) shows the expected shape (Fig. 6.4, yellow): [175,176] a first peak is observed around 0.41 V that results from the lifting of the Au surface reconstruction. The peak at 0.8 V is due to sulfate adsorption. Upon further potential increase, oxidation of the Au surface is observed. The first peak at 1.13 V corresponds to the first electron transfer (OH deposition) and a second peak starts to rise at higher potentials but its position cannot be determined in the investigated potential range. The second peak corresponds to the transfer of the second electron for Au oxide formation. The corresponding reduction peak in the cathodic scan is observed at 0.81 V.

The CV of adenine/Au(111) (Fig. 6.4, black) shows a markedly different behavior than the pristine Au crystal. The measured currents are higher in this case than in the previous one. Like in the CVs acquired in the EC-TERS cell, we observe two distinct reversible peaks at ca. 0.36 and 0.62 V in both anodic and cathodic scan directions. The CV taken in the EC-TERS cell (displayed in Fig. 6.3) is nicely reproduced in the conventionally recorded CV (comparison in Fig. 6.5). The peaks are also visible in the full potential range CV, however, partially masked by the strong current increase above 0.9 V. This oxidation peak can be attributed to an increased charge transfer from the NH_2 lone pair of adenine to the Au d*-band and/or Au surface oxidation.

6.4 Discussion

Different phenomena, like changes in surface coverage, chemical conversion, molecular reorientation and charge effects, could account for the observed potential-dependent spectral changes.

Similar intensity variations of the ring-breathing mode have been attributed to changes in the coverage in an adenine-containing electrolyte in an ensemble study. [165] As we work in adenine-free electrolyte, an increase in coverage would be uniquely due to molecular diffusion. By integrating over 5 s per spectrum and averaging over 5 spectra per data point, however, we average over random

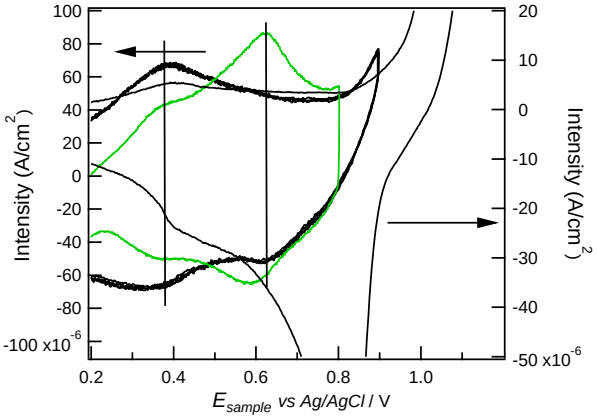

Figure 6.5. Comparison of the CV of adenine/Au(111) recorded in the standard EC cell (black & grey) with the CV taken in EC-TERS cell during TERS experiment (green). Reproduced with permission from *Angewandte Chemie Int. Ed.*, 88, 7108-7114 (2016); Copyright 2017 Wiley-VCH Verlag GmbH & Co. KGaA. [4]

fluctuations produced by diffusion into and out of the hot spot. Furthermore, the recovery of the 736 cm^{-1} upon sweep reversal (Fig. 6.2) and the constant intensity of the other Raman peaks (Fig. 6.3) as well as of the CV features (Section 6.3.1) corroborate that the surface coverage in the near-field region remains constant throughout the hour-long experiment set.

According to literature, one adenine molecule occupies a surface area between 0.41 nm^2 (upright) and 0.55 nm^2(flat).[172] The TERS spatial resolution for small, non-resonant molecules in a Au-tip/Au-sample gap lies in the order of a few nm where the near-field is sufficiently strong to provide detectable TER scattering.[177–180] With an effective TERS scattering radius of 6 nm, we estimated that the number of probed adenine molecules is in the range of 50 and 70, demonstrating the extreme sensitivity that our EC-TERS setup holds particularly for non-resonant species.

6.4.1 Adenine protonation and shift of Raman bands

In acidic media, (de)protonation from N1-protonated to neutral adenine has been suggested to occur upon potential sweep at around 0.6 V. Deprotonation facilitates chemisorption with a partial charge transfer from N lone-pairs of adenine to d* band of Au(111) at higher potentials.[160–162,165] As a transition between protonated, neutral and partially oxidized adenine may induce band shifts, we have performed gas-phase DFT calculations (details in Appendix B)

to compare the Raman shifts predicted for cationic, neutral and N1-protonated molecules.

Giese *et al.* used theoretical DFT data to assign their experimental bands at ca. 723 and 1483 cm^{-1} to the theoretically calculated ring-breathing mode (at 726 cm^{-1} in their calculations) and to the str. N7-C8, bend C8-H and sciss. NH_2 (at 1524 cm^{-1} in the calculations).[168] Similarly, we assign the experimental modes at 736 and 1464 cm^{-1} to the simulated modes around 723 cm^{-1} (ring-breathing) and at ca. 1513 cm^{-1}, respectively, based on the mode displacements returned by the calculations (shown in Fig. 6.6, with exact frequencies in the calculations at 725.71 cm^{-1} and 1514.03 cm^{-1} for the neutral adenine molecule) in agreement with previous reports.[167,168]

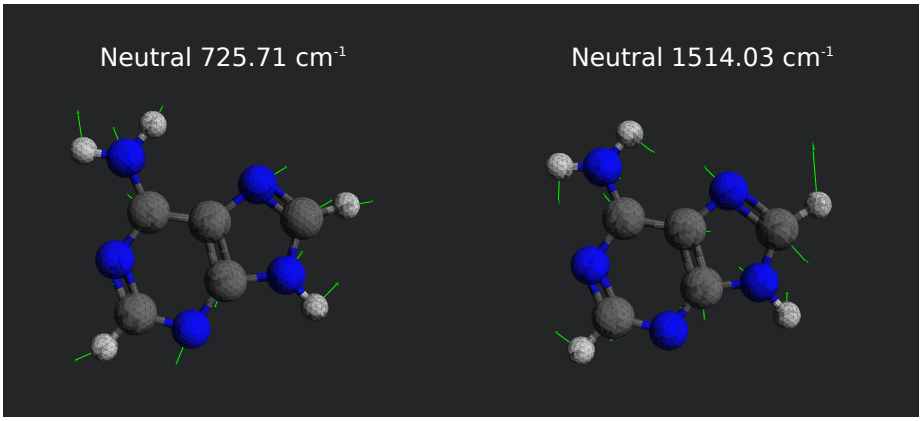

Figure 6.6. Atomic displacements calculated for the modes at 725.71 cm^{-1} (ring-breathing) and 1514.03 cm^{-1} (str. N7-C8, bend C8-H and sciss. NH_2) of neutral adenine assigned to the experimental bands at 736 and 1464 cm^{-1}. Reproduced with permission from *Angewandte Chemie Int. Ed.*, 88, 7108-7114 (2016); Copyright 2017 Wiley-VCH Verlag GmbH & Co. KGaA.[4]

The DFT calculations predict a blue-shift from 721.69 (1511.89) cm^{-1} for the protonated molecule to 725.71 (1514.03) cm^{-1} for the neutral case to 731.72 (1569.53) cm^{-1} for the cation. Note that adenine is not fully oxidized within our potential window as discussed earlier; the cation calculation merely serves to confirm the trend of the Raman shift due to deprotonation and partial charge transfer upon chemisorption. This trend is in qualitative agreement with the blue-shifts of 2 and 10 cm^{-1} observed experimentally for the 736 and 1464 cm^{-1} modes, respectively.

In addition, previous pH-dependent SERS experiments showed that at low pH, the intensity ratio of the 1320 and 1350 cm^{-1} bands is higher for the protonated species than for neutral adenine.[169] Fig. 6.7a shows the fitting results of the

bands at 1320 and 1350 cm^{-1} in our experiments. The intensity ratio between them (I_{1320}/I_{1350}), presented in Fig. 6.7b, decreases upon potential increase. This observation further supports the conclusion that at potentials < 0.6 V, adenine molecules are protonated. After deprotonation at ca. 0.6 V neutral adenine is detected.

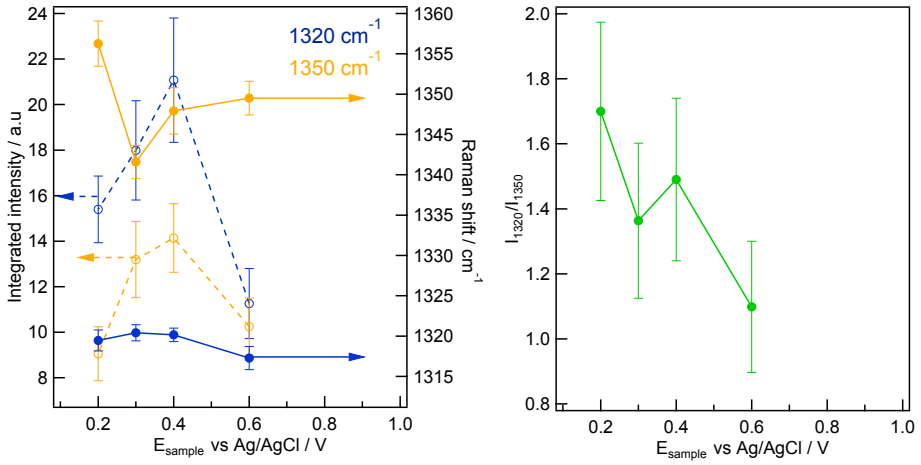

Figure 6.7. a. Fitting results of the two bands at 1320 (blue) and 1350 cm^{-1} (orange). Band position indicated in solid circles, solid line and intensity indicated with open circles and dashed lines. b. Intensity ratio between bands at 1320 and 1350 cm^{-1}. Reproduced with permission from *Angewandte Chemie Int. Ed.*, 88, 7108-7114 (2016); Copyright 2017 Wiley-VCH Verlag GmbH & Co. KGaA. [4]

While potential-induced deprotonation explains the observed band shifts and small variations in relative band intensities, it does not account for the drastic intensity changes of the prominent ring-breathing mode.

6.4.2 Molecular reorientation and induced intensity changes

The Raman scattering intensity is proportional to the 4th power of the polarizability. [42] Because of the tensorial nature of the polarizability, potential-dependent molecular reorientation is expected to manifest itself in strong intensity changes as observed in the EC-TER spectra, provided the tensor elements exhibit anisotropy that is largely maintained upon adsorption. Note that in TERS, the excitation (near-)field is oriented parallel to the surface normal. [28] As such, the field efficiently excites vibrations with large polarizability components in the long tip axis (surface normal). For example, in-plane modes (as

the ring-breathing mode of adenine at 736 cm^{-1}) appear more intense in the Raman spectrum if the molecular plane is oriented parallel to the incident field, i. e. if the molecules stand vertically on the substrate, with the molecular plane parallel to the long tip axis. In contrast, the mode does not appear in the spectrum if the molecules stand horizontally in the surface, with the molecular plane perpendicular to the tip axis. With knowledge of the respective Raman polarizability tensors of the vibrational modes of interest, the molecular orientation of the few molecules in the nanometer-confined near-field spot at the flat Au(111) terrace can be deduced from the observed intensity changes. [27,28]

As a first approximation, we have calculated the transition polarizability tensors of the 723 and 1513 cm^{-1} modes of an isolated molecule in protonated and neutral forms with DFT. Details of the calculations and the complete tensors are given in Appendix B. In our calculations, x,y,z is the coordinate system on the molecule. The z-axis is perpendicular to the rings' plane (containing the x-/y-axes, with y (short axis) parallel to the C4−C5 bond (Fig. 6.8a and d). X', Y' and Z' represent the fixed axes of our experimental configuration. The Y'-axis is parallel to the long axis of the tip (and therefore the excitation field) and the X',Z'-axes define the plane of the substrate surface.

The diagonal elements of the Raman tensors for the 723 cm^{-1} mode show a pronounced anisotropy between the x,y-plane of the adenine rings and the z-component for both protonated and neutral species with a ratio of $\alpha_{xx} : \alpha_{yy} : \alpha_{zz} = 3:3:1$. The Raman tensor of the 1513 cm^{-1} mode shows a pronounced anisotropy within the x,y-plane with a ratio of 14:1:1 for the neutral form of adenine and 20:2:1 for the protonated case.

We have calculated the intensities of the 723 and 1513 cm^{-1} modes (neutral and protonated) for an upright to planar transition in two situations:

1. for the y-axis of the molecular plane initially parallel to the excitation field (Y') and a tilt angle, θ, around the x-axis of the molecule (Fig. 6.8a)

2. for the x-axis of the molecular plane initially parallel to the excitation field (Y') and a tilt angle, θ, around the y-axis of the molecule (Fig. 6.8d).

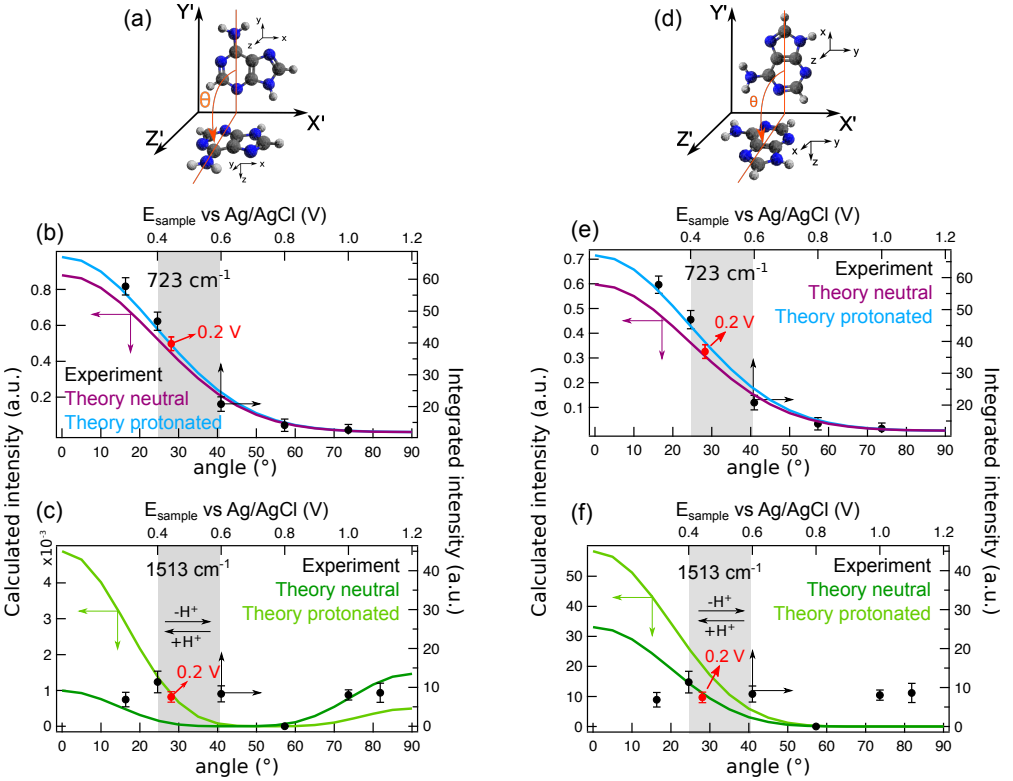

FIGURE 6.8. a: Schematic depiction of a rotation of the adenine molecules around the x-axis (d: y-axis) of the molecule, the excitation EM field is polarized in the Y'-direction. Orientation-dependent calculated Raman intensities of the 723 cm^{-1} (b) and 1513 cm^{-1} (c) modes in neutral (b purple, c dark green) and protonated (b blue, c light green) forms for the rotation depicted in a. e and f: same for rotation around the y-axis (d). The experimental data points (black or red solid circles) of both modes are included for comparison. The gray shaded areas indicate the potential region where deprotonation is expected. Reproduced with permission from *Angewandte Chemie Int. Ed.*, 88, 7108-7114 (2016); Copyright 2017 Wiley-VCH Verlag GmbH & Co. KGaA. [4]

Fig. 6.8b displays the simulated intensity variation of the 723 cm^{-1} mode (c: 1513 cm^{-1}) for rotation 1. The ring-breathing mode intensity is largest for a tilt angle of $\theta = 0°$ and slowly decreases with molecular reorientation to a flat configuration at $\theta = 90°$. The simulation results for protonated (purple solid line) and neutral adenine (blue solid line) show the same trend. The experimental data (black solid circles) are included in the graph and match perfectly the obtained trends with low potentials corresponding to small tilting angles (vertical arrangement). The agreement is also good considering the deprotonation occurring between peaks in the CV (gray shaded area). The lower band intensity of the ring-breathing mode at 0.2 V (red solid circle) below the potential of zero charge, which has also been observed in previous EC-SERS experiments, [165,181] is consistent with a tilted physisorbed adsorbate orientation as deduced from EC experiments and discussed above. In other words, the experimentally observed 736 cm^{-1} band intensity behavior as a function of increasing potential can be explained with adenine reorientation from tilted to upright to flat with respect to the Au(111) surface.

The simulation results for the 1513 cm^{-1} mode show that for both the protonated and neutral cases, the peak intensity drops to zero at intermediate angles between ca. 40° and 60° while at smaller or larger angles, the peak is expected to have higher intensity (Fig. 6.8c). The experimental data show such behavior: the peak vanishes at 0.8 V while at lower and higher potentials the measured intensity is constantly higher. The quantitative deviation between the absolute intensity values of experimental and simulations for this mode may be related to the fact that the gas-phase simulations do not take into account any molecule-molecule or molecule-substrate interactions. The 1513 cm^{-1} mode involves the NH_2 moiety that has been suggested to enable adenine adsorption on Au. [166] Therefore this vibration is expected to be more affected by the exclusion of the electrode in the simulations than the delocalized ring-breathing mode. Simulations of adenine at solid/liquid interfaces beyond gas-phase calculations could give polarizability tensors describing better the experimental results.

The results for the ring-breathing mode at 723 cm^{-1} for rotation 2 (Fig. 6.8d) are shown in Fig. 6.8e and are equivalent to the results obtained for rotation 1. This results are expected since the x and y components of the polarizability tensor are very similar ($\alpha_{xx,neutral} = 0.879261 \approx \alpha_{yy,neutral} = 0.968468$ and $\alpha_{xx,prot} = 0.919670 \approx \alpha_{yy,prot} = 0.995191$, Appendix B). The trends of protonated and neutral adenine are similar and consistent with the experimental data points for an increasing tilt angle θ with increasing potential.

The results for the 1513 cm^{-1} mode presented in Fig. 6.8f, show that for both neutral and protonated species, the intensity of the band is expected to decrease upon angle increase, with higher absolute intensity values for protonated than

for neutral adenine. The different behavior between rotation 1 and 2 arises from the fact that α_{xx} is, for both protonated and neutral case, one order of magnitude higher than α_{yy} and α_{zz}. Comparing the results of the simulations in Fig. 6.8 f with the experimental data, we observe that the agreement between them is qualitatively worse than the one obtained for rotation 1 presented in Fig. 6.8 c. In the experiment, the mode at 1464 cm^{-1} is present through the whole potential window at constant intensity, except at 0.8 V when it vanishes, behavior that is qualitatively consistent with the simulation results for the geometrical configuration of rotation 1.

Based on the described observations, we conclude that the adenine monolayer transitions from a vertical to a planar orientation with respect to the gold electrode upon potential increase (and deprotonation) with the y-axis in the molecular plane (short axis of the adenine plane) initially parallel to the long axis of the tip (Y'-axis). Note that while in reality, the molecule can obviously also adopt an off-axis geometry (including rotation around the defined axes), these two simplest approximations discussed here already describe the experimental data surprisingly well.

Adenine reorientation from vertical to horizontal upon potential increase above 0.3 V is further supported by analysis of the low-wavenumber mode at ca. 260 cm^{-1}. This band has previously not been investigated experimentally in detail, despite the wealth of information it contains about the adsorbate-substrate interaction. Interestingly, the Au-N mode only appears at potentials >0.6 V after deprotonation. The significant blue-shift from 245 to 274 cm^{-1} can be attributed to a strengthening of the Au-N bond with increasing potential, i.e. an increasing interaction between the N lone pairs and the metal d*-band that results in a planar orientation of adenine. Coordination of neutral adenine through the amino group N10 and N1 at potentials above the anodic peaks in the CV is consistent with all observed trends. The lack of the Au-N mode at potentials <0.6 V is in line with weakly physisorbed adenine where the monolayer is stabilized by π-d* adsorbate-substrate or π-π intermolecular interactions at potentials below or around 0.3 V, respectively.[159,164,166] Figure 6.9 summarizes the adsorption/reaction model of the potential-dependent, reversible adenine (de)protonation and reorientation as deduced from our EC-TERS results.

6.5 Conclusions

To summarize, we have demonstrated how the EC-TERS setup can be efficiently used to study the electrochemical behavior of small non-resonant molecules at electrified interfaces with a few nanometer spatial chemical resolution and < 100 molecules sensitivity. For the showcase adenine/Au(111) system, EC-

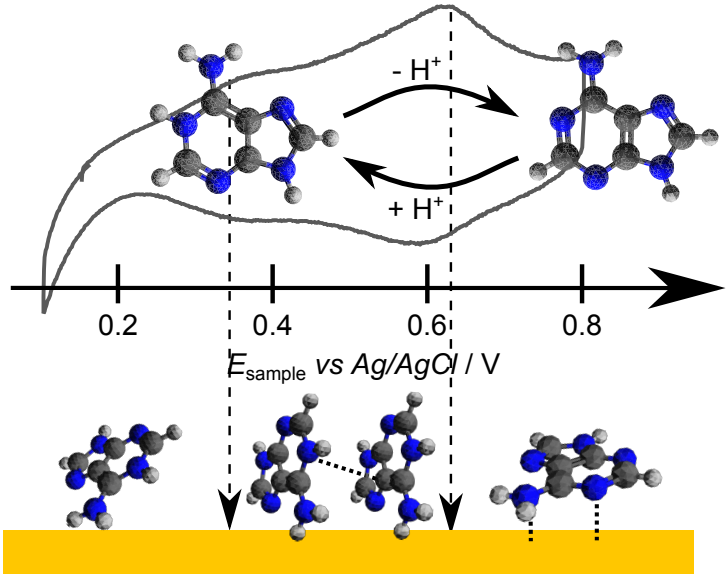

Figure 6.9. Proposed potential-dependent adsorption/reaction model for adenine/Au(111). Reproduced with permission from *Angewandte Chemie Int. Ed.*, 88, 7108-7114 (2016); Copyright 2017 Wiley-VCH Verlag GmbH & Co. KGaA. [4]

TERS in combination with DFT results allow us to deduce a reversible adsorption/reaction model where protonated adenine is adsorbed at atomically flat Au(111) in a tilted geometry at low potentials and in an upright configuration with its short molecular axis perpendicular to the surface around the potential of zero charge. Upon potential increase, the molecule adapts a flat adsorption geometry with strong Au-N interactions between deprotonated adenine molecules and the gold substrate. With this important extension of EC-TERS capabilities to evaluate adsorbate orientation and chemical conversion as a function of potential, in-situ local chemical information at the nanoscale becomes accessible for a full range of electrochemical systems.

Chapter 7

Outlook

The work presented in this thesis demonstrates the efficient extension of a standard TERS system operating in air to work in liquid and electrochemical environment. The liquid and EC-TERS experiments described offer an overview of the challenges that need to be taken into account when building an EC-TERS setup and the way to interpret the obtained results.

In Chapter 4, a systematic characterization of liquid TERS is offered. We find that, in side-illumination instruments, focus distortion in liquid results in a reduction of TERS intensity by a factor of 3 with respect to air. Despite intensity decrease, reproducible liquid TERS for resonant and non-resonant species has been shown with enhancement factors as high as 10^5. In order to correct focus distortion, phase modulation of the beam with a spatial light modulator is being tested. Our preliminary results show the power of this approach recovering TERS intensity lost by focus distortion. In air, beam modulation can also be used to raise the weak intensities or Raman bands. This approach offers a promising tool to increase TERS sensitivity in air and liquid experiments.

The TERS intensity has been found to depend on the gap distance by a factor $\propto d^{-10}$ in air. The gap distance in STM is indirectly set by adjusting the bias voltage between tip and sample and the tunneling current. In Chapter 5 we test the dependency of TERS intensity on these parameters in experiments performed under controlled Ar atmosphere and in water. We find that the dependency of the TERS intensity on bias and tunneling current follow a simple distance dependence model in both argon and water experiments. In the range of values scanned (tunneling current between 0.1 and 1.8 nA and bias voltage between 0.02 and 0.5 V), the bias voltage is found to affect stronger the intensity of Raman bands than the tunneling current. We find that working at bias lower

than 0.1 V and tunneling current higher than 1 nA maximizes TERS intensity while the resulting gap distance is still safe enough to avoid tip crash into the sample.

In Chapter 6 a proof-of-principle EC-TERS experiment is presented. EC-TERS from a monolayer of adenine in a Au(111) electrode in acidic media combined with DFT calculations provide a deep characterization of the electrochemical interface. We find that the molecular orientation changes as a function of applied potential. Tilted physisorbed adenine is protonated in the surface at low potentials. After passing the potential of zero charge a vertical arrangement is adopted. Increasing further the potential of the sample, adenine deprotonates resulting in chemisorption in a tilted orientation. These results show the impressive capabilities of our EC-TERS to characterize electrochemical interfaces. TER spectra combined with CV provide complete information about the chemistry, electron transfer and geometry of the molecular monolayer at the surface as a function of electrode potential.

This work offers important information about the characteristics of TERS spectra in liquid and electrochemical environments. The presented results together with the recent work of other groups on EC-TERS set the bases for the use of TERS in realistic working conditions. While EC-TERS has been shown in side, top and bottom-illumination, with STM and AFM-based systems many aspects of the instrument still remain unexplored. Gap-mode experiments or resonant molecules have been mostly reported, and the feasibility of the experiments for combined non-resonant and no gap-mode experiments need still to be investigated. Ideally, 2D EC-TERS mapping of electrochemical interfaces may offer additional insight into the role of, for example, individual active sites. The differences between air and electrochemical experiments in terms of background changes could also offer additional information about the enhancement mechanisms in liquid and used for further optimization. As shown in Chapter 6, theoretical calculations are essential in EC-TERS to interpret the experimental results. We use a simplified model based on isolated gas-phase Raman response of the molecules studied. However, it is important to develop the used models to take into account the real system studied: near-field Raman, adsorbate-substrate ensemble and surrounding dielectric (electrolyte). While the work is not yet finished and further development and characterization are required, EC-TERS is now a reality that can be used to study important electrochemical systems and to answer important open questions in catalysis, energy-conversion schemes, biology or synthesis.

Appendices

Appendix A

Spectral analysis

In this appendix all the details of spectral analysis used during Chapters 4, 5 and 6 are expained.

All the analysis for the different experiments was performed using default and user-programmed functions of Wavemetrics Igor Pro 6.34A and 7. Additionally, some functions of LabSpec 6 (the software of the Horiba spectrograph/CCD detection system) were used for preliminary analysis as smoothening or despiking.

In general, all the peak fittings presented through this thesis correspond to Lorentzian fittings, i. e. fitting of the data points to a Lorentzian function with expression:

$$y(x) = y_0 + \frac{A}{(x - x_0)^2 + B} \tag{A.1}$$

The parameter x_0 corresponds to the maximum of the Lorentzian function (or peak position/frequency), y_0 corresponds to the baseline, while A and B give information about the height (I), the area and the FWHM of the fitted peak: $FWHM = 2\sqrt{B}$ and $I = A/B$.

Igor Pro has defined functions (MultiPeakFitting) to fit peaks in a spectrum, where the baseline is adjusted by the user and constraints (exact value or ranges of height, position, FWHM etc.) can be applied. If not stated differently, the peaks in the spectra presented in this thesis are free fits (no constraints) of reduced spectral ranges (chosen to contain the specific peak and enough data points before and after to determine the S/N ratio of the spectrum). A linear baseline is applied since the reduced fitting range hides the large and inhomogeneous TERS backgrounds.

The following sections explain specific details about important (or unconven-

tional) fitting procedures.

A.1 Background fitting

This section contains the information about background fittings of the TER spectra in air and water for PhS and MGITC in Chapter 4.

For a given pair of TER spectra (air and water for the same molecule), the same mask was applied to exclude the Raman intense bands that could lead to fitting errors. The remaining data points of the spectrum were fitted with a Lorentzian function (Eq. A.1). A Lorentzian function has been found to describe well the shape of experimental TERS backgrounds.

The original spectra of MGITC together with the fitting and the position of the maximum for air and water are presented in Fig. A.1. To compare the two spectra, we normalized them to the 1175 cm^{-1} band (indicated with an asterisk in the graph). In Fig. A.2, the spectra and fittings for the PhS experiments are shown. Table I contains all the parameters returned by the fitting procedure.

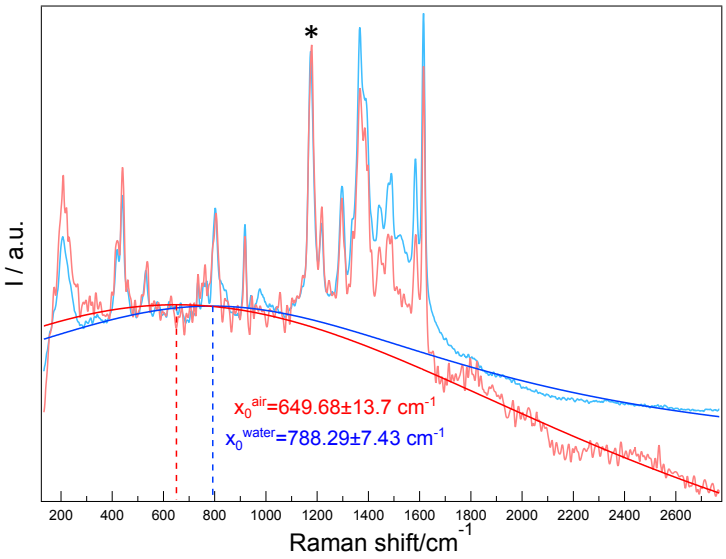

FIGURE A.1. TERR spectra of MGITC/Au(111) in air (light red) and water (light blue) normalized to the 1175 cm^{-1} band (marked with an asterisk). Lorentzian backgrounds in air (red) and water (blue) with their maximum positions. Reproduced with permission from *Analytical Chemistry, 88*, 7108-7114 (2016); Copyright 2016 American Chemical Society. [1]

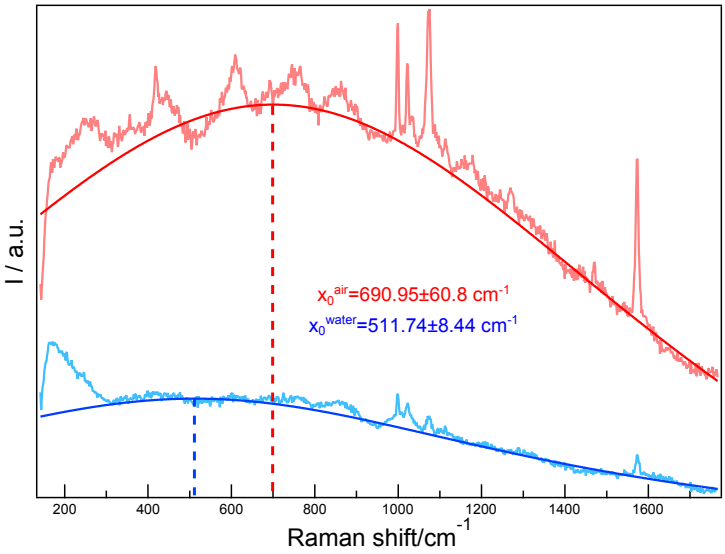

FIGURE A.2. TER spectra of PhS/Au(111) in air (light red) and water (light blue). Lorentzian backgrounds in air (red) and water (blue) with their maximum positions. Reproduced with permission from *Analytical Chemistry, 88*, 7108-7114 (2016); Copyright 2016 American Chemical Society. [1]

A.2 Low wavenumber fittings in liquid and electrochemical experiments

As shown in Chapters 5 and 6, all our Raman experiments performed in liquid environment (far-field and near-field) feature a broad background component at low wavenumbers.

This region is of special interest for our experiments since the stretching vibrations of Au-S and Au-N (corresponding to the adsorbate-substrate interaction for the molecules probed) lie within the same region, and therefore are difficult to analyze without developing an appropriate fitting method.

In general, the low-wavenumber region has two components:

i) A fixed component which is also present in the far-field spectra, which does not show any near-field enhancement and does not change upon potential (or STM parameters) ramp. Since this broad feature is identical in the retracted and TER spectra, we treat it as a fixed background component.

In the case of adenine in Chapter 6 we use an average of the retracted spectra at different sample potentials (far-field spectra) which were identical within the noise level. A free fitting in this region (between 155.64 and 309.79 cm^{-1})

	y_0[counts]	A[counts·cm^{-2}]	x_0[cm^{-1}]	B[cm^{-2}]
MGITC	11009	$1.09 \cdot 10^{1}0$	**649.68**	$4.43 \cdot 10^{6}$
Air TERS	±65.1	$\pm 9.04 \cdot 10^{8}$	±13.7	$\pm 2.55 \cdot 10^{5}$
MGITC	831.8211009	$1.62 \cdot 10^{9}$	**788.29**	$1.58 \cdot 10^{6}$
water TERS	±12	$\pm 7.31 \cdot 10^{7}$	±7.43	$\pm 5.7 \cdot 10^{4}$
PhS	772.82	$1.39 \cdot 10^{9}$	**690.95**	$1.90 \cdot 10^{6}$
Air TERS	±207	$\pm 8.91 \cdot 10^{-5}$	±60.8	±0.06
PhS	1074.6	$1.45 \cdot 10^{8}$	**511.74**	$9.8 \cdot 10^{5}$
Water TERS	±3.3	$\pm 1.14 \cdot 10^{7}$	±8.44	$\pm 5.64 \cdot 10^{4}$

TABLE I. Parameters of the background fittings plotted in Figs. A.1 and A.2

returns 2 Lorentzian peaks at 172.17 cm^{-1} (FWHM = 49.02, Area = 2793.8) and 220.22 cm^{-1} (FWHM = 80, Area = 2479.3). The fitting results are presented in Fig. A.3. The results of the retracted spectra describe perfectly the low-wavenumber feature of the TER spectra (as shown in Fig. 6.1 d). We therefore fit the TER spectra by constraining the previously described peaks at 172.17 and 220.22 cm^{-1} as a background component and allowing the fitting to find new near-field bands.

For the PhS measurements in liquid of Chapter 5 we follow a similar approach. More specifically we use all the collected far-field spectra in liquid to fit the constant components and fix them on the fitting procedure of the TER spectra.

ii) For adenine, a near-field band is found at potentials $E_{sample} > 0.6$,V whose Raman shift and intensity are potential-dependent (as shown in Fig. 6.1). For PhS in Chapter 5, a near-field band is found at ca. 255 cm^{-1} which shifts considerably as a function of E_b.

The origin of the constant feature (in far-field and near-field) is at present unclear. We observe the same feature in all solid/liquid experiments performed with our setup but not in air. They presumably originate from the aqueous environment, where the thermal fluctuation and composition of the solvent is expected to affect the spectral features.

A.3 Potential-dependent adenine bands: peak fitting

The discussion of the EC-TERS spectra of adenine contained in Chapter 6 is largely based on the intensity changes and frequency shifts of the bands, and therefore some details of the fitting results are provided in this section.

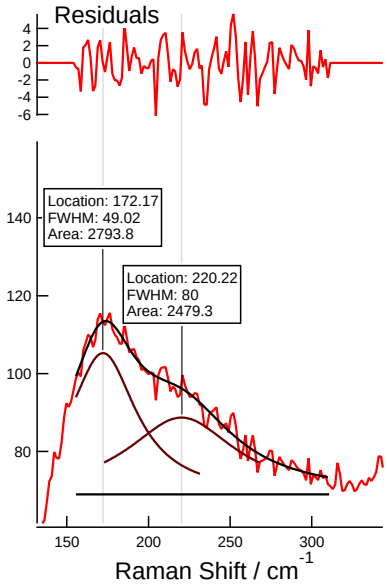

FIGURE A.3. Fitting of the far-field (20 nm tip retraction) spectrum of adenine/Au(111) in H_2SO_4 (0.01 M). Reproduced with permission from *Angewandte Chemie Int. Ed.*, 88, 7108-7114 (2016); Copyright 2017 Wiley-VCH Verlag GmbH & Co. KGaA.[4]

For a given potential, the spectrum used for the fitting is a result of an average of 5 individual spectra taken consecutively. The spectra have been fitted applying masks to reduced frequency ranges in order to avoid errors induced by the changing TERS background. The 736 cm^{-1} mode is fitted as a single Lorentzian peak in the region between 690.74 and 793.01 cm^{-1}, assuming a linear background. The region between 1273 and 1508 cm^{-1} is fitted with Lorentzian peaks and linear background (between 1 and 4 peaks are obtained from the free fittings depending on the sample potential analyzed).

Appendix B

DFT calculations

In this appendix details of the simulations presented in Chapter 6 are included. Theoretical calculations included in this work are performed by collaborators. Dr. Tatsuhiko Ohto[a] and Dr. Yuki Nagata[b] made the orientation dependent DFT calculations. Dr. Denis Andrienko [c] made the simulations of the adenine Raman spectrum for protonated, neutral and anionic species. Their work (simulations, figures and text) is included here for a proper understanding of the experimental results.

Neutral (charge 0, S = 0) and N1-protonated (charge +1, S = 0) and cation (charge +1, S = 1/2) molecules were first optimized using the B3LYP functional and aug-cc-pVTZ basis set using the GAUSSIAN09 package.[182] The pre-resonance Raman intensities (averaged over molecular orientations) were computed by evaluating polarizability derivatives by numerically differentiating the analytic dipole derivatives with respect to an electric field. The resulting Raman spectra are shown in Fig. B.1A. To estimate the effect of long range interactions, were performed the same calculations using the CAM-B3LYP/aug-cc-pVTZ functional/basis set. As Figure SB.1B shows, no significant differences in relative spectral shifts were found.

The orientation-dependent Raman intensity was calculated by transferring the molecular polarizability calculated in the molecular frame to that in the lab frame. The rotation of the polarizability can be estimated from:

$$\alpha^{lab} = A^t \alpha^{mol} A$$

[a]Graduate School of Engineering Science, Osaka University, Toyonaka, Japan
[b]Max Planck Institute for Polymer Research, molecular spectroscopy department, Mainz, Germany
[c]Max Planck Institute for Polymer Research, polymer theory department, Mainz, Germany

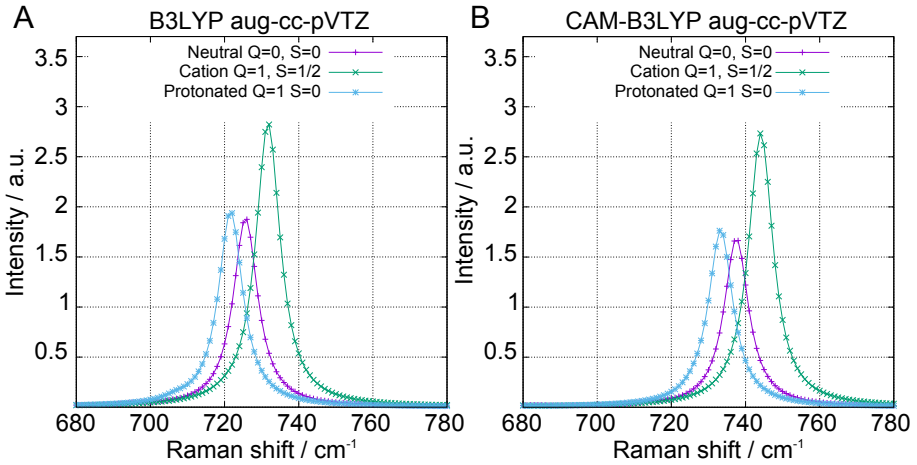

FIGURE B.1. Calculated Raman spectra using the B3LYP functional (A), and the CAM-B3LYP/aug-cc-pVTZ functional/basis set (B). Reproduced with permission from *Angewandte Chemie Int. Ed.*, 88, 7108-7114 (2016); Copyright 2017 Wiley-VCH Verlag GmbH & Co. KGaA.[4]. By Dr. Denis Andrienko.

where α^{lab} is the polarizability tensor in the lab frame, α^{mol} is the polarizability in the molecular frame, A is the rotational matrix converting from the molecular frame to the lab frame. Since in this study we rotated along y and x-axes, the corresponding rotational matrix A_y or A_x, respectively, renders to:

$$A_y = \begin{bmatrix} cos(\theta) & 0 & sin(\theta) \\ 0 & 1 & 0 \\ -sin(\theta) & 0 & cos(\theta) \end{bmatrix}$$

$$A_x = \begin{bmatrix} 1 & 0 & 0 \\ 0 & cos(\theta) & -sin(\theta) \\ 0 & sin(\theta) & cos(\theta) \end{bmatrix}$$

B.1 Polarizability tensor

The simulations of the neutral adenine returned vibrational modes at 725.71 and 1514.03 cm^{-1}. The transition polarizabilities for these modes are reported in eqs. (B.1) and (B.2), respectively. The simulations of the protonated adenine for the same modes returned bands shifted to 721.69 and 1511.89 cm^{-1}. The respective transition polarizabilities for the protonated molecule are reported in

eqs. (B.3) and (B.4), respectively.

$$\alpha_{ij}(Neutral, 725.71) = \begin{bmatrix} 0.879261 & 0.243536 & 0.228457 \cdot 10^{-3} \\ 0.243536 & 0.968468 & 0.384041 \cdot 10^{-2} \\ 0.228457 \cdot 10^{-3} & 0.384041 \cdot 10^{-2} & 0.278196 \end{bmatrix} \tag{B.1}$$

$$\alpha_{ij}(Neutral, 1514.03) = \begin{bmatrix} -0.239922 \cdot 10^{1} & -0.341878 \cdot 10^{-1} & 0.198503 \cdot 10^{-2} \\ -0.341878 \cdot 10^{-1} & -0.177500 & -0.179628 \cdot 10^{-2} \\ 0.198503 \cdot 10^{-2} & -0.179628 \cdot 10^{-2} & -0.195549 \end{bmatrix} \tag{B.2}$$

$$\alpha_{ij}(Prot, 721.69) = \begin{bmatrix} 0.919670 & 0.130127 & -0.728378 \cdot 10^{-3} \\ 0.130127 & 0.995191 & -0.210687 \cdot 10^{-2} \\ -0.728378 \cdot 10^{-3} & -0.210687 \cdot 10^{-2} & 0.280621 \end{bmatrix} \tag{B.3}$$

$$\alpha_{ij}(Prot, 1511.89) = \begin{bmatrix} -0.276388 \cdot 10^{1} & -0.526311 & 0.295483 \cdot 10^{-2} \\ -0.526311 & -0.264349 & 0.669949 \cdot 10^{-3} \\ 0.295483 \cdot 10^{-2} & 0.669949 \cdot 10^{-3} & -0.149078 \end{bmatrix} \tag{B.4}$$

Bibliography

1. N. Martín Sabanés, L. Driessen, K. F. Domke, *Analytical Chemistry* **2016**, *88*, 7108–7114.

2. N. Martín Sabanés, K. F. Domke, *ChemElectroChem* **2017**, *4*, 1814–1823.

3. N. Martín Sabanés, A. Elizabeth, J. H. K. Pfisterer, K. F. Domke, *Faraday Discussions* **2017**, *205*, 233–243.

4. a) N. Martín Sabanés, T. Ohto, D. Adrienko, Y. Nagata, K. F. Domke, *Angewandte Chemie International Edition* **2017**, *56*, 9796–9801; b) N. Martín Sabanés, T. Ohto, D. Adrienko, Y. Nagata, K. F. Domke, *Angewandte Chemie* **2017**, *129*, 9928 –9933.

5. a) M. T. M. Koper, E. Bouwman, *Angewandte Chemie International Edition* **2010**, *49*, 3723–3725; b) M. T. M. Koper, E. Bouwman, *Angewandte Chemie* **2010**, *122*, 3810–3812.

6. C. Cheng, P. R. McGonigal, J. F. Stoddart, R. D. Astumian, *ACS Nano* **2015**, *9*, 8672–8688.

7. P. Simon, Y. Gogotsi, B. Dunn, *Science* **2014**, *343*, 1210–1211.

8. A. J. Bard, R. W. Murray, *Proceedings of the National Academy of Sciences* **2012**, *109*, 11484–11486.

9. S. Szunerits, S. E. Pust, G. Wittstock, *Analytical and Bioanalytical Chemistry* **2007**, *389*, 1103–1120.

10. a) R. Wen, B. Rahn, O. M. Magnussen, *Angewandte Chemie International Edition* **2015**, *54*, 6062–6066; b) R. Wen, B. Rahn, O. M. Magnussen, *Angewandte Chemie* **2015**, *127*, 6160–6164.

11. a) T. Sun, Y. Yu, B. J. Zacher, M. V. Mirkin, *Angewandte Chemie International Edition* **2014**, *53*, 14120–14123; b) T. Sun, Y. Yu, B. J. Zacher, M. V. Mirkin, *Angewandte Chemie* **2014**, *53*, 14120–14123.

12. J. P. Grote, A. R. Zeradjanin, S. Cherevko, K. J. J. Mayrhofer, *Review of Scientific Instruments* **2014**, *85*, 1041011–1041014.

13. C. H. Wu, R. S. Weatherup, M. B. Salmeron, *Physical Chemistry Chemical Physics* **2015**, *17*, 30229–30239.

14. M. Dell'Angela, T. Anniyev, M. Beye, R. Coffee, J. Gladh, T. Katayama, S. Kaya, O. Krupin, J. Larue, D. Nordlund, H. Ogasawara, L. G. M. Pettersson, W. F. Schlotter, J. A. Sellberg, F. Sorgenfrei, J. J. Turner, M. Wolf, W. Wurth, A. Nilsson, *Science* **2013**, *339*, 1302–1306.

15. J. J. Velasco-Velez, C. H. Wu, T. A. Pascal, L. F. Wan, J. Guo, D. Prendergast, M. Salmeron, *Science* **2014**, *346*, 831–834.

16. M. Osawa, *Bulletin of the Chemical Sociecty of Japan* **1997**, *70*, 2861–2880.

17. J.-T. Li, Z.-Y. Zhou, I. Broadwell, S.-G. Sun, *Accounts of Chemical Research* **2012**, *45*, 485–494.

18. P. B. Miranda, Y. R. Shen, *The Journal of Physical Chemistry B* **1999**, *103*, 3292–3307.

19. F. Vidal, A. Tadjeddine, *Reports on Progress in Physics* **2005**, *68*, 1095–1127.

20. Y. Tong, K. Cai, M. Wolf, R. K. Campen, *Catalysis Today* **2016**, *260*, 66–71.

21. M. Fleischmann, P. J. Hendra, A. J. McQuillan, *Journal of the Chemical Society Chemical Communications* **1973**, 80–81.

22. D. L. Jeanmaire, R. P. Van Duyne, *Journal of Electroanalytical Chemistry* **1977**, *84*, 1–20.

23. Z.-Q. Tian, B. Ren, *Annual Review of Physical Chemistry* **2004**, *55*, 197–229.

24. a) A. Hartschuh, *Angewandte Chemie International Edition* **2008**, *47*, 8178–8191; b) A. Hartschuh, *Angewandte Chemie* **2008**, *120*, 8298–8312.

25. G. Sharma, T. Deckert-Gaudig, V. Deckert, *Advanced Drug Delivery Reviews* **2015**, *89*, 42–56.

26. N. Jiang, D. Kurouski, E. A. Pozzi, N. Chiang, M. C. Hersam, R. P. Van Duyne, *Chemical Physics Letters* **2016**, *659*, 16–24.

27. R. Zhang, Y. Zhang, Z. C. Dong, S. Jiang, C. Zhang, L. G. Chen, L. Zhang, Y. Liao, J. Aizpurua, Y. Luo, J. L. Yang, J. G. Hou, *Nature* **2013**, *498*, 82–86.

28. N. Jiang, N. Chiang, L. R. Madison, E. A. Pozzi, M. R. Wasielewski, T. Seideman, M. A. Ratner, M. C. Hersam, G. C. Schatz, R. P. Van Duyne, *Nano Letters* **2016**, *16*, 3898–3904.

29. D. Zhang, K. F. Domke, B. Pettinger, *ChemPhysChem* **2010**, *11*, 1662–1665.

30. X. Wang, K. Broch, F. Schreiber, A. J. Meixner, D. Zhang, *Physical Chemistry Chemical Physics* **2016**, *18*, 15919–15926.

31. T. Schmid, B.-S. Yeo, G. Leong, J. Stadler, R. Zenobi, *Journal of Raman Spectroscopy* **2009**, *40*, 1392–1399.

32. W. Schmickler, E. Santos, *Interfacial Electrochemistry*, Springer, 2nd ed., **2010**.

33. J. K. Sass, *Vacuum* **1983**, *33*, 741–751.

34. *Electrochemistry at the Nanoscale*, (Eds.: P. Schmuki, S. Virtanen), Springer, 1st ed., **2009**.

35. T. Deckert-Gaudig, A. Taguchi, S. Kawata, V. Deckert, *Chemical Society Reviews* **2017**, *46*, 4077–4110.

36. P. Verma, *Chemical Reviews* **2017**, *117*, 6447–6466.

37. X. Wang, S.-C. Huang, T.-X. Huang, H.-S. Su, J.-H. Zhong, Z.-C. Zeng, M.-H. Li, B. Ren, *Chemical Society Reviews* **2017**, *46*, 4020–4041.

38. A. B. Zrimsek, N. Chiang, M. Mattei, S. Zaleski, M. O. McAnally, C. T. Chapman, A.-I. Henry, G. C. Schatz, R. P. Van Duyne, *Chemical Reviews* **2017**, *117*, 7583–7613.

39. M. Fleischmann, P. Hendra, A. J. McQuillan, *Chemical Physics Letters* **1974**, *26*, 163–166.

40. M. G. Albrecht, J. A. Creighton, *Journal of American Chemical Society* **1977**, *99*, 5215–5217.

41. *Surface-Enhanced Raman Scattering*, (Eds.: K. Kneipp, M. Moskovits, H. Kneipp), Springer, 1st ed., **2006**.

42. E. C. Le Ru, P. G. Etchegoin, *Principles of surface-enhaced Raman spectroscopy and related plasmonic effects.*, Elsevier, 1st ed., **2009**.

43. Y. Inouye, *Proceedings of SPIE* **1999**, *3791*, 40–48.

44. R. M. Stöckle, Y. D. Suh, V. Deckert, R. Zenobi, *Chemical Physics Letters* **2000**, *318*, 131–136.

45. N. Hayazawa, Y. Inouye, Z. Sekkat, S. Kawata, *Optics Communications* **2000**, *183*, 333–336.

46. M. S. Anderson, *Applied Physics Letters* **2000**, *76*, 3130–3132.

47. B. Pettinger, G. Picardi, R. Schuster, G. Ertl, *Electrochemistry* **2000**, *12*, 942–949.

48. A. J. Bard, L. R. Faulkner, *Electrochemical Methods: Fundamentals and applications*, Wiley, 2nd ed., **2001**.

49. D. A. C. Brownson, C. E. Banks, *The Handbook of graphene electrochemistry*, Springer, 1st ed., **2014**, pp. 23–78.

50. *Handbook of Reference Electrodes*, (Eds.: G. Inzelt, A. Lewenstam, F. Scholz), Springer, **2013**.

51. I. V. Pobelov, PhD thesis, Rheinisch-Westfalischen Technical University of Aachen, **2008**.

52. G. Binnig, H. Rohrer, C. Gerber, E. Weibel, *Physical Review Letters* **1982**, *49*, 57–61.

53. E. Meyer, H. J. Hug, R. Bennewitz, *Scanning probe microscopy: the lab on a tip*, Springer, 1st ed., **2004**.

54. J. G. Simmons, *Journal of Applied Physics* **1963**, *34*, 1793–1803.

55. J. Bardeen, *Physical Review Letters* **1961**, *6*, 57–59.

56. J. Tersoff, D. Hamann, *Physical Review Letters* **1983**, *50*, 1998–2001.

57. R. L. McCreery, *Chemistry of Materials* **2004**, *16*, 4477–4496.

58. L. Bürgi, H. Brune, K. Kern, *Physical Review Letters* **2002**, *89*, 1768011–1768014.

59. T. Aoki, T. Yokoyama, *Physical Review B* **2014**, *89*, 1554231–1554235.

60. D. A. Long, *The Raman effect: A unified treatment of the theory of Raman scattering by molecules.*, Wiley, 1st ed., **2002**.

61. R. L. Olmon, M. B. Raschke, *Nanotechnology* **2012**, *23*, 1–28.

62. L. Novotny, N. van Hulst, *Nature Photonics* **2011**, *5*, 83–90.

63. K. F. Domke, PhD thesis, Freien Universität Berlin, **2006**.

64. N. Mauser, A. Hartschuh, *Chemical Society Reviews* **2014**, *43*, 1248–1262.

65. X. Shi, N. Coca-López, J. Janik, A. Hartschuh, *Chemical Reviews* **2017**, *117*, 4945–4960.

66. A. Campion, J. E. Ivanecky, C. M. Child, M. Foster, *Journal of the American Chemical Society* **1995**, *117*, 11807–11808.

67. J. R. Lombardi, R. L. Birke, *Accounts Of Chemical Research* **2009**, *42*, 734–742.

68. L. Jensen, *AIP Conference Proceedings* **2012**, *182*, 182–188.

69. L. G. Cançado, A. Jorio, A. Ismach, E. Joselevich, A. Hartschuh, L. Novotny, *Physical Review Letters* **2009**, *103*, 1861011–1861014.

70. R. V. Maximiano, R. Beams, L. Novotny, A. Jorio, L. G. Cançado, *Physical Review B* **2012**, *85*, 2354341–2354348.

71. B. Pettinger, K. F. Domke, D. Zhang, R. Schuster, G. Ertl, *Physical Review B* **2007**, *76*, 1134091–1134094.

72. B. Pettinger, K. F. Domke, D. Zhang, G. Picardi, R. Schuster, *Surface Science* **2009**, *603*, 1335–1341.

73. N. Anderson, A. Hartschuh, S. Cronin, L. Novotny, *Journal of the American Chemical Society* **2005**, *127*, 2533–2537.

74. J. Steidtner, B. Pettinger, *Physical Review Letters* **2008**, *100*, 2361011–2361014.

75. J. Stadler, T. Schmid, R. Zenobi, *Nano Letters* **2010**, *10*, 4514–4520.

76. R. W. Rendell, D. J. Scalapino, *Physical Review B* **1981**, *24*, 3276–3294.

77. S. F. Becker, M. Esmann, K. W. Yoo, P. Gross, R. Vogelgesang, N. K. Park, C. Lienau, *ACS Photonics* **2016**, *3*, 223–232.

78. B. Pettinger, B. Ren, G. Picardi, R. Schuster, G. Ertl, *Physical Review Letters* **2004**, *92*, 0961011–0961014.

79. R. Matsui, P. Verma, T. Ichimura, Y. Inouye, S. Kawata, *Applied Physics Letters* **2007**, *90*, 0619061–0619063.

80. a) E. Bailo, V. Deckert, *Angewandte Chemie International Edition* **2008**, *47*, 1658–1661; b) E. Bailo, V. Deckert, *Angewandte Chemie* **2008**, *120*, 1682–1685.

81. N. Peica, C. Thomsen, J. Maultzsch, *Physica Status Solidi B* **2010**, *247*, 2818–2822.

82. N. Jiang, E. T. Foley, J. M. Klingsporn, M. D. Sonntag, N. A. Valley, J. A. Dieringer, T. Seideman, G. C. Schatz, M. C. Hersam, R. P. Van Duyne, *Nano Letters* **2012**, *12*, 5061–5067.

83. L. Opilik, P. Payamyar, J. Szczerbinski, A. P. Schütz, M. Servalli, T. Hungerland, A. D. Schlüter, R. Zenobi, *ACS Nano* **2015**, *9*, 4252–4259.

84. E. Sheremet, A. G. Milekhin, R. D. Rodriguez, T. Weiss, M. Nesterov, E. E. Rodyakina, O. D. Gordan, L. L. Sveshnikova, T. A. Duda, V. A. Gridchin, V. M. Dzhagan, M. Hietschold, D. R. T. Zahn, *Physical Chemistry Chemical Physics* **2015**, *17*, 21198–21203.

85. X. Wang, J. H. Zhong, M. Zhang, Z. Liu, D. Y. Wu, B. Ren, *Analytical Chemistry* **2016**, *88*, 915–921.

86. N. Kumar, S. Mignuzzi, W. Su, D. Roy, *EPJ Techniques and Instrumentation* **2015**, *2*, 1–23.

87. Z. Zhang, S. Sheng, R. Wang, M. Sun, *Analytical Chemistry* **2016**, *88*, 9328–9346.

88. D. Kurouski, M. Mattei, R. P. Van Duyne, *Nano Letters* **2015**, *15*, 7956–7962.

89. K. F. Domke, B. Pettinger, *ChemPhysChem* **2010**, *11*, 1365–1373.

90. T. Deckert-Gaudig, M. Richter, D. Knebel, T. Jähnke, T. Jankowski, E. Stock, V. Deckert, *Applied Spectroscopy* **2014**, *68*, 916–919.

91. R. Ossikovski, Q. Nguyen, G. Picardi, *Physical Review B* **2007**, *75*, 1–9.

92. K. L. A. Chan, S. G. Kazarian, *Nanotechnology* **2011**, *22*, 175701.

93. A. Drechsler, M. Lieb, C. Debus, A. Meixner, G. Tarrach, *Optics Express* **2001**, *9*, 637–644.

94. J. Steidtner, B. Pettinger, *Review of Scientific Instruments* **2007**, *78*, 1031041–1031048.

95. B. Pettinger, P. Schambach, C. J. Villagómez, N. Scott, *Annual Review of Physical Chemistry* **2012**, *63*, 379–399.

96. G. Picardi, Q. Nguyen, J. Schreiber, R. Ossikovski, *The European Physical Journal Applied Physics* **2007**, *40*, 197–201.

97. K. Karraï, R. D. Grober, *Ultramicroscopy* **1995**, *61*, 197–205.

98. A. Hartschuh, H. Qian, A. J. Meixner, N. Anderson, L. Novotny, *Nano Letters* **2005**, *5*, 2310–2313.

99. A. Hartschuh, N. Anderson, L. Novotny, *Journal of microscopy* **2003**, *210*, 234–240.

100. T.-X. Huang, S.-C. Huang, M.-H. Li, Z.-C. Zeng, X. Wang, B. Ren, *Analytical and Bioanalytical Chemistry* **2015**, *407*, 8177–8195.

101. B. Ren, G. Picardi, B. Pettinger, *Review of Scientific Instruments* **2004**, *75*, 837–841.

102. J. S. Lloyd, A. Williams, R. H. Rickman, A. McCowen, P. R. Dunstan, *Applied Physics Letters* **2011**, *99*, 1431081–1431084.

103. V. Snitka, R. D. Rodrigues, V. Lendraitis, *Microelectronic Engineering* **2011**, *88*, 2759–2762.

104. a) B. Ren, G. Picardi, B. Pettinger, R. Schuster, G. Ertl, *Angewandte Chemie International Edition* **2005**, *44*, 139–142; b) B. Ren, G. Picardi, B. Pettinger, R. Schuster, G. Ertl, *Angewandte Chemie* **2005**, *117*, 141–144.

105. K. F. Domke, D. Zhang, B. Pettinger, *The Journal of Physical Chemistry C* **2007**, *111*, 8611–8616.

106. A. Nakata, T. Nomoto, T. Toyota, M. Fujinami, *Analytical sciences* **2013**, *29*, 865–869.

107. Z.-C. Zeng, S.-C. Huang, D.-Y. Wu, L.-Y. Meng, M.-H. Li, T.-X. Huang, J.-H. Zhong, X. Wang, Z.-L. Yang, B. Ren, *Journal of the American Chemical Society* **2015**, *137*, 11928–11931.

108. M. Mattei, G. Kang, G. Goubert, D. V. Chulhai, G. C. Schatz, L. Jensen, R. P. Van Duyne, *Nano Letters* **2016**, *17*, 590–596.

109. T. Touzalin, A. L. Dauphin, S. Joiret, I. T. Lucas, E. Maisonhaute, *Physical Chemistry Chemical Physics* **2016**, *18*, 15510–15513.

110. P. Pienpinijtham, S. Vantasin, Y. Kitahama, S. Ekgasit, Y. Ozaki, *The Journal of Physical Chemistry C* **2016**, *120*, 14663–14668.

111. M. J. Booth, T. Wilson, *Journal of Biomedical Optics* **2001**, *6*, 266–272.

112. A. Egner, S. W. Hell, *Aberrations in confocal and multi-photon fluorescence microscopy induced by refractive index mismatch*, Springer, 3rd ed., **2006**, pp. 404–413.

113. B. Gjonaj, P. Johnson, M. Bonn, K. F. Domke, *Applied Optics* **2012**, *51*, 8034–8040.

114. S. Hell, G. Reiner, C. Cremer, E. H. K. Stelzer, *Journal of microscopy* **1993**, *169*, 391–405.

115. D. Iwaniuk, P. Rastogi, E. Hack, *Optics Express* **2011**, *19*, 19407–19414.

116. I. M. Vellekoop, A. P. Mosk, *Optics Communications* **2007**, *281*, 3071–3080.

117. P. Birch, D. Budgett, C. Chatwin, R. Young, *Optics letters* **2001**, *26*, 920–922.

118. L. Billot, L. Berguiga, M. de la Chapelle, Y. Gilbert, R. Bachelot, *The European Physical Journal Applied Physics* **2005**, *31*, 139–145.

119. Z. L. Li, T. H. Wu, Z. J. Niu, W. Huang, H. D. Nie, *Electrochemistry Communications* **2004**, *6*, 44–48.

120. *Scanning Tunneling Microscopy II*, (Eds.: R. Wiesendanger, H.-J. Gtintherodt), Springer, 1st ed., **1992**.

121. J. Clavilier, R. Faure, G. Guinet, R. Durand, *Journal of Electroanalytical Chemistry and Interfacial Electrochemistry* **1980**, *107*, 205–209.

122. B. Pettinger, B. Ren, G. Picardi, R. Schuster, G. Ertl, *Journal of Raman Spectroscopy* **2005**, *36*, 541–550.

123. K. F. Domke, D. Zhang, B. Pettinger, *Journal of the American Chemical Society* **2006**, *128*, 14721–14727.

124. C. Blum, L. Opilik, J. M. Atkin, K. Braun, S. B. Kämmer, V. Kravtsov, N. Kumar, S. Lemeshko, J. F. Li, K. Luszcz, T. Maleki, A. J. Meixner, S. Minne, M. B. Raschke, B. Ren, J. Rogalski, D. Roy, B. Stephanidis, X. Wang, D. Zhang, J. H. Zhong, R. Zenobi, *Journal of Raman Spectroscopy* **2014**, *45*, 22–31.

125. K. F. Domke, D. Zhang, B. Pettinger, *Journal of the American Chemical Society* **2007**, *129*, 6708–6709.

126. V. M. Hallmark, S. Chiang, J. F. Rabolt, J. D. Swalen, R. J. Wilson, *Physical Review Letters* **1987**, *59*, 2879–2882.

127. Y. Fujita, N. N. Horimoto, S. Kajimoto, H. Fukumura, *Chemical Physics Letters* **2013**, *582*, 110–114.

128. L. E. C. van de Leemput, H. van Kempen, *Reports on Progress in Physics* **1992**, *55*, 1165–1240.

129. J. Halbritter, G. Repphun, S. Vinzelberg, G. Staikov, W. J. Lorenz, *Electrochimica Acta* **1995**, *40*, 1385–1394.

130. M. Hugelmann, W. Schindler, *Surface Science* **2003**, *541*, L643–L648.

131. J. Pan, T. W. Jing, S. M. Lindsay, *The Journal of Physical Chemistry* **1994**, *98*, 4205–4208.

132. A. Vaught, T. W. Jing, S. M. Lindsay, *Chemical Physics Letters* **1995**, *236*, 306–310.

133. D. H. Woo, E. M. Choi, Y. H. Yoon, K. J. Kim, I. C. Jeon, H. Kang, *Surface Science* **2007**, *601*, 1554–1559.

134. A. Hartschuh, E. J. Sánchez, X. S. Xie, L. Novotny, *Physical Review Letters* **2003**, *90*, 7–10.

135. F. Festy, A. Demming, D. Richards, *Ultramicroscopy* **2004**, *100*, 437–441.

136. I. Notingher, A. Elfick, *The Journal of Physical Chemistry B* **2005**, *109*, 15699–15706.

137. N. Kumar, A. Rae, D. Roy, *Applied Physics Letters* **2014**, *104*, 1231061–1231066.

138. D. W. Scott, J. P. McCullough, W. N. Hubbard, J. F. Messerly, I. A. Hossenlopp, F. R. Frow, G. Waddington, *Journal of the American Chemical Society* **1956**, *78*, 5463–5468.

139. D. H. Dressler, Y. Mastai, M. Rosenbluh, Y. Fleger, *Journal of Molecular Structure* **2009**, *935*, 92–96.

140. C. Toccafondi, G. Picardi, R. Ossikovski, *The Journal of Physical Chemistry C* **2016**, *120*, 18209–18219.

141. K. F. Domke, B. Pettinger, *Physical Review B* **2007**, *75*, 2364011–2364013.

142. C. G. T. Feugmo, V. Liégeois, *ChemPhysChem* **2013**, *14*, 1633–1645.

143. D. J. Wold, R. Haag, M. A. Rampi, C. D. Frisbie, *The Journal of Physical Chemistry B* **2002**, *106*, 2813–2816.

144. S. B. Sachs, S. P. Dudek, R. P. Hsung, L. R. Sita, J. F. Smalley, M. D. Newton, S. W. Feldberg, C. E. D. Chidsey, *Journal of American Chemical Society* **1997**, *119*, 10563–10564.

145. S. Creager, C. J. Yu, C. Bamdad, S. O. Connor, T. Maclean, Y. Chong, G. T. Olsen, J. Luo, M. Gozin, J. F. Kayyem, E. Lam, *Journal of American Chemical Society* **1999**, *121*, 1059–1064.

146. H. Yamamoto, D. H. Waldeck, *The Journal of Physical Chemistry B* **2002**, *106*, 7469–7473.

147. L. Venkataraman, J. E. Klare, C. Nuckolls, M. S. Hybertsen, M. L. Steigerwald, *Nature* **2006**, *442*, 904–907.

148. H. H. B. Akkerman, B. de Boer, *Journal of Physics: Condensed Matter* **2008**, *20*, 130011–1300120.

149. a) M. E. Chiu, D. J. Watson, G. Kyriakou, M. S. Tikhov, R. M. Lambert, *Angewandte Chemie International Edition* **2006**, *45*, 7530–7534; b) M. E. Chiu, D. J. Watson, G. Kyriakou, M. S. Tikhov, R. M. Lambert, *Angewandte Chemie* **2006**, *118*, 7692 –7696.

150. Z. Qiu, M. Zhang, D. Y. Wu, S. Y. Ding, Q. Q. Zuo, Y. F. Huang, W. Shen, X. D. Lin, Z. Q. Tian, B. W. Mao, *ChemPhysChem* **2013**, *14*, 2217–2224.

151. M. Lukas, K. Dössel, A. Schramm, O. Fuhr, C. Stroh, M. Mayor, K. Fink, H. V. Löhneysen, *ACS Nano* **2013**, *7*, 6170–6180.

152. S. Baldelli, *Accounts of Chemical Research* **2008**, *41*, 421–431.

153. S. Zaleski, A. J. Wilson, M. Mattei, X. Chen, G. Goubert, M. F. Cardinal, K. A. Willets, R. P. Van Duyne, *Accounts of Chemical Research* **2016**, *49*, 2023–2030.

154. a) H. Wackerbarth, M. Grubb, J. Zhang, A. G. Hansen, J. Ulstrup, *Angewandte Chemie International Edition* **2004**, *43*, 198–203; b) H. Wackerbarth, M. Grubb, J. Zhang, A. G. Hansen, J. Ulstrup, *Angewandte Chemie* **2004**, *116*, 200 –205.

155. R. Wen, B. Rahn, O. M. Magnussen, *The Journal of Physical Chemistry C* **2016**, *120*, 15765–15771.

156. a) E. Katz, I. Willner, *Angewandte Chemie International Edition* **2004**, *43*, 6042–6108; b) E. Katz, I. Willner, *Angewandte Chemie* **2004**, *116*, 6166–6235.

157. P. A. Sontz, N. B. Muren, J. K. Barton, *Accounts of Chemical Research* **2012**, *45*, 1792–1800.

158. N. J. Tao, J. a. DeRose, S. M. Lindsay, *The Journal of Physical Chemistry* **1993**, *97*, 910–919.

159. Y.-J. Xiao, Y.-F. Chen, X.-X. Gao, *Spectrochimica Acta Part A* **1999**, *55*, 1209–1218.

160. A. P. M. Camargo, H. Baumgärtel, C. Donner, *Physical Chemistry Chemical Physics* **2003**, *5*, 1657–1664.

161. A. Martins, A. Queirós, F. Silva, *ChemPhysChem* **2005**, *6*, 1056–1060.

162. A. Rodes, M. Rueda, F. Prieto, C. Prado, J. M. Feliu, A. Aldaz, *The Journal of Physical Chemistry C* **2009**, *113*, 18784–18794.

163. M. Rueda, F. Prieto, A. Rodes, J. M. Delgado, *Electrochimica Acta* **2012**, *82*, 534–542.

164. C. Vaz-Domínguez, M. Escudero-Escribano, A. Cuesta, F. Prieto-Dapena, C. Cerrillos, M. Rueda, *Electrochemistry Communications* **2013**, *35*, 61–64.

165. B.-Y. Wen, X. Jin, Y. Li, Y.-H. Wang, C.-Y. Li, M.-M. Liang, R. Panneerselvam, Q.-C. Xu, D.-Y. Wu, Z.-L. Yang, J.-F. Li, Z.-Q. Tian, *Analyst* **2016**, *141*, 3731–3736.

166. F. Prieto, Z. Su, J. J. Leitch, M. Rueda, J. Lipkowski, *Langmuir* **2016**, *32*, 3827–3835.

167. R. Santamaria, E. Charro, a. Zacaras, M. Castro, *Journal of Computational Chemistry* **1999**, *20*, 511–530.

168. B. Giese, D. Mcnaughton, *The Journal of Physical Chemistry B* **2002**, *106*, 101–112.

169. J. Kundu, O. Neumann, B. Janesko, D. Zhang, S. Lal, A. Barhoumi, G. E. Scuseria, N. J. Halas, *The Journal of physical Chemistry C* **2009**, *113*, 14390–14397.

170. D. M. Kolb., J. Schneider, *Electrochimica Acta* **1986**, *31*, 929–936.

171. A. P. M. Camargo, H. Baumgärtel, C. Donner, *PhysChemComm* **2002**, *5*, 151–157.

172. C. Prado, F. Prieto, M. Rueda, J. Feliu, A. Aldaz, *Electrochimica Acta* **2007**, *52*, 3168–3180.

173. L. M. Gonçalves, C. Batchelor-Mcauley, A. A. Barros, R. G. Compton, *The Journal of Physical Chemistry C* **2010**, *114*, 14213–14219.

174. G. Dryhurst, P. J. Elving, *Journal of The Electrochemical Society* **1968**, *115*, 1014–1020.

175. H. Angerstein-Kozlowska, B. E. Conway, A. Hamelin, L. Stoicoviciu, *Journal of Electroanalytical Chemistry* **1987**, *228*, 429–453.

176. A. Hamelin, A. Martins, *Journal of Electroanalytical Chemistry and Interfacial Electrochemistry* **1996**, *407*, 1–11.

177. S. Jiang, Y. Zhang, R. Zhang, C. Hu, M. Liao, Y. Luo, J. Yang, Z. Dong, J. G. Hou, *Nature Nanotechnology* **2015**, *10*, 865–870.

178. C. Zhang, B. Q. Chen, Z. Y. Li, *The Journal of Physical Chemistry C* **2015**, *119*, 11858–11871.

179. F. Latorre, S. Kupfer, T. Bocklitz, D. Kinzel, S. Trautmann, S. Gräfe, V. Deckert, *Nanoscale* **2016**, *8*, 10229–10239.

180. T. Deckert-Gaudig, D. Kurouski, M. A. B. Hedegaard, P. Singh, I. K. Lednev, V. Deckert, *Scientific Reports* **2016**, *6*, 335751–335759.

181. D. Ibañez, A. Santidrian, A. Heras, M. Kalbáč, A. Colina, *The Journal of Physical Chemistry C* **2015**, *119*, 8191–8198.

182. M. J. Frisch, *et al*, *Gaussian 09 Revision E.01*, **2009**.